

CBET lolol

(Hopefully soon to be Dr.) Philip W. X. Moloney

IMPERIAL

June 2024

Submitted in partial fulfilment of the requirements for the degree of
Doctor of Philosophy of Imperial College London

Department of Physics
Imperial College London
Prince Consort Road
London SW7 2AZ

Contents

1 SOLAS, a 3-D Laser Ray-Trace and Cross-Beam Energy Transfer Model	16
1.1 Ray-Tracing for Hydrodynamic Simulations of Fusion Plasmas	17
1.2 Existing Cross-Beam Energy Transfer Models	18
1.2.1 Ray-Based Models	18
1.2.2 Wave Solvers	20
1.2.3 Particle in Cell Codes	21
1.3 SOLAS 3-D Laser Ray-Trace	21
1.3.1 Outline of SOLAS-CHIMERA Interfacing	22
1.3.2 SOLAS Mesh Structure	22
1.3.3 Ray Initialisation	26
1.3.4 Equations of Rays and Adaptive Integration	29
1.4 Ray-Based Field Reconstruction and Ray Sheets	35
1.4.1 Ray-Amplitude and Field Estimate from Neighbour Rays	36
1.4.2 Caustic Field Capping	40
1.4.3 Field Reconstruction Validation	41
1.5 Ray-Based CBET Model	44
1.5.1 Power Change of Rays due to CBET	45
1.5.2 Caustic Gain Truncation	48
1.5.3 Coherent Caustic Correction and Caustic Region Identification	50
1.5.4 Dynamic Memory for Storing Fields and CBET Gains	52
1.5.5 Pump Depletion Iterations	53
1.5.6 Energy Conservation Iterations	54
1.5.7 CBET Validation	56
1.6 Simulations of CBET for OMEGA Direct-Drive Implosions	61
1.6.1 1-D hydrodynamics, 3-D Ray-Trace Simulation of OMEGA Shot 89224 . .	61
1.6.2 3-D Post Process of Absorption Non-Uniformity	66
1.7 Conclusions	68
2 Cylindrical Simulations to Study the Effect of Beam Radius in Direct-Drive	70
2.1 Introduction to Beam Radius in Direct-Drive Inertial Confinement Fusion . . .	71
2.1.1 Previous Work Studying the Effect of Beam Radius on OMEGA	73
2.1.2 Statistical Modelling of OMEGA Direct-Drive Implosions	74
2.2 Cylindrical Simulation Platform for Beam Radius Parameter Scan	77
2.2.1 Advantages and Validity Considerations of the Cylindrical Simulation Platform	78

2.2.2	Pulse Shape and Target Initial Conditions	79
2.2.3	1-D Implosion Tuning	80
2.3	Asymmetry of Deposited Power	82
2.3.1	Analysis and Quantity Definitions	83
2.3.2	Deposition Asymmetries in the Absence of CBET	84
2.3.3	CBET Imprint on Incident Field	85
2.3.4	Deposition Asymmetries in the Presence of CBET	88
2.4	Stagnation State Asymmetry	90
2.4.1	Stagnation State Asymmetry Trend with Beam Radius	90
2.4.2	Time Resolved Asymmetry Growth	93
2.4.3	Comparison of Results to Statistical Modelling	95
2.5	Conclusions	96
2.5.1	Summary of work	96
2.5.2	Future Work	97
A	Numerics Appendices	100
Bibliography		101
Copyright Permissions		121

List of Acronyms

Rad-MHD Radiative-Magnetohydrodynamics

Rad-Hydro Radiative-Hydrodynamics

HEDP High Energy Density Physics

LPIs Laser-Plasma Instabilities

CBET Cross-Beam Energy Transfer

ICF Inertial Confinement Fusion

PiC Particle in Cell

GO Geometric Optics

SBS Stimulated Brillouin Scattering

PCGO Paraxial Complex Geometric Optics

IRT Inverse Ray Tracing

FRT Forward Ray Tracing

LLE Laboratory for Laser Energetics

LLNL Lawrence Livermore National Laboratory

CEA Commissariat à l'Énergie Atomique et aux Energies Alternatives

IAW Ion Acoustic Wave

OpenMP Open Multi-Processing

MPI Message Passing Interface

Inv-Brem Inverse-Bremsstrahlung

EI Etalon Integral

FL Field Limiter

CGT Caustic Gain Truncation

DPRs Distributed Polarization Rotators

RTI Rayleigh–Taylor Instability

IFAR In-Flight Aspect Ratio

ADI Alternating-Direction Implicit

DFT Discrete Fourier Transform

List of Tables

1.1	The ratio of the power of the seed beam as it exits the domain to its initial power.	56
1.2	Integrated metrics from simulations of OMEGA 89224. LILAC metrics are from Refs. [1–3].	62
2.1	Results of the 1-D Tuning Simulations.	80

List of Figures

1.1	3-D ray trajectories through a spherically symmetric, OMEGA direct-drive scale density profile. The incident rays are plotted in cyan and the reflected rays, which spread out over a large solid angle, are plotted in dark blue. The critical density is represented by the black mesh.	19
1.2	A flowchart illustrating the basic interfacing between CHIMERA and SOLAS. The interpolation steps refer simultaneously to the re-domain balancing and cell combination procedures described in Sec. 1.3.2.	22
1.3	An illustrative diagram demonstrating the MPI re-domain balanced grid employed by SOLAS compared to the CHIMERA domain balanced grid for a cylindrical geometry.	23
1.4	Illustrative diagrams demonstrating a) the spherical polar mesh used by CHIMERA for hydrodynamic calculations, b) the cell combination mechanism employed by SOLAS to obtain a roughly equal area grid for spherical simulations and c) the adaptive radial cell combination to reduce resolution in regions where Cross-Beam Energy Transfer (CBET) and refraction are unimportant.	25
1.5	Example initial locations for ~ 4000 rays for an OMEGA beam port with super-Gaussian intensity profile, with a shape defined by $n_s = 5.2$ and $\sigma = 352 \mu\text{m}$. The inverse-projection ray locations are shown in sub-figure a) which demonstrate a higher ray density for rays pointed to the pole at $x \sim -0.15\text{mm}$. b) shows the randomly sampled rays where all rays are initialised with the same power, and c) shows uniformly sampled rays.	26
1.6	Shape function smearing for ray power interpolation to the SOLAS grid for a cylindrical mesh. The shape function has the same size and geometry as the SOLAS grid cell which the ray is located in. A top-hat shape function is used, so the fraction of the deposited power interpolated to a given cell is proportional to the volume overlap of the shape function with the cell.	31
1.7	Results of the quadratic trough ray trajectory test problem for the adaptive solver with 3 different cases. These are default settings (linear interpolation of both n_e and ∇n_e), the Kaiser algorithm (linear interpolation of n_e and uniform ∇n_e in a cell) and the adaptive algorithm with tricubic interpolation of n_e). The top plot shows ray trajectories and analytic trajectory and the bottom plot shows absolute errors for the 3 cases.	32

1.8 Results from the cylindrical-helix test problem, obtained using the default adaptive RK45 algorithm. a) shows the trajectory of a ray from a simulation with 100 radial cells in 3-D space. b) shows the trajectory of the ray projected on the $x-y$ plane, along with the n_e profile. c) shows the error of the test, defined as the fractional difference in radius of the ray as it exits the domain from the initial radius, as a function of number of radial cells.	34
1.9 Results of the blast wave Inverse-Bremsstrahlung (Inv-Brem) absorption test problem. The colour-plot shows the temperature of the 1-D simulation as a function of time (x -axis) and space (y -axis). The heatfront obtained from CHIMERA, which is the maximum x location where $T_e > T_{e0}$, is in good agreement with the analytic solution.	35
1.10 A demonstration of how the ray-amplitude is obtained from the area of neighbouring-rays for a beam propagating up a linear density gradient. Fig. a) explicitly shows the trajectory of a main-ray and its neighbour-rays in red and blue respectively, explicitly highlighting the beam's caustic region, where the amplitude of the light is capped. Fig. b) plots the area of the main-ray in blue (which goes through a minimum at the caustic location), as a function of the phase of the ray. Also shown are the uncapped and capped amplitudes of the ray.	37
1.11 An illustration of the concept of caustics and ray sheets. In a), the trajectory of rays traversing up a linear density gradient are plotted. Separate colours are used for the incident and reflected sheets, which are separated by a caustic. In b), rays propagate up a density profile, $n_e = n_{cr} \exp [-(r_{\mu m} - 20)/100]$. Unlike in a), the ray caustics do not occur at their turning point, <i>i.e.</i> the minimum radius.	38
1.12 Results of the 1-D field reconstruction test, comparing SOLAS fields with different caustic field capping methods to the LPSE results. Panel a) shows the oscillatory behaviour of the field solution which arises due to the interference between the incident and reflected sheet. Panel b) plots the same results, but zoomed in on the caustic region to demonstrate the differences in fields obtained from the different methods.	42
1.13 Results of the 2-D field reconstruction test. Panel a) plots the field from LPSE on the left side and the SOLAS field on the right for the 1/64 OMEGA scale simulation. Panel b) shows the SOLAS field from the 1/4 scale simulation which, when compared to a), demonstrates that as scale increases, the relative size of the caustic region decreases. Panels c), d) and e) are lineouts near the caustic region along y from the 1/64 scale simulations at $x = 0, 3$ and $6 \mu m$ respectively, the positions of which are indicated by the white lines on a). Note that the circular features in the field in panels a) and b) arise due to aliasing artefacts between the true solution scale, with the resolution of the image and/ or simulation grid.	43

1.14 The SOLAS CBET model operation loop. F_i is shorthand for the total field from all sheets at pump depletion iteration i and f_{CP} is the modifier to the caustic pump multiplier, described in Sec. 1.5.6 of the j^{th} energy conservation iteration. ΔE denotes the energy conservation error, which is the total incident power minus deposited power and power exiting the grid.	45
1.15 Illustration of the Caustic Gain Truncation (CGT) and caustic region identification algorithms. Panel a) shows a laser, separated into incident and reflected sheets by a caustic, propagating up and reflecting in a linear density ramp. CGT is illustrated in b) where a cell is separated into a <i>lit</i> and <i>unlit</i> region by the reconstructed <i>caustic plane</i> (dashed magenta line). Panels c) and d) illustrate the method used to identify the <i>caustic region</i> (shaded blue), where the coherent caustic modifier is applied. c) shows that cells are geometrically separated into <i>capped</i> (blue squares) and <i>uncapped</i> (red squares) regions and the coherent caustic modifier to the gain is applied in this capped, caustic-region.	49
1.16 Results of successive pump depletion iterations for an illustrative simulation of two beams crossing and undergoing a CBET resonance in a uniform plasma background. Each beams' rays from the field reconstruction ray-trace are plotted in a), where more opaque rays indicate a higher power. Panel b) plots the reconstructed intensity from this ray-trace, where $i = 0$ indicates the field reconstruction ray-trace and therefore no CBET occurs. Panels c) and d) plot the intensity reconstructed from the 1 st and 7 th pump depletion iterations respectively, where the effect of transfer of powers between beams due to CBET is evident. Panel e) plots the convergence parameter from the simulation over successive pump depletion iterations, with convergence defined here as $K_{\text{Conv},0} = 10^{-6}$	53
1.17 Energy conservation iterations for a two-beam caustic test problem, which is presented in Sec. 1.5.7.2. 4 iterations were required to achieve energy conservation, which was defined to be $\delta E < 1 \times 10^{-4}$. The order of the iterations is indicated by the text next to each point.	55
1.18 Results of the 2-D CBET test in the absence of laser caustics. Panels a) and b) show the electric field from the SOLAS and LPSE simulations respectively, after the pump depletion iterations have occurred. Panels c) and d) plot lineouts from the inbound fields of the pump and seed beams respectively for both SOLAS and LPSE. e) and f) plot the same for the outbound fields.	57
1.19 Results of the 2-D CBET test in the presence of a laser caustic. Panels a) and b) show the electric field from the LPSE and SOLAS simulations respectively. Also plotted is an inset zoom on the caustic region of the seed beam, which demonstrates that SOLAS does not capture the evanescent field. Panels c) and e) plot lineouts from the inbound fields of the pump and seed beams respectively for both SOLAS and LPSE. d) and f) plot the same for the outbound fields.	58

1.20 Results from a resolution scan of the two-beam caustic CBET test both with CGT and without. Plotted in a), b) and c) are the power amplification of the seed beam, initial energy conservation error before energy conservation iterations and caustic pump multiplier used to obtain energy conservation respectively.	59
1.21 Results from the 16 beam CBET test problem. Panel a) plots the deposited power both without (left) and with (right) CBET from the simulation ran in cylindrical coordinates at $1 \mu\text{m}$ radial resolution. Panel b) plots the results of the resolution scan for both Cartesian and cylindrical coordinates. The circles and squares are the values of power deposition without and with enforced energy conservation respectively. The shaded regions illustrate the magnitude of energy conservation error from the initial energy conservation iteration, which can be thought of as the (single-sided) error on the circular points.	60
1.22 The initial conditions for OMEGA shot 89224. The shot was a cryogenic, DT implosion with materials and radii shown in panel a). Panel b) plots the incident laser pulse shape.	62
1.23 CHIMERA-SOLAS simulation of OMEGA shot 89224. Panel a) shows the deposited power both from 2 separate simulations of 89224, one with and one without CBET as red and blue solid curves respectively. The shell radius, defined at the radius of maximum density, is also plotted on the right axis as dashed curves. Panel b) plots the time resolved partition of non-absorbed light for these simulations. Plotted in c) is the energy conservation error after energy conservation was achieved, alongside the value of f_{CP} that was used to achieve conservation.	63
1.24 CBET deposition diagnostics from $t = 1.6 \text{ ns}$ into the CHIMERA-SOLAS simulation of OMEGA 89224, with CBET. Both sub-plots plot the power deposition with and without CBET, along with the g_{CBET} , which is defined as the sum of the absolute value of all power lost or gained by rays via CBET in the cell. The electron density normalised to critical density and radial velocity normalised to the sound speed are also plotted in panel a) and b) respectively. The blue shaded region in b) represents the full-width half-maximum of the g_{CBET} curve.	65
1.25 3-D SOLAS post-process of spherically symmetric hydrodynamic data obtained from a LILAC simulation of an OMEGA direct-drive implosion. Figures a) and b) show the deviation in radially integrated deposited power without and with CBET respectively. Figures c) and d) plot the spherical harmonic modal decomposition for these maps alongside results from the IFRIIT and BEAMCROSSER codes without and with CBET respectively.	66
1.26 Electric fields from the 3-D post-process. Panels a), b), c) and d) plot the incident sheet without CBET, the reflected sheet without CBET, the incident sheet with CBET and the reflected sheet with CBET respectively. The critical surface is plotted with the inbound sheets as a transparent spherical wireframe. Note that the outbound sheets are plotted on a log scale.	68

2.1 The trajectory of rays from two beams through a direct-drive like coronal plasma. The density profile for both simulations is $n_e = n_{\text{cr}} \exp [-(r_{\mu\text{m}} - 20)/100]$. Panels a) and b) plot rays from beams with widths $\sigma = 10$ and $18 \mu\text{m}$ respectively. Ray trajectories are separated for each beam by colour depending on their sheet. Rays coloured in red and dark blue are from the incident sheet (before the ray caustic) and rays coloured in magenta and light blue are from the reflected sheet (after the ray caustic).	71
2.2 Soft x-rays emitted from the ablation surface of direct-drive implosions with various R_b/R_t values, as measured by an x-ray framing camera. All images were taken at a constant capsule radius of $R = 175 \mu\text{m}$. The figure has been reproduced with permission from Ref. [4].	73
2.3 Experimentally inferred fusion yield degradation due to the finite beams on the OMEGA laser facility. The dotted orange curve is the fit obtained from just using the $\bar{R}_{b/t}$ relation, while the black dashed curve uses the full relation in Eq. 2.7. The vertical dotted line indicates the critical threshold, $\hat{R}_{b/t}^{\text{crit}} = 0.86$, after which the $\hat{R}_{b/t}$ also has an effect. The cross validation error from the $\bar{R}_{b/t}$ and full fit is -1.0% and -0.5% respectively. The figure has been reproduced with permission from Ref. [5].	76
2.4 The a) target initial conditions with beam geometry, and b) pulse shape used for the 2-D cylindrical simulations. All beams were polarised out of the simulation plane, in the $+\hat{\mathbf{z}}$ direction. Initial layer radii were taken from the initial conditions for OMEGA shot 89224, presented in Fig. 1.22.a.	79
2.5 Streak plots from two of the 1-D tuning simulations including CBET. Panels a) and b) plot the electron density of the $R_b/R_t = 0.8$ and $R_b/R_t = 1.0$ simulations respectively, as a function of time (x -axis) and radius (y -axis). Panels c) and d) plot the electron temperature for the $R_b/R_t = 0.8$ and $R_b/R_t = 1.0$ simulations respectively.	81
2.6 Demonstration of the analysis workflow to obtain the key results for this chapter. The power deposition at $t = 1.12 \text{ ns}$ from the CBET (left) and no-CBET (right) simulations are plotted in panel a) for the $R_b/R_t = 0.85$ case. Panel b) plots the radially integrated deposition from the profiles in a) as a function of azimuthal angle. It can be seen from this plot, that the CBET asymmetry (light-blue) is greater than the no-CBET asymmetry (red). The power spectrum of these profiles is then plotted in panel c). This demonstrates that the dominant modes in the spectrum are multiples of the number of beams.	82

- 2.7 Radially integrated deposited power from no-CBET simulations as a function of time (x -axis) and angle (y -axis), alongside amplitudes of the dominant modes from a Fourier power spectrum. Panels a) and b) plot the radially integrated deposited power and Fourier modes respectively for the $R_b/R_t = 0.8$ simulation. The same is plotted for the $R_b/R_t = 0.9$ simulation in c) & d) and for the $R_b/R_t = 1.0$ simulation in e) & f). The mode 10 from the number of beams is clearly visible in the radially integrated power plots as 10 peaks to troughs in angle at a given time, *i.e.* 10 cyclical perturbations along a vertical lineout. 85
- 2.8 Demonstration of a mode-flip in P_{dep} for the no-CBET $R_b/R_t = 0.8$ simulation. Panel a), b) and c) plot the power deposition just before, during and just after the mode-flip. Panel d) plots the deviation from the mean of the radially profiles around the azimuthal angle for all 3 times. It can be seen from this plot that the deposition is very symmetric at $t = 0.7$ ns. In all 4 panels, the angles of the beams are shown by the dashed magenta lines. The overlap region where deposition rises as the scale length increases, is highlighted with a white circle in panels a), b) and c). 86
- 2.9 Field structure which leads to CBET induced asymmetry on power deposition and its dependence on R_b/R_t and target convergence. Each panel plots the incident sheet field, which includes the effect of CBET, along with contours of the critical electron density (green) and the incident field, $|E_z^{\text{in}}| = 1 \times 10^{10} \text{ Vm}^{-1}$ contour of another beam (magenta). Panel a) and b) plot this for the $R_b/R_t = 0.9$ simulation at $t = 1.0$ ns and $t = 1.5$ ns respectively. The convergence of the target in this time interval, leads to beams wrapping around the target more, and therefore a change in the spatial location of the resonant CBET interaction. Panel c) plots the same for the $R_b/R_t = 0.80$ simulation at the same time as panel a). This demonstrates that the $R_b/R_t = 0.80$ beam is not wide enough at this time to lead to a resonant CBET interaction, unlike the wider beam in panel a). 87
- 2.10 This figure plots the same as Fig. 2.7, but now for the equivalent simulations which include the effect of CBET. Comparing these results and those in Fig. 2.7 demonstrates that CBET introduces additional modal-flips of the deposition and amplifies the magnitude of asymmetries. 88
- 2.11 Demonstration of a mode-flip in P_{dep} for the CBET, $R_b/R_t = 0.9$ simulation. Panels a), b) and c) plot the power deposition before, during and after the mode-flip. Panel d) plots the deviation from the mean of the radially profiles around the azimuthal angle for all 3 simulations. Fig. 2.9.a and Fig. 2.9.b plot a single, incident sheet field from panels a) and c) respectively. It can be seen that the centre of the beam depletion at $t = 1.5$ ns leads to less deposition at the beam angles (magenta lines) on panel d). Panel b) shows that during the CBET induced mode-flip, a significant $\ell = 20$ occurs in the deposition. The reducing absorption at the centre of one beam is highlighted in by the white dashed circles. 89

2.12 Densities of the DT fuel and ion temperatures for various R_b/R_t simulations both with and without CBET. Each row correspond to a different R_b/R_t value; the left column contains simulations without CBET; and the right column contains simulations with CBET. It is visible from the density plots that increasing R_b/R_t improves stagnation symmetry for the no-CBET simulations, but degrades it for the CBET simulations.	91
2.13 Trends of a) stagnation asymmetry and b) maximum (azimuthally averaged) fuel density for CBET and no-CBET simulations. The no-CBET improvement in symmetry with R_b/R_t is observed which also corresponds to improved compression. The symmetry trend including CBET is more complex, but broadly the stagnation state symmetry is worse with increasing R_b/R_t	92
2.14 Time resolved $\ell = 10$ Fourier power spectrum amplitude for a) $\rho_{DT}R$ and b) $P_{dep}R$ for CBET simulations with 3 R_b/R_t values. The developing, but unrealiised, modal-flip for $R_b/R_t = 0.8$ from $t \sim 0.5 \rightarrow 1.2$ ns reduces the $P_{dep}R_{\ell=10}$, leading to slow $\rho_{DT}R_{\ell=10}$ growth and ultimately a relatively symmetric stagnation state. Despite large values of $\rho_{DT}R_{\ell=10}$ initially, the developing modal flip of the $R_b/R_t = 1.0$ simulation from $t \sim 1.8 \rightarrow 2.1$ ns slows the density asymmetry growth.	94

1 SOLAS, a 3-D Laser Ray-Trace and Cross-Beam Energy Transfer Model

This chapter describes the SOLAS code, a 3-D laser ray-tracing module implemented in the Radiative-Magnetohydrodynamics (Rad-MHD) code CHIMERA. The chapter begins with a discussion of why ray-tracing is frequently used to model ‘long-pulse’ lasers for High Energy Density Physics (HEDP) experiments and why the standard framework is inadequate to model Laser-Plasma Instabilities (LPIs). It then goes on to describe the ray-trajectory solver, electric-field reconstruction and CBET components of the model in detail, including discussion of the validity of the model components. The numerical methods are also presented alongside an extensive set of validation problems to verify the implementation.

1.1 Ray-Tracing for Hydrodynamic Simulations of Fusion Plasmas

Nanosecond length ('long-pulse') lasers are often used as an external energy source in the field of HEDP, for example in laboratory-astrophysics experiments [6–8], equation of state studies [9, 10] or Inertial Confinement Fusion (ICF) implosions [11–13]. Experimental design and analysis for these experiments must often be supported with fluid Rad-MHD simulations. The laser must therefore be described in these codes by a theoretical framework that is both valid and computationally tractable. The physical processes by which lasers interact with plasma are a result of microscopic couplings between the laser field and particles or plasma waves. The detailed microphysics of these interactions are often studied using Particle in Cell (PiC) codes [14] or wave-based solvers [15], typically for scales and durations of tens of micrometres and hundreds of picoseconds. Coupling these tools directly to multidimensional Radiative-Hydrodynamics (Rad-Hydro) simulations, which are often used for millimetre and nanosecond scales, is usually computationally intractable.

The Geometric Optics (GO) assumptions are often applicable for HEDP laser-plasma interactions and therefore ray-tracing offers a computationally tractable approach to modelling lasers in these experiments¹. By assuming static Rad-Hydro profiles (which is normally valid for the propagation time of light through the computational domain) a laser beam can be discretized into a bundle of rays. The ray equations can then be integrated along their path to solve for the trajectory of the light, assuming that refraction dominates over diffraction. A discrete amount of power can also be given to each ray. If there is a suitable model for the power-absorption rate, this can also be integrated along the ray to provide an energy source for the plasma. In many laser-driven HEDP experiments, frequency-doubled or -tripled lasers and long scale-length plasmas mean that Inv-Brem is the dominant deposition process [16, 17]. There are well established models for Inv-Brem that are suitable for implementation in ray-tracing codes, because they only require knowledge of the local plasma conditions, which are easily accessible via interpolation from the Rad-Hydro grid to ray locations [18, 19]. The combination of the ray equations and Inv-Brem deposition is therefore the basis for the vast majority of laser-modules coupled to Rad-Hydro codes.

In laser-driven ICF experiments however, another class of interaction, LPIs, are vitally important to the energetics of the implosion. For example, CBET leads to a zeroth-order correction to the energy deposited in direct-drive experiments at the OMEGA laser facility, reducing coupled power late in the implosion to $\sim 50\%$ [20]. LPIs cannot be included in the simple framework described above for two reasons. Firstly, they are non-linear² and secondly, reduced theoretical models of the interaction rely on knowledge of the electric field or intensity of the light [21]. Implementation in a ray-tracing code therefore necessitates a method by which the separate light waves can 'talk' to each other. For example, the CBET code described in this chapter stores information for separate components of laser beams on a common grid, which can then interact via the 'pump-depletion iterations', described in Sec. 1.5.5. Additionally, calculating the electric field or intensity is problematic because this

¹Validity is discussed in detail for ICF plasmas in Sec. ??

²Non-linear in this context means that the interaction involves multiple light and plasma waves.

is not an attribute which can be obtained from a GO ray. Heuristically, rays have an associated power, so an area is required to obtain an intensity. The evolution of a portion of the beam front's area is governed by a first order expansion of the Helmholtz equation, rather than the zeroth order expansion, which is most commonly used in ray-tracing packages for Rad-Hydro codes [22]. The first order expansion introduces an equation for the ray amplitude, which can be solved in a variety of ways and used to obtain the electric field of the light. Sec. 1.4 describes the approach taken to solving for the amplitude of the rays in SOLAS, which is to track the area of a triangle³ of rays around a standard GO ray.

For direct-drive ICF simulations, it is also desirable to have a 3-D ray-trace, where rays travel and refract in three dimensions. In some computational direct-drive studies, particularly in 1-D Rad-Hydro simulations, simplified laser models are employed in which rays travel radially toward the target [23]. This simplification can lead to significant deviations from reality, as it neglects any refractive losses, which become increasingly significant late in the implosion as the target converges. Assuming that rays travel radially inward, also leads to deposition occurring closer to the critical surface compared to a true 3-D ray-trace, resulting in an overestimation of the drive. The growth of LPIs also depends on vector summations of light and plasma wavevectors, so a 3-D ray-trace is necessary when modelling these effects. Predictive direct-drive simulations therefore necessitate a fully 3-D ray-trace, even when coupled to just 1-D hydrodynamics.

1.2 Existing Cross-Beam Energy Transfer Models

There is a variety of existing computational tools used to model CBET for ICF conditions. These include codes that are used to study the interaction from first principles, reduced models to investigate the effect of CBET when coupled to hydrodynamics and validation tools to test the implementation of these reduced models. A non-exhaustive list of existing codes is listed below, provided as context for the work presented later in this chapter.

1.2.1 Ray-Based Models

The most common tool to study the coupling of CBET effects into hydrodynamics are reduced ray-based models, which use the linear gain theory of Stimulated Brillouin Scattering (SBS), described in more detail in Sec. 1.5. A variety of different codes used to study this. The main difference between the models is the way that the electric field or intensity of the laser light is obtained.

Inverse Ray Tracing (IRT) This is an approach implemented in the IFRIT code, that creates a mapping between points on an initial beam front and arbitrary locations within the plasma [24, 25]. This is in contrast to Forward Ray Tracing (FRT), used in the other ray-based approaches listed below, where discrete points on the beam front are integrated forward to discrete points within the plasma. IRT is an efficient approach for convex, approximately

³For a 2-D ray-trace, a co-planar, pair of rays is used rather than a triangle.

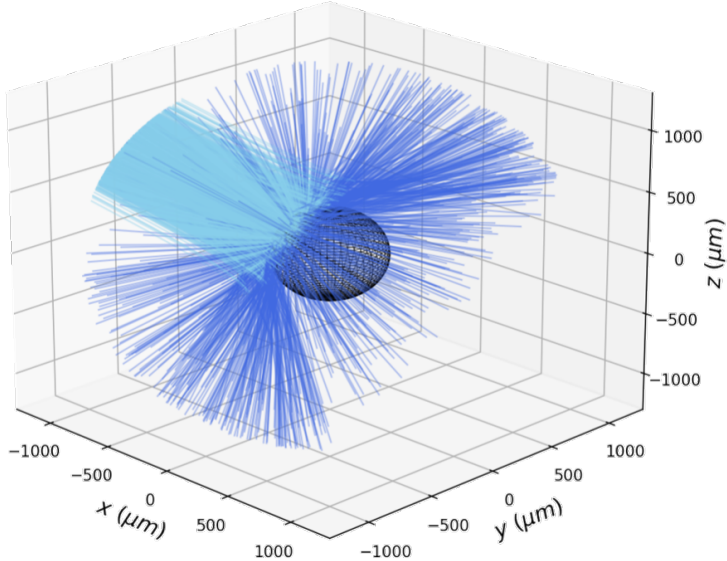


Figure 1.1: 3-D ray trajectories through a spherically symmetric, OMEGA direct-drive scale density profile. The incident rays are plotted in cyan and the reflected rays, which spread out over a large solid angle, are plotted in dark blue. The critical density is represented by the black mesh.

spherically symmetric plasma profiles, but cannot deal well with beams that have multiple caustics⁴, where the FRT approach is better suited. IFRIIT has been coupled to the 3-D Rad-Hydro code, ASTER from Laboratory for Laser Energetics (LLE), and prior to the development of CHIMERA-SOLAS, ASTER-IFRIIT was the only code combination capable of conducting 3-D direct-drive simulations with in-line CBET [20].

Ray Statistics Approach The LASNEX [26], TROLL [27] and DRACO codes [28], developed at Lawrence Livermore National Laboratory (LLNL), Commissariat à l’Énergie Atomique et aux Energies Alternatives (CEA) and LLE respectively, implement field-reconstruction methods, which depend heavily on having many rays per computational cell. LASNEX and TROLL, used mainly for indirect-drive hohlraum simulations, obtain the intensity of light by first propagating rays through the mesh and obtaining the deposited power in each grid cell. The intensity is then obtained from the power in each cell using electromagnetic energy conservation. Obtaining the intensity from deposition means that the field cannot be reconstructed in vacuum regions where no deposition occurs.

DRACO uses a similar approach, but the intensity is estimated by multiplying the ray power by the path length in a cell and dividing by the cell volume, which gives a dimensional estimate for the intensity. Both of these approaches require many rays-per-cell to accurately obtain the intensity, $\mathcal{O}(100)$ [29]. For direct-drive simulations this is extremely computationally expensive, because backscatter CBET dominates over sidescatter. Therefore, the reflected field of each beam must be resolved, and each beam spreads out over a large solid angle after reflecting off a convex density profile, as is demonstrated in Fig. 1.1. This means that

⁴Caustics are defined and discussed in detail in Sec. 1.4.1.

orders of magnitude more rays are required, compared to approaches which can accurately obtain the field from a single ray per cell.

Another drawback of both of these approaches is that caustics of beams (regions where the amplitude of rays diverge) are not identifiable, and therefore fields cannot be capped to physically accurate, diffraction-limited values. If a significant amount of CBET occurs at caustics, such as in direct-drive ICF, then erroneous global multipliers to CBET gains must be applied which are effectively free parameters that must be tuned to obtain a pre-known reduction in absorbed energy. It is therefore difficult to trust this approach for predictive, pre-shot direct-drive simulations.

Paraxial Complex Geometric Optics (PCGO) In this approach, each ray has an associated Gaussian intensity profile, the width of which is integrated along the ray trajectory [22, 30]. A single ray can be used per cell because each ray therefore has an intensity which is interpolated to the mesh. However, the reconstructed field near caustics is not accurate and the width evolution is only valid for a short propagation distance. This approach was coupled to the CHIC 2-D Rad-Hydro code, but the approach is difficult to extend to 3-D as the implementation relied on interacting only rays whose centroids crossed, which does not occur in 3-D for non-coplanar rays [31].

Neighbouring Rays The BEAMCROSSER code obtains an area for each ray by co-tracing a triangle of neighbouring rays around it that can be converted into a ray amplitude and therefore electric field from electromagnetic energy conservation [32]. Integrating the amplitude along the ray trajectory means that the caustics can be identified and therefore fields in those regions capped to diffraction limited values [33]. Each ray also has an individual field value, and it is therefore less dependent on ray-per-cell statistics than geometric models, such as that used in the DRACO code described above [34]. Sec. 1.4 describes the implementation of this approach into the CHIMERA 3-D Rad-MHD code. A similar approach, simplified by assuming uniform illumination of a direct-drive target, has been implemented into the 1-D LILAC Rad-Hydro code [35, 36]. It had previously however, not been coupled to a multidimensional Rad-Hydro code.

1.2.2 Wave Solvers

Solving Maxwell's equations in a plasma background is a useful tool for the study of LPIs. The main code used in the ICF community that uses this approach is LPSE, which propagates light waves through a prescribed, spatially varying density, temperature and velocity profile in 1-D→3-D [15, 37]. It then solves the nonlinear coupling of electromagnetic waves by allowing first order plasma perturbations (obtained from the ponderomotive beat pattern between light waves), which then feed back into the wave propagation. The perturbative approach limits LPSE to linear problems and the temporal and spatial resolution required to resolve the beat frequency mean that coupling to multidimensional Rad-Hydro simulations is not feasible. However, it is an extremely useful tool to validate implementation of CBET

models, especially for laser caustics where diffraction is important, such as the test case presented in Sec. 1.5.7.2. It can also been used for many other important studies, such as the mitigation of LPIs via laser bandwidth and the effect of beam smoothing techniques on the growth rate of LPIs [38].

1.2.3 Particle in Cell Codes

Both ray-based codes and LPSE are ill-suited to the study of LPIs in the non-linear regime, where the laser intensity becomes sufficiently large that the ponderomotive imprint on the plasma can no longer be treated perturbatively. Understanding the growth and saturation of LPIs in this regime is particularly important for ICF schemes with high peak intensities, such as during the ignitor spike in shock ignition pulses [39]. Often kinetic effects such as ion-trapping become important in non-linear saturation, where ions are trapped and then accelerated in the CBET induced Ion Acoustic Wave (IAW), leading to changes in the IAW phase velocity and therefore a loss of resonance [14]. PiC codes operate by using a finite number of macro-particles to represent the distribution function of the plasma, coupled to an electromagnetic solver, discretised on a mesh. They are therefore well suited to model this kinetic saturation, albeit over short timescales and in simulations that are not truly representative of direct-drive conditions, due to computational expense [40]. Kinetic modelling of CBET has demonstrated that the growth of LPIs can be a much more complex, time-dependent problem than is assumed by the linear-models used in ray-based codes, leading to larger net energy transfers [41].

1.3 SOLAS 3-D Laser Ray-Trace

This section describes how the ray equations, derived from the Helmholtz equation in Sec. ?? are solved in the SOLAS module for the CHIMERA Rad-MHD code. Details of the mesh used for spherical simulations, load balancing options as well as validation problems are provided.

A short summary of the computational derived-types is presented here, to aid understanding of the following sections. In SOLAS, a domain balanced mesh is created from the hydrodynamic grid in CHIMERA. The mesh is made up of *laser-cells*, which hold information about the geometry, hydrodynamic-quantities, laser-quantities⁵ and neighbouring cells on the SOLAS grid. *Beam* objects are created which hold user-defined geometric information about the beam-port and pointing location and also store a list of rays from the beam. Each ray is defined by a position (\mathbf{x}), wavevector (\mathbf{k}), phase (φ), angular frequency (ω) and power (P). If field reconstruction is performed, then each ray also stores up to three additional *neighbour-rays*, from which the electric field of the ray can be reconstructed, as described in Sec. 1.4.

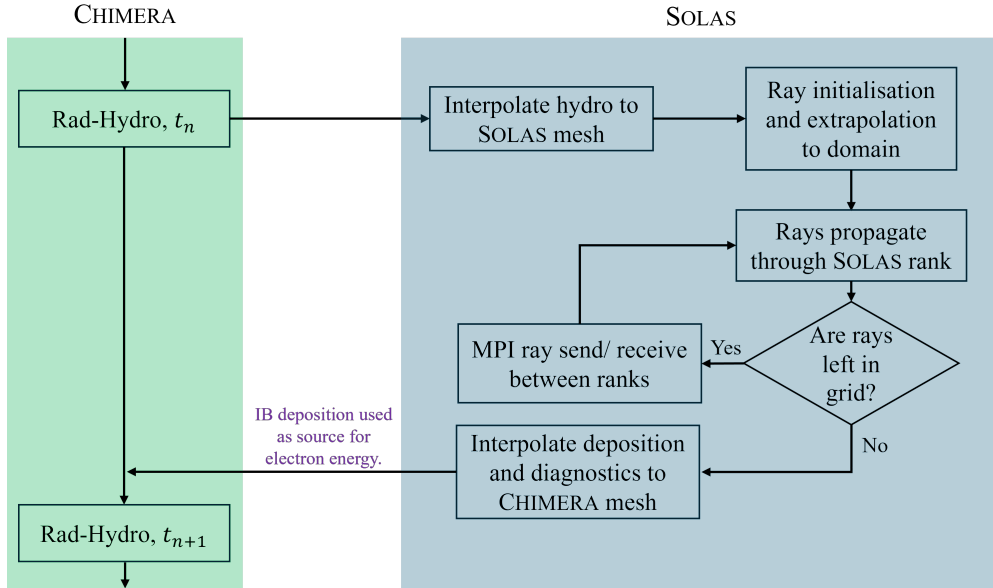


Figure 1.2: A flowchart illustrating the basic interfacing between CHIMERA and SOLAS. The interpolation steps refer simultaneously to the re-domain balancing and cell combination procedures described in Sec. 1.3.2.

1.3.1 Outline of SOLAS-CHIMERA Interfacing

A simple flowchart for the basic SOLAS operational loop and the interfacing with CHIMERA is shown in Fig. 1.2. At the start of a Rad-Hydro timestep, t_n , the hydrodynamic variables (stored on the Eulerian CHIMERA grid), which are necessary to compute ray trajectories and CBET gains, are interpolated to the SOLAS mesh. Rays are then initialised on the beam port locations and extrapolated to the computational domain, before being traced through the grid. SOLAS uses an Message Passing Interface (MPI) domain balanced approach to parallelisation, the reasons for which are discussed in more detail in Sec. 1.3.2, therefore rays are traced up to the internal borders of the MPI rank subdomain. Rays are then passed between ranks and moved through their new subdomain until they exit the entire simulation domain. As rays move through the domain, they lose energy via Inv-Brem, contributing to a running deposition total in each grid cell. When all rays have exited the domain, the SOLAS quantities, such as deposited energy which have been built up from the ray-trace, are then interpolated onto the CHIMERA grid, where the Inv-Brem deposition is used as a source term for the electron energy in the subsequent Rad-Hydro step, t_{n+1} . The interpolation, initialisation and propagation steps are outlined in sections 1.3.2, 1.3.3, 1.3.4 respectively.

1.3.2 SOLAS Mesh Structure

For direct-drive ICF simulations, which model the laser using ray-tracing (especially those which include CBET), the choice of an appropriate computational mesh on which to conduct the laser ray-trace is crucial to obtaining an accurate and noise-free energy deposition.

⁵Laser quantities include, for example, Inv-Brem deposition and electric field strength.

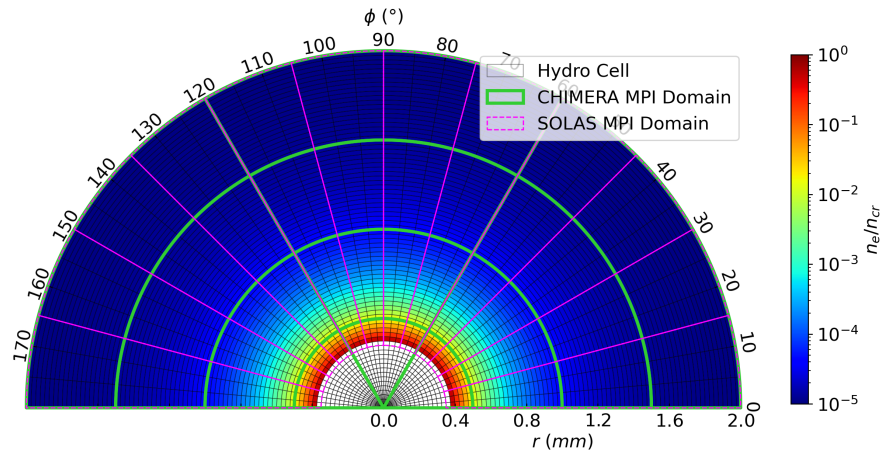


Figure 1.3: An illustrative diagram demonstrating the MPI re-domain balanced grid employed by SOLAS compared to the CHIMERA domain balanced grid for a cylindrical geometry.

A well-chosen grid can also significantly reduce the run-time and memory requirements of the calculation. The mesh used for hydrodynamic simulations of these experiments is often not well suited for ray-tracing calculations. For example, hydrodynamic grids often have excessive resolution in the corona to resolve the gradients in the laser quantities, which greatly increases the expense of tracing rays through the mesh, without significantly enhancing the accuracy of the solution. This section describes the approach taken in the SOLAS code to create a grid structure that accurately resolves laser energy deposition, both with and without CBET, in a memory-efficient manner.

1.3.2.1 Re-Domain Balance for Radial Geometries

Rad-MHD codes including CHIMERA, often employ a domain balanced approach to parallelisation, where each computational rank solves a portion of the entire spatial domain, for each discrete timestep. Additional ‘ghost-cells’ are stored in the subdomains and used to calculate gradients on the boundaries between ranks, which are updated with inter-rank MPI communications each timestep. The hydrodynamic grid for CHIMERA is Eulerian, with options for Cartesian, cylindrical or spherical-polar grids.

The optimal domain balancing minimises the number of ghost cells at subdomain boundaries, which leads to cubic⁶ subdomains. If computing a laser ray-trace through this domain for a typical direct-drive calculation however, initially rays travel approximately radially and therefore regularly encounter processor boundaries where they must be transferred between ranks. A more optimal domain decomposition for the ray-trace minimises radial splitting to avoid excessive passing of rays. For spherical and cylindrical simulations, SOLAS therefore takes the hydrodynamic variables on the CHIMERA grid and re-domain balances the grid

⁶Cubic in cell dimension, not necessarily in physical space for non-Cartesian geometries.

for the ray-trace, such that the splitting does not occur in the radial coordinate. An example of this re-domain balancing is shown in Fig. 1.3 for an illustrative cylindrical mesh. The CHIMERA domain decomposition divides the radial and azimuthal extent into four and three ranks respectively, whereas SOLAS' division is purely in the azimuthal direction. For spherical and cylindrical direct-drive simulations where there is a defined, global minimum critical radius, SOLAS' mesh excludes the grid cells below this minimum radius beyond which the rays cannot reach in order to reduce the memory burden of the re-gridding.

An alternative approach to MPI-based domain-decomposition parallelisation of the module is to use the Open Multi-Processing (OpenMP) package, for which ranks share memory across a computational node. In this approach, the entire laser grid is stored once on the shared memory of the node and separate ranks trace rays through the entire domain without the need for transfers. While this is a preferable approach for a standard ray-trace to the MPI procedure described above, including a model for CBET is more challenging. This is because CBET requires communication between beams and therefore large amounts of information must be stored on the grid, which can lead to large memory overheads. Therefore, using multiple computing nodes is often a necessity for 3-D CBET calculations for which OpenMP-MPI hybrid approaches are required. This was deemed too significant an undertaking for the scope of the work presented in this thesis.

When a 3-D ray-trace is coupled to a lower dimensional hydrodynamics simulation (for example, a 1-D spherical direct-drive simulation) then a sparse 3-D mesh at a user-specified resolution is created for the ray-trace. This 3-D mesh allows the re-domain balancing routine to be employed to load balance the simulation. For CBET simulations, it also allows the field, which is required to compute the power change of rays due to CBET, to be stored as a function of angle when discretised on this sparse 3-D mesh. Storing the field discretised in angle enables the interaction between beams around the sphere to be correctly computed. After the ray-trace, if these extra dimensions have been added to the ray-trace grid, then the deposited power is integrated over the additional grid directions to obtain the source term on the hydrodynamic grid.

1.3.2.2 Semi-Structured Eulerian Grid with Combined Cells

Ideal ICF implosions are spherically symmetric and departures from this symmetry are usually higher-order corrections. Simulations of these experiments therefore typically employ a computational grid with spherical symmetry. CHIMERA typically simulates direct-drive implosions with a spherical-polar Eulerian mesh, shown in Fig. 1.4.a. This grid has the advantage of simplicity to take gradients across cells, however it has the disadvantage that cell edge lengths tend to zero as the radial coordinate, $r \rightarrow 0$ and the polar coordinate, $\theta \rightarrow 0, \pi$. This limits the hydrodynamic timestep, because stable explicit timesteps are inversely proportional to edge lengths, increasing the cost of 3-D spherical simulations. The issue is circumvented at late times in the implosion by remapping onto a Cartesian grid, which does not have vanishing edge lengths and face areas [42].

Computing CBET requires at least a single ray from each interacting beam to pass through

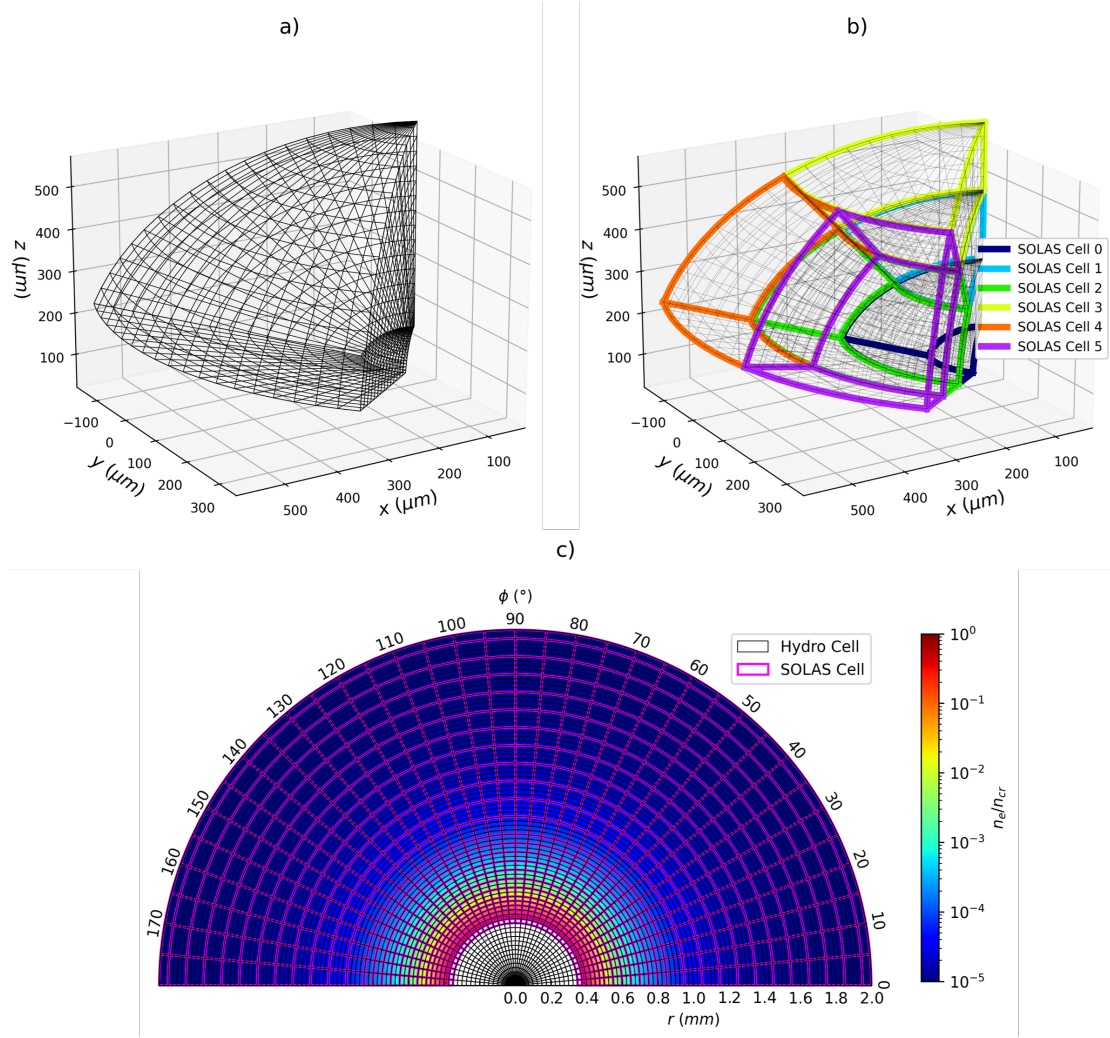


Figure 1.4: Illustrative diagrams demonstrating a) the spherical polar mesh used by CHIMERA for hydrodynamic calculations, b) the cell combination mechanism employed by SOLAS to obtain a roughly equal area grid for spherical simulations and c) the adaptive radial cell combination to reduce resolution in regions where CBET and refraction are unimportant.

each computational grid cell where the interaction should be important. For spherical-polar meshes the vanishing cell volume therefore sets extreme minimum ray number limits for the calculation to fully resolve all the fields, particularly the reflected field in direct-drive simulations, which spreads out over 4π steradians, as is shown in Fig. 1.1. Hydrodynamic resolutions are often also excessive for ray-trace calculations to resolve the necessary refraction and energy exchange of the light. Rays must also stop at each cell boundary in order to deposit the correct amount of energy into each grid cell and therefore the expense of the ray-trace is directly proportional to the number of grid cells that the rays see.

To circumvent these issues, cells can be combined around the spherical grid angles in order to make a semi-structured Eulerian grid, as is shown in Fig. 1.4.b. Hydrodynamic grid cells are merged together on the SOLAS mesh in each grid direction until a pre-specified resolution, set by the user, is reached. In Fig. 1.4.b, many cells are combined in each direction to

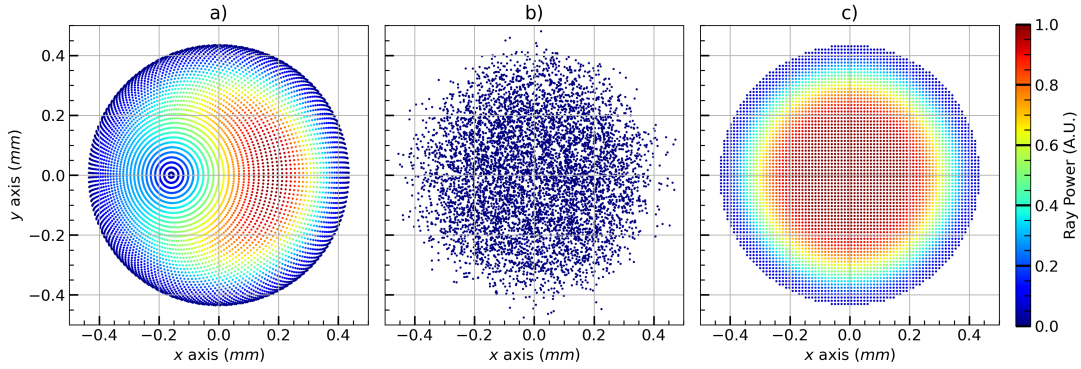


Figure 1.5: Example initial locations for ~ 4000 rays for an OMEGA beam port with super-Gaussian intensity profile, with a shape defined by $n_s = 5.2$ and $\sigma = 352 \mu\text{m}$. The inverse-projection ray locations are shown in sub-figure a) which demonstrate a higher ray density for rays pointed to the pole at $x \sim -0.15\text{mm}$. b) shows the randomly sampled rays where all rays are initialised with the same power, and c) shows uniformly sampled rays.

clearly display the effect. Typically, for spherical simulations however, the cells are not combined in the polar direction, θ and n_φ cells are combined in the azimuthal direction until the azimuthal and polar resolutions match, explicitly $n_\varphi r \Delta\varphi \sin\theta \approx r \Delta\theta$ at a given radius, r .

Fig. 1.4.c demonstrates the capability of the meshing algorithm to adaptively combine cells in the radial direction based upon density gradients. This allows large cells to exist in the coronal plasma where the light refracts minimally and deposits little energy, while the sharp turning point regions close to the critical surface can be well resolved. To find the number of radial cells to combine at a given radius n_r , maximum gradient length scale from the combined hydrodynamic cells, $L_{n_e} = n_{crit}/|\nabla n_e|_{max}$ is calculated. The algorithm then finds the optimal number of cells to merge together such that the new cell resolution $n_r \Delta r \approx C_L L_{n_e}$, where C_L is a user parameter⁷ which can be reduced to limit cell combining. A maximum cell size is also set to prevent excessively large cells in regions with small density gradients.

Note that many options for equal area computational grids exist which, unlike the semi-structured grid described here, are completely uncorrelated from the Rad-Hydro mesh [43, 44]. These have the advantage that the grid can be chosen purely based upon quantities important to the laser ray-trace. However, the mesh described in this section has the advantage that interpolation to the hydrodynamic mesh is extremely straightforward as the SOLAS grid cells completely overlap the CHIMERA cells. This also minimises artefacts from interpolation between the grids, which have the potential to introduce spurious high order modes to the deposition source term.

1.3.3 Ray Initialisation

To obtain a noise-free energy deposition source term from a ray-trace, both the grid and choice of initial ray number and location is crucial. The problems are closely related as a higher resolution grid requires a larger density of rays to get equivalent ray-per-cell statistics.

⁷Default value set to $C_L = 0.05$.

It is therefore wise to choose the number of rays used in a simulation to be some function of the grid used for the ray-trace. Several methods for ray initialisation which have been implemented are briefly outlined here, along with a summary of their strengths and weaknesses.

All beams profiles described in this thesis have circularly symmetric super-Gaussian intensity profiles described by the equation,

$$I(r) = I_0 \exp\left(-\left|\frac{r}{\sigma}\right|^{n_s}\right), \quad (1.1)$$

where r is the distance from the centre of the beam port, perpendicular to the beam normal, I_0 is the peak intensity, σ is the beam width⁸ and n_s is the super-Gaussian exponent.

Uniform Sampling In this method of ray initialisation, demonstrated in Fig. 1.5.c, each beam is assigned a number of rays and a maximum initialisation radius⁹, beyond which rays are not initialised. Rays are then placed on a uniform, square grid in this plane with a power proportional to the intensity value from by Eq. 1.1. For all three procedures described in this subsection, the total summed power of the rays is normalised to the incident beam power after the initialisation of all rays is complete. Typically, for direct-drive, the total number of rays used for spherical simulations is chosen to be,

$$N_{\text{ray}} = C_N \max(N_r N_\varphi, N_r N_\theta, N_\theta N_\varphi), \quad (1.2)$$

where $N_{i=r,\varphi,\theta}$ is the number of SOLAS grid cells in each grid direction and C_N is a user-parameter multiplier which to give better ray statistics for CBET simulations when required. $C_N \sim 2$ is found to give converged deposition when including CBET and so this value is used by default.

When there is sufficiently low ray-per-cell statistics, beat phenomena can occur between the ray spacing and the grid resolution. In this event, especially when using a nearest neighbour interpolation for ray power deposition onto the grid, significant spurious modes can be introduced to the power deposition. To resolve this, ray locations can be ‘dithered’ so that they take a random position within the polygon¹⁰ defined by neighbouring ray locations. This option is always used for simulations using uniform sampling in this thesis.

Random Sampling Rays can also be randomly sampled according to the intensity profile. Example ray locations from this method are shown in Fig. 1.5.b. Note that the intensity profile purely emerges from the ray locations in this method as all rays have equal power. For no-CBET simulations this is a useful method as it minimises coherent build-up of noise from ray-spacing, grid-resolution beating. However, the wings of the intensity profile have poor ray statistics so for direct-drive CBET calculations, resolving the reflected field and therefore the dominant backscatter CBET is excessively expensive.

⁸The radius at which $I = I_0 e^{-1}$.

⁹The maximum initialisation radius is usually set to be the radius at which $I = I_0 e^{-3}$.

¹⁰This polygon is a square for uniform sampling, but not for inverse-projection

Inverse-Projection Inverse-projection is the final method that has been implemented for ray initialisation in SOLAS. The algorithm is described in detail in Appendix A of Ref. [28]. The method works by finding several surfaces, defined by fractions of the critical density and then creating aim points in each cell on the surface. These aim points and their associated area on the surface are back-projected onto each beam port and rays are created if the aim point is not obscured by the surface on which it was created. The power of the ray is then the back-projected area multiplied by the intensity at the beam port location. For a spherical polar grid, this gives a ray distribution which varies in ray density according to which region on the beam port maps to regions on the grid with higher or lower cell-face areas. The higher ray density region on the beam port maps to the polar region of the grid, at $x \sim -0.16\text{ mm}$ on Fig. 1.5.a have a correspondingly lower power compared to rays at equal radii to give the same intensity.

While inverse-projection does guarantee good ray statistics at given surfaces for the in-bound component of the field, the algorithm does not extend to beyond ray caustics, or the reflected field component. Therefore, ray statistics are not guaranteed to be good for the reflected field, so the advantages of this method are not evident for direct-drive CBET simulations when backscatter must be resolved. However, for no-CBET, direct-drive simulations, this is a useful option for ray initialisation.

For all simulations in this thesis, the uniform sampling method with ray dithering is used. This method is found to give the best ray-per cell statistics across the semi-structured Eulerian grid described in Sec. 1.3.2 while minimising the overall number of rays used required to resolve CBET.

After rays are initialised on each of the beam ports, they are extrapolated to the edge of the computational domain. Beam focussing is typically neglected, so all rays are assigned velocities parallel to the beam normal. This approximation is widely used for codes that simulate OMEGA-scale direct-drive implosions, where the lasers are approximately collimated on the implosion scale [20, 28]. It is assumed that outside of the simulation domain is vacuum and rays are therefore extrapolated to the edge of the computational domain in straight lines, using a simple root finding algorithm to obtain the intersection of the rays with either a spherical, cylindrical or rectangular domain depending on the simulation geometry.

1.3.4 Equations of Rays and Adaptive Integration

The partial differential equations that are integrated along the trajectory of each ray are,

$$\begin{aligned}\frac{d\mathbf{x}}{d\tau} &= \mathbf{k}, \\ \frac{d\mathbf{k}}{d\tau} &= \frac{1}{2}\nabla\varepsilon(\mathbf{x}), \\ \frac{d\varphi}{d\tau} &= \varepsilon(\mathbf{x}), \\ \frac{d\omega}{d\tau} &= \frac{\omega}{2c}\frac{\partial(n_e/n_{cr})}{\partial t}, \\ \frac{dP}{d\tau} &= -\kappa_{IB},\end{aligned}\tag{1.3}$$

where $\varepsilon = 1 - n_e/n_{cr}$ is the dielectric permittivity of the plasma, n_e and n_{cr} are the electron and critical densities, c is the speed of light, t is time, κ_{IB} is the Inv-Brem absorption kernel, given explicitly in Eq. ?? and τ is the ray path length. Note that the phase here is defined such that it has the same dimension as path length and therefore has spatial units. The wavevector is normalised such that $|\mathbf{k}| = \sqrt{\varepsilon}$. The optical path length is related to the arc length, ds by the variable change $ds = d\tau\sqrt{\varepsilon}$. In some formulations of the ray-tracing equations, the differential equations are written in terms of the arc length [28, 45], which is equivalent, but more complicated and without benefit. Note that the time, t is not related to the ray path length τ , because an operator split approach is taken to the ray-trace, such that the hydrodynamic variables are frozen and the ray-trace finds the time independent trajectory of the light through these profiles. The path length τ is therefore best seen as a parameterisation of the ray curve.

The frequency shift arises due to light propagating through a time varying refractive index. This causes successive wavefronts to bunch up (blue-shift) or rarefy (red-shift), which occurs for a temporally increasing or decreasing n_e respectively [46]. This effect is only significant for the work presented in this thesis when calculating CBET. For direct-drive calculations at the OMEGA laser facility scale, this results in wavelength shifts of $\Delta\lambda/\lambda_0 \sim \mathcal{O}(0.1\%)$, which is typically negligible for computing ray trajectories. However, the induced wavelength shift is relatively significant when calculating the CBET resonance and in direct-drive can alter the spatial location where scattering is significant [20]. Neglecting time-dependent ionisation effects, which is a good assumption during peak-power for the approximately steady-state direct-drive corona where CBET occurs, the time derivative can be obtained by assuming that n_e is advected with the bulk fluid,

$$\frac{\partial(n_e/n_{cr})}{\partial t} = -\frac{\iiint_V \nabla \cdot [(n_e/n_{cr})\mathbf{u}] dV}{\iiint_V dV},\tag{1.4}$$

where \mathbf{u} is the fluid velocity and the integral is over a computational cell volume. Using the Divergence Theorem, this can be rewritten,

$$\frac{\partial(n_e/n_{cr})}{\partial t} = -\frac{\oint_S (n_e/n_{cr})\hat{\mathbf{n}} \cdot \mathbf{u} dS}{\iiint_V dV},\tag{1.5}$$

where the integral on the numerator is now over the cell bounding area, with normal $\hat{\mathbf{n}}$ [28].

Two algorithms have been implemented to integrate Eqs. 1.3, an adaptive RK45 algorithm and the Kaiser algorithm. These are described below, alongside the method for ray-deposition-to-cell interpolation and time-stepping considerations.

Adaptive RK45 Algorithm The default ray evolution algorithm in SOLAS is to solve Eq. 1.3 using an adaptive RK45 algorithm with stepsize control [47]. Ray steps are either limited by the error from this algorithm, or by distance to the next impact with a cell face. Evaluations of the right-hand side of these equations employ trilinear interpolation for n_e , ∇n_e and T_e to obtain varying values for these quantities at different locations throughout the cell. All other quantities are either defined at the ray location, or use nearest neighbour interpolation. The `bspline-fortran` library has also been implemented to allow tricubic interpolation of n_e , which yields a quadratically varying ∇n_e across the grid [48]. This is slow to evaluate many times per ray step as is required in an RK45 algorithm and therefore limits performance, but is used throughout this chapter as a higher order solution to validate accuracy of the default interpolation.

Linear interpolation of n_e and T_e is required for accurate computation of κ_{IB} , especially for ‘cold-start’ simulations where light impacts upon a solid target and the plasma profiles have steep gradients. Interpolation of ∇n_e was found to be necessary to obtain low-noise ray amplitudes from neighbouring rays for CBET evaluation, which is described in more detail in 1.4. Linear interpolation of both n_e and ∇n_e is technically inconsistent, because ∇n_e should be the gradient of n_e , however the test cases presented in Sec. 1.3.4.1 found that this did not reduce accuracy compared to the Kaiser algorithm, which employs a self-consistent linear interpolation of n_e and constant ∇n_e within a computational cell.

Kaiser Algorithm The Kaiser algorithm for ray integration has also been implemented [45]. In this algorithm, each cell has a single ∇n_e and an n_e value defined at the cell centre, allowing for linear interpolation of n_e throughout the cell. In a constant ∇n_e region, the trajectory of rays can be analytically shown to follow a parabola. The Kaiser algorithm thus evolves rays over parabolic segments between cells by finding the intersection of the parabola with cell faces, using a root finding algorithm. Assuming constant ∇n_e cells leads to discontinuities in n_e at cell interfaces when the true gradient is not linear and thus Snell’s Law is used to refract rays upon cell exit. While this method is often slightly more efficient compared to the adaptive RK45, it was found that when attempting to reconstruct the ray amplitude from the area of neighbouring rays, as outlined in Sec. 1.4, excessive noise was introduced in the amplitude from the discontinuous refraction. Therefore, the adaptive algorithm was used for all work in this thesis, other than where explicitly outlined.

Shape Functions for Ray Deposition Nearest neighbour interpolation of power deposition, which is defined along the ray trajectory, onto the computational grid can result in significant levels of noise in the power deposition profile when ray statistics are not sufficiently high. This is similar to problems experienced in PiC codes when interpolating macro parti-

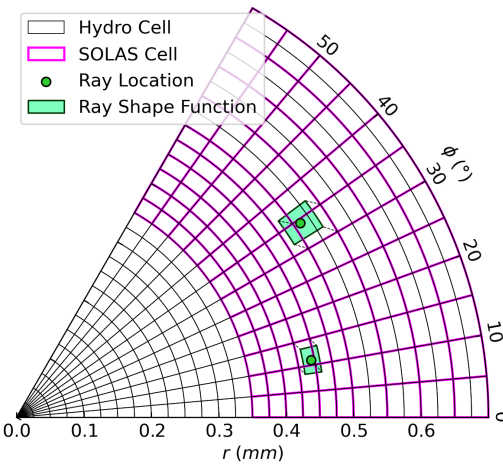


Figure 1.6: Shape function smearing for ray power interpolation to the SOLAS grid for a cylindrical mesh. The shape function has the same size and geometry as the SOLAS grid cell which the ray is located in. A top-hat shape function is used, so the fraction of the deposited power interpolated to a given cell is proportional to the volume overlap of the shape function with the cell.

cles to the grid without the use of shape functions [49, 50]. A PiC-inspired shape function approach was therefore taken, where the power deposition from rays is smeared across neighbouring cells. A top hat shape function is used, with a shape function that has the size and shape of the cell that the ray is located within, as is shown in Fig. 1.6. The power deposited into each cell that has an overlap with the shape function bounds is therefore proportional to the volume overlap of the shape function with the cell. This approach is more explicitly outlined, particularly for the case of the non- logically rectilinear grids which are present for SOLAS, in Ref. [51]. This smearing is somewhat numerically diffusive and therefore can be optionally disabled. For the work presented in this thesis, the shape function smearing is employed for multidimensional direct-drive simulations, but otherwise disabled.

Hydrodynamic Time Step Limiter Laser heating of a plasma results in a temperature increase of the material, which also reduces the Inv-Brem kernel. If the hydrodynamic timestep, δt is too large, excessive heating occurs in initially cold cells, which should have the magnitude of absorption gradually reduced as they warm up. This can lead to spurious oscillations in temperature at fine grid resolutions. A limiter on the hydrodynamic time-step is therefore introduced to prevent large heating in any cell within one timestep. The limit detailed by Haines in Ref. [52] is enforced, which estimates the increase in temperature of a cell from Inv-Brem heating by assuming an ideal gas equation of state to derive,

$$\delta t = \min_{n \in \text{cells}} \left(\tilde{\delta}t, C_{\delta t} \frac{3}{2} \frac{n_{e,n} e T_{e,n} V_n}{P_n} \right), \quad (1.6)$$

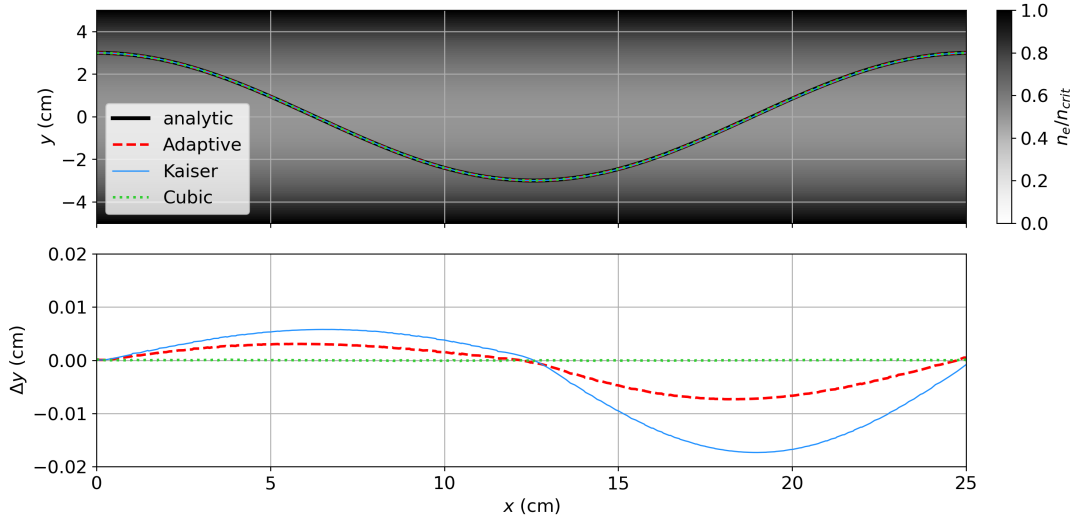


Figure 1.7: Results of the quadratic trough ray trajectory test problem for the adaptive solver with 3 different cases. These are default settings (linear interpolation of both n_e and ∇n_e), the Kaiser algorithm (linear interpolation of n_e and uniform ∇n_e in a cell) and the adaptive algorithm with tricubic interpolation of n_e). The top plot shows ray trajectories and analytic trajectory and the bottom plot shows absolute errors for the 3 cases.

where $\tilde{\delta t}$ is the stable hydrodynamic timestep from other physical processes, $n_{e,n}$, $T_{e,n}$, V_n and P_n are the electron density, electron temperature, volume and deposited power into cell n , and $C_{\delta t}$ is a user defined stability parameter. By default, the parameter $C_{\delta t}$ is set to 1, which is found to be adequate for most situations [52]. Note that Eq. 1.6 is only applied in cells where $n_{e,n} > 1 \times 10^{-4} n_{cr}$. Small amounts of deposition in these cells can lead to large temperature increases, which severely limits δt , despite the cells often being far from the region of interest, normally near critical, where the maximum deposition occurs. For simulations where a laser heats a solid, initially cold target, Eq. 1.6 mostly only affects the hydrodynamic timestep early in the simulation, after which the laser-heated plasma corona remains in a mostly steady-state unless there are steep changes in incident power.

1.3.4.1 Ray Solver Validation

Several validation problems have been conducted to verify that the ray solver has been implemented correctly. Here the quadratic trough and cylindrical helix test problems are presented, which compare the path of a single ray in to an analytic solution in order to verify that the ray solvers correctly obtain the trajectory of light. The blast wave problem is also presented which is a test of Inv-Brem absorption to an analytic solution in the absence of thermal conduction and hydrodynamic motion.

Quadratic trough The quadratic trough is a test of ray trajectory in a quadratic density trough, which admits an analytic solution of a periodically oscillating ray [45, 52]. The den-

sity profile used for the test is defined as,

$$n_e(y) = \frac{n_{\text{cr}}}{2} \left(1 + \frac{y^2}{y_c^2} \right), \quad (1.7)$$

which for light with wavelength $\lambda = 351$ nm, is initialised with $n_{\text{cr}} = 9.049 \times 10^{21}$ cm $^{-3}$ and $y_c = 5$ cm. The domain has bounds $x \in [0, 25]$ cm and $y \in [-5, 5]$ cm and a ray enters the domain at $[x_0, y_0] = [0, 3]$ cm. Analytic integration of the first 2 lines from Eq. 1.3, yields the analytic trajectory as a function of ray path length τ ,

$$\begin{aligned} x(\tau) &= \tau \sqrt{1 - \frac{n_e(y_0)}{n_{\text{cr}}}}, \\ y(\tau) &= y_0 \cos \left(\frac{\tau}{\sqrt{2} y_c} \right). \end{aligned} \quad (1.8)$$

The analytic trajectory is compared to the solution from the adaptive solver (using both default interpolation and tricubic interpolation of n_e) and the Kaiser algorithm in Fig. 1.7. The associated error, defined as the difference in y from the analytic value at a given x is also plotted. Note that all results were obtained using a grid resolution of 100×100 cells. The top panel demonstrates that all trajectories are identical to the analytic solution by eye. The corresponding errors show that the tricubic interpolation effectively perfectly recreates the analytic solution and the Kaiser error is slightly more significant compared to the default adaptive error. The tricubic error is insignificant because the cubic interpolation perfectly recreates the true density profile, so the errors are purely numeric, not due to the resolution. Errors from the other algorithms would therefore decrease more quickly with increasing resolution as the density profile the ray sees becomes more similar to a quadratic trough. The error from the default adaptive interpolation (linear interpolation of both n_e and ∇n_e) is lower than that of Kaiser (linear n_e and uniform ∇n_e), indicating that the inconsistent interpolation is not a significant issue for resolving ray trajectories.

Cylindrical-Helix The quadratic trough test ensures that the ray evolution algorithm functions correctly in Cartesian geometry. An additional test was desired in non-Cartesian geometry, because CHIMERA also operates with cylindrical and spherical grids. The cylindrical-helix test was therefore devised, where a ray enters an axially symmetric density trough that keeps the ray at a constant, cylindrical radius, r , as is shown in Fig. 1.8.b. As is shown in Fig. 1.8.a, the z extent of the simulation is chosen such that the ray has performed one complete helical spiral when it exits the domain. By requiring that a ray undergo circular motion in the $x - y$ plane and specifying the initial ray direction such that $k_{z0} = \sqrt{k_{x0}^2 + k_{y0}^2}$, it can be derived that a ray entering the domain at r_0 will undergo one complete helical spiral over a z length $\Delta z = 2\pi r_0$, if the density profile has the shape,

$$n_e(r) = n_{\text{cr}} \left(1 - \exp \left(\frac{-r^2}{2r_0^2} \right) \right). \quad (1.9)$$

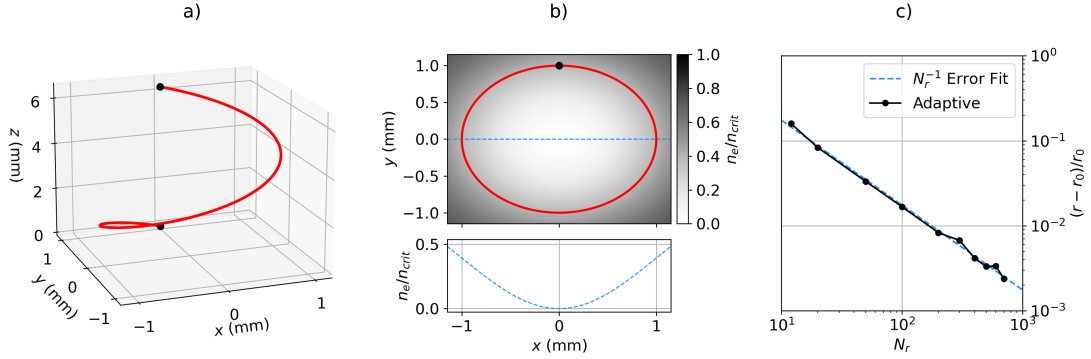


Figure 1.8: Results from the cylindrical-helix test problem, obtained using the default adaptive RK45 algorithm. a) shows the trajectory of a ray from a simulation with 100 radial cells in 3-D space. b) shows the trajectory of the ray projected on the $x - y$ plane, along with the n_e profile. c) shows the error of the test, defined as the fractional difference in radius of the ray as it exits the domain from the initial radius, as a function of number of radial cells.

For a ray entering the domain at $[x_0 = 0, y_0 = 1, z_0 = 2\pi]$ mm, with initial wavevector $[k_{x0} = \sqrt{\varepsilon_0/2}, k_{y0} = 0, k_{z0} = -\sqrt{\varepsilon_0/2}]$, the ray position as a function of path length τ is,

$$\begin{aligned} x(\tau) &= r_0 \sin\left(\sqrt{\frac{\varepsilon_0}{2}}\tau\right), \\ y(\tau) &= r_0 \cos\left(\sqrt{\frac{\varepsilon_0}{2}}\tau\right), \\ z(\tau) &= z_0 - \sqrt{\frac{\varepsilon_0}{2}}\tau, \end{aligned} \quad (1.10)$$

where $\varepsilon_0 \equiv \varepsilon(r = r_0)$.

This problem was run in cylindrical geometry for a variety of radial resolutions, employing the default adaptive RK45 solver with linear interpolation of both n_e and ∇n_e . The domain bounds for the problem were $r \in [0, 1.5]$ mm, $\varphi \in [0, 2\pi]$ and $z \in [0, 2\pi]$ mm, with a single cell in both the φ and z directions. For all radial resolutions, the ray was observed by eye to exit the domain at the expected location, verifying that the ray-trace is functional in non-Cartesian geometries. Plotting the fractional error in ray exit location as a function of number of radial cells, N_r in Fig. 1.8.c, demonstrates that the error in final position of the ray scales as N_r^{-1} . This is because larger N_r more closely recreates the density profile in Eq. 1.9. The error scaling is dictated by the lowest order interpolation used in the algorithm. This is the linear interpolation of n_e for the default adaptive RK45 solver, which leads to the N_r^{-1} scaling.

Blast wave The blast wave problem is a validation test of the implementation of Inv-Brem absorption [52, 53]. In this problem, a 527 nm, 2 ns laser is incident on a uniform density ($\rho = 1 \text{ mg/cm}^{-3}$), cold gas ($T_{e0} = 1 \text{ eV}$) with fixed ionisation at $Z = 6$, that has an ideal gas equation of state. The $\ln \Lambda$ value used for the κ_{IB} coefficient is fixed at 7. The laser travels in the x

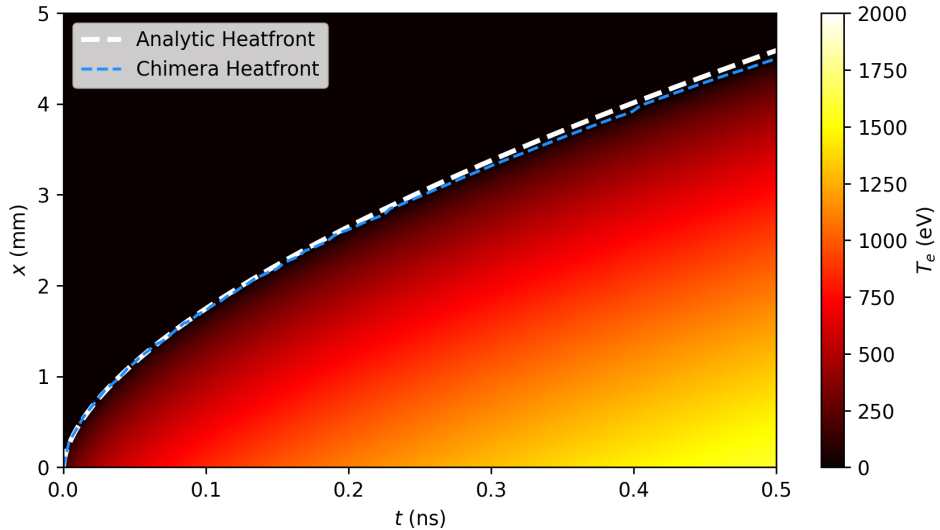


Figure 1.9: Results of the blast wave Inv-Brem absorption test problem. The colour-plot shows the temperature of the 1-D simulation as a function of time (x -axis) and space (y -axis). The heatfront obtained from CHIMERA, which is the maximum x location where $T_e > T_{e0}$, is in good agreement with the analytic solution.

direction and has an intensity of $6.4 \times 10^{13} \text{ Wcm}^{-2}$. Hydrodynamic motion and transport is disabled in the simulation. The laser is initially strongly absorbed in the gas, so energy is not transported beyond the initial layer, perpendicular to the laser propagation direction. As the gas heats up, κ_{IB} decreases and therefore more energy is transported further into the domain by the laser, moving the heatfront forward. The heatfront $x_{\text{analytic}}(t)$, defined as the largest x coordinate at a time, t where $T_e > T_{e0}$, has an analytic solution, derived by Denavit and Phillion in Ref. [53],

$$x_{\text{analytic}}(t) = \frac{2}{3\kappa_{\text{IB}}} \left(\frac{5}{3} \frac{\kappa_{\text{IB}} I}{n_e k_B} \right)^{3/5}, \quad (1.11)$$

which can be compared to the result from a ray-tracing simulation.

Fig. 1.9 shows the results for $T_e(x, t)$ and the heatfront location from a CHIMERA-SOLAS simulation of the blast wave problem. The heatfront from the simulation compares well to the analytic heatfront, validating the implementation of the Inv-Brem absorption kernel.

1.4 Ray-Based Field Reconstruction and Ray Sheets

In order to compute CBET, or other LPIs in a ray-tracing calculation, additional information about the electric field or intensity of the light is required than can be obtained from the ray directly. This section outlines the method used in SOLAS to obtain the electric field of the light along the path of each ray, which broadly follows the implementation from Ref. [34].

1.4.1 Ray-Amplitude and Field Estimate from Neighbour Rays

Recalling the formula for the ray-amplitude, A , Eq. ?? from Sec. ??,

$$A(\tau) = A(0) \left| \frac{D(0)}{D(\tau)} \right|^{1/2}, \quad D(\tau) = \begin{bmatrix} \frac{\partial x}{\partial \zeta_1} & \frac{\partial x}{\partial \zeta_2} & \frac{\partial x}{\partial \tau} \\ \frac{\partial y}{\partial \zeta_1} & \frac{\partial y}{\partial \zeta_2} & \frac{\partial y}{\partial \tau} \\ \frac{\partial z}{\partial \zeta_1} & \frac{\partial z}{\partial \zeta_2} & \frac{\partial z}{\partial \tau} \end{bmatrix}, \quad (1.12)$$

where $[x, y, z]$ and $[\zeta_1, \zeta_2, \tau]$ are the ray real-space and phase-space coordinates respectively and D is the Jacobian for the coordinate transform from phase-space to real-space. When refraction forces rays closer together, $|D(\tau)|$ will decrease and equally, when refraction forces rays to separate, $|D(\tau)|$ will increase. The amplitude can therefore be approximated by assuming proportionality between the determinant of the Jacobian and the area, S of an infinitesimally small bundle of rays surrounding the main ray,

$$A(\tau) = \varepsilon^{-1/4} \sqrt{\frac{S(\tau=0)}{S(\tau)}}, \quad (1.13)$$

where the $\varepsilon^{-1/4}$ term accounts for swelling of the field due to the increased optical path through plasma with finite density [34]. Note that the amplitude is a purely geometric quantity, which holds no information about power changes of the light due to absorption or LPIs. The electric field outside the caustic region, which is discussed in more detail in Sec. 1.4.2, can then be obtained with the formula,

$$\frac{|E(\tau)|}{|E(\tau=0)|} = \sqrt{\frac{P(\tau)}{P(\tau=0)}} A(\tau), \quad (1.14)$$

where P is the power of the ray and the initial (vacuum) electric field $|E(\tau=0)| = \sqrt{2I_0/c\varepsilon_0}$, where I_0 is the intensity of the beam at the ray initialisation point on the beam port.

This method, which has been used successfully to model direct-drive CBET in the BEAM-CROSSER post-process code, is the approach taken to estimate the field in SOLAS. Explicitly, for every ray that initialised for a SOLAS calculation, an additional 3 ‘neighbour-rays’ are initialised in an equilateral triangle around it, perpendicular to the initial direction of propagation. Note that when a 2-D ray-trace is used, only two neighbour-rays are required as the rays cannot change separation in the out of plane direction. It is important to distinguish the dimension of the ray-trace, which is the number of dimensions in which rays can move in a simulation, to the dimension of the hydrodynamics. For example, a 1-D spherical direct-drive Rad-Hydro simulation still requires a 3-D ray-trace where rays can move in x , y and z for full accuracy.

These neighbour-rays are then co-traced up to the phase of the ‘main-ray’ to evaluate the area of the main ray on its phase front. Practically, the separation distance of the bundle of neighbour-rays (i.e. the side-length of the triangle, Δl) does not need to be infinitesimally small, but small enough that it accurately captures the local change of $|D(\tau)|$. In terms of the hydrodynamic profiles, this means that $\Delta l \ll L_{n_e}$, where L_{n_e} is the density length scale

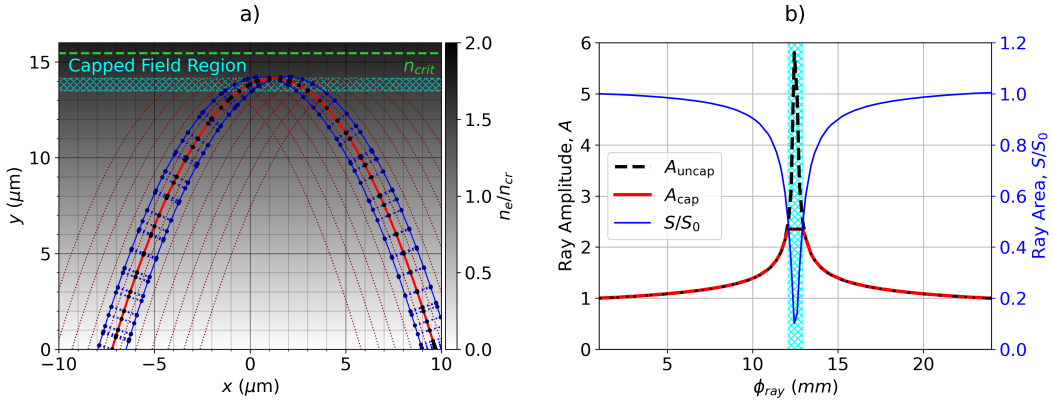


Figure 1.10: A demonstration of how the ray-amplitude is obtained from the area of neighbouring-rays for a beam propagating up a linear density gradient. Fig. a) explicitly shows the trajectory of a main-ray and its neighbour-rays in red and blue respectively, explicitly highlighting the beam's caustic region, where the amplitude of the light is capped. Fig. b) plots the area of the main-ray in blue (which goes through a minimum at the caustic location), as a function of the phase of the ray. Also shown are the uncapped and capped amplitudes of the ray.

of the plasma. For OMEGA scale direct-drive simulations, an initial separation of $\Delta l \lesssim 1 \mu\text{m}$ is found to give converged behaviour. If the separation is too small however, floating point arithmetic can lead to noise in the ray-amplitude estimation. For all simulations presented in this thesis, $\Delta l = \lambda_0/10 \ll 1 \mu\text{m}$ was used.

As mentioned in Sec. 1.3.4, it was found that the Kaiser algorithm for ray propagation, which uses a single ∇n_e in each grid cell and discontinuously refracts rays at cell boundaries, led to large levels of noise in the ray-amplitude profiles. In order to obtain smooth profiles for A , linear interpolation of ∇n_e was found to be necessary. The continuously varying ∇n_e , which does not have discontinuities across cell interfaces, allows a smoothly varying area for each ray to be obtained.

Fig. 1.10.a demonstrates this amplitude reconstruction process in a purely illustrative example of a beam travelling up a linear density gradient at an angle, leading to a caustic at its turning point. The trajectory of several main-rays are plotted in dark-dashed red, and a single main-ray is highlighted in a brighter shade of red. The two neighbour-rays of this highlighted main-ray are plotted in blue. Note that in this figure, the default initial main-neighbour-ray separation of $\Delta l = \lambda_0/10 = 0.035 \mu\text{m}$ was used, but the separation has been magnified on the plot to visualise the amplitude reconstruction from the area more clearly. The locations of the main- and neighbour-rays after a single step of each main-ray are plotted as black and dark-blue spots respectively. The 'area' of the neighbour-rays S , which in this 2-D ray-trace example here is simply a distance, is plotted on 1.10.a as a dashed blue line between the neighbour-rays. The neighbour-rays are pushed until they have the same phase as the main-ray, at which point the area is evaluated.

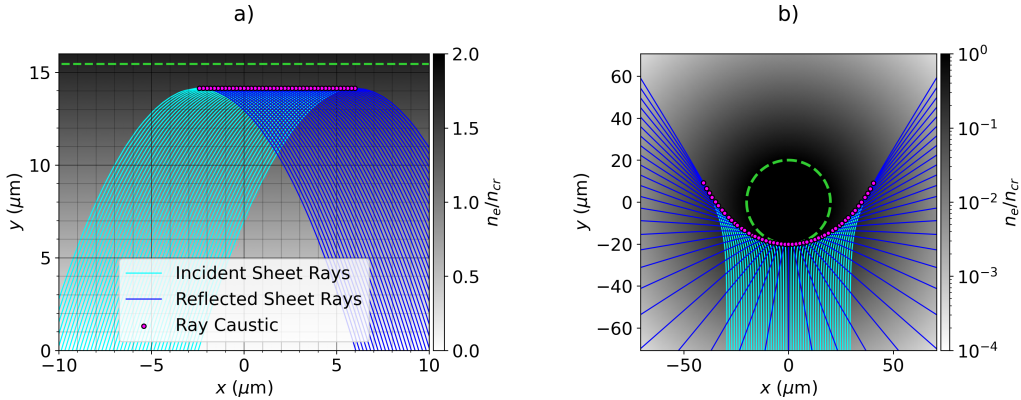


Figure 1.11: An illustration of the concept of caustics and ray sheets. In a), the trajectory of rays traversing up a linear density gradient are plotted. Separate colours are used for the incident and reflected sheets, which are separated by a caustic. In b), rays propagate up a density profile, $n_e = n_{cr} \exp [-(r_{\mu m} - 20)/100]$. Unlike in a), the ray caustics do not occur at their turning point, *i.e.* the minimum radius.

1.4.1.1 Caustics and Ray-Sheets

Caustics are an important concept in GO, and the reconstructed field in their vicinity must be handled correctly in order to accurately model CBET in ray-based codes. Fig. 1.10.b plots the area of the main-ray as a function of main-ray phase in blue. At $\varphi_{ray} \sim 12 \mu m$, $S \rightarrow 0$, *i.e.* neighbouring-rays cross over each other, which is known as the ray-caustic. In the absence of caustics, rays never cross over each other and therefore the mapping from ray phase-space (beam-port locations, where $\tau = 0$) to real-space is single-valued, or in other words each point in space will be reached by (at most) one ray from each beam. In the presence of caustics, this single-valued mapping breaks down and a single real-space location is accessible by multiple ray launch locations. A single-valued mapping is still possible if each beam is separated into distinct ‘sheets’ after caustics, where each sheet still has a single-valued projection from phase-space to real-space.

This is illustrated in Fig. 1.11.a, where rays from a single beam are plotted propagating up a linear density gradient with $n_e = n_{cr} y_{\mu m} / 15.5$. As the density gradient is purely in the y direction, each ray has translational symmetry in x and therefore each ray-caustic is located at the ray turning point, $y \sim 14 \mu m$. The portions of the ray trajectories that fall before and after the caustic are separated into the ‘incident’ and ‘reflected’ sheets respectively and plotted in separate shades of blue. Fig. 1.11.b also plots rays from a single beam, but now propagating through a cylindrically symmetric n_e profile. As can be seen from this figure, the caustic is not the same as the ray turning-point¹¹, but it is the location that the amplitude diverges.

Unless the amplitude is tracked along each ray trajectory, the location of the caustic cannot be identified and rays cannot be separated into distinct sheets, both of which have important ramifications for ray-based CBET models. Firstly, because the amplitude diverges, the field values can become large and therefore must be capped to diffraction limited values

¹¹Defined here as the location of maximal n_e experienced along the ray trajectory.

(the SOLAS methods for this are discussed in more detail in Sec. 1.4.2). The power change of rays due to CBET scales exponentially with field strength squared, so erroneously large field values are extremely problematic to accurately computing power changes. Additionally, if the beam cannot be separated into distinct sheets, then self-CBET, where the reflected component of a beam interacts with the incident component of the same beam, must be neglected. In SOLAS, the neighbour-ray method allows the amplitude to be tracked along each ray, enabling caustic location identification and sheet-separation. Currently, it is assumed that each sheet has two components, *i.e.* an incident and reflected field, but it should be possible to extend this to multiple caustics to accurately model complex CBET interactions such as target-stalk simulations [54–56]. This is an advantage of the forward ray-tracing approach to CBET modelling, compared to inverse-ray-tracing, where only plasma profiles that result in a single caustic can be modelled [20].

The phase of the light is also evolved along each ray trajectory in equations 1.3, and therefore the coherent sum of all electric fields can be reconstructed which involves interference between sheets. The total electric field is,

$$E = \sum_j^{\text{sheets}} |E_j| \exp(i(k_0\varphi_j - \pi\alpha_j/2)), \quad (1.15)$$

where k_0 is the vacuum wavevector of the light and α_j accounts for the $\pi/2$ phase shift that occurs when a ray changes sheet, *i.e.* $\alpha_j = 0$ for the incident sheet and $\alpha_j = 1$ for the reflected sheet [34].

The fields are discretised on the SOLAS mesh by nearest neighbour interpolation from the ray to the cell. When multiple rays from the same sheet pass through a cell, then the inverse-distance weighted average of the mid-point along the ray step to the cell centre is used to compute the field value for the cell. This leads to a field structure, $|E_j|(\mathbf{x}, \mathbf{k}, \omega, \phi)$, where j refers to each sheet, \mathbf{x} is the spatial location of the field which refers to the cell the field is stored in, and \mathbf{k}, ω, ϕ are the wavevector, frequency and phase of the ray. For many beam simulations, there is a large associated memory cost to store this information on the mesh, which is discussed in more detail in Sec. 1.5.4. When computing the effect of CBET, it is also necessary to interpolate the fields stored at the cell centre to the ray trajectories. Nearest neighbour interpolation is also used for this step, so rays experience a constant value for $|E_j|(\mathbf{x}, \mathbf{k}, \omega, \phi)$ throughout the cell. It is technically possible to use higher order interpolation for both stages, either from an unstructured mesh of the ray locations, or from the SOLAS mesh, which is close to logically rectilinear. The second of these options was tested but proved both to be the dominant computational cost for many beam CBET interactions and also challenging to robustly implement for non-Cartesian meshes, because the angular resolution for typical spherical direct-drive simulations was too coarse for the required accuracy.

1.4.2 Caustic Field Capping

In the vicinity of beam-caustics, the electric field magnitude of a beam is limited by diffraction which is neglected in GO. Therefore, ray-based models which do not cap fields near caustics can experience divergent electric fields. For direct-drive simulations, a significant amount of CBET occurs near caustics and therefore sensibly capping the field value is crucial for accurate simulations [25]. This cannot be achieved without knowledge of the caustic location, which is a severe limitation to the predictive capability of CBET codes that do not track the amplitude. This section describes two methods that have been implemented to cap the field values in the vicinity of laser caustics, the Field Limiter (FL) and Etalon Integral (EI) approaches.

Field Limiter This is a straightforward hard cap on the maximum value of the electric field reconstructed during the ray-trace. The electric field of light propagating up a linear density gradient has the analytic solution of an Airy function. The field limiter approach is to cap all electric fields to this value,

$$\frac{|E|}{|E(\tau = 0)|} = \sqrt{\frac{P(\tau)}{P(\tau = 0)}} \min \left[A, \sqrt{\zeta} \left(\frac{n_t}{n_{cr}} \right)^{1/4}, \sqrt{\zeta} \sqrt{\frac{S(\tau = 0)}{S(\tau)}} \right],$$

$$\zeta = 0.9 (\omega L/c)^{1/3},$$

$$L = n_{cr}/|\nabla n_e|_t,$$
(1.16)

where n_t is the electron density at the caustic and $|\nabla n_e|_t$ is the magnitude of the electron density gradient at the caustic location [33, 36, 57]. The first term in the minimum is the standard field reconstruction from the amplitude away from caustics. The second term is the maximum of the Airy function and the third term is an improvement to the second term for near-normally incident rays [34]. Fig. 1.10.b plots the uncapped and capped amplitudes obtained from the field limiter approach for light propagating at an angle to a linear density gradient.

Etalon Integral The EI method is an improvement to the FL, which allows for deviations in the density profile away from linearity [24, 58, 59]. Several distinct types of caustic exist for different geometries of problem. For example in direct-drive, the light reflecting from the critical surface forms a ‘fold’-type caustic, whereas focussing light leads to a more complex ‘cusp’-type caustic [60]. If the form of the caustic is assumed, then an approximation to the total field in the vicinity of the caustic is formulated, which allows for deviations from the ideal case. In the example of the direct-drive fold caustic, the field is assumed to be the sum of an Airy function and its derivative, which accounts for the deviations from linearity. An expression for the total field can be derived in terms of the ray-amplitude and phase before

(A_1, φ_1) and after (A_2, φ_2) the caustic,

$$\begin{aligned} E_T &= \sqrt{\pi} [(-\xi)^{1/4}(A_1 + A_2)\text{Ai}(\xi) - i(-\xi)^{1/4}(A_1 - A_2)\text{Ai}'(\xi)] e^{i(k_0\chi - \pi/4)}, \\ \chi &= \frac{1}{2}(\varphi_1 + \varphi_2), \\ \xi &= -\left[k_0 \frac{3}{4}(\varphi_2 - \varphi_1)\right]^{2/3}, \end{aligned} \quad (1.17)$$

where Ai and Ai' are the Airy function and its derivative. In SOLAS, Ai and Ai' are computed numerically using the `special-functions` library [61]. This total field can then be divided between the incident and reflected sheet by inversion of Eq. 1.15 assuming that $|E_1| = |E_2|$,

$$\frac{|E_j|}{|E_{j,0}|} = \frac{\sqrt{W_j} |E_T|}{\sqrt{2} [1 + \sin(\varphi_2 - \varphi_1)]^{1/2}}. \quad (1.18)$$

The assumption of equal fields is approximately valid for OMEGA scale direct-drive conditions, where the caustic region is small compared to the plasma scales and therefore ray powers are assumed to not vary significantly over this distance. The Etalon integral is applied in the ‘caustic-region’, which in Refs. [24, 62, 63], is stated to be equivalent to,

$$|\varphi_1 - \varphi_2| \leq \lambda_0/2, \quad (1.19)$$

where λ_0 is the vacuum wavelength of the light.

Applying the EI method requires evaluation of Eq. 1.19 to determine if a ray is inside its caustic region, which relies on interpolation of the phase of the other sheet from the same beam onto the ray location. If using nearest neighbour interpolation, such as in SOLAS for interpolation of all field quantities onto rays, a grid resolution of $\Delta \ll \lambda_0$ must be used, which is a much higher resolution than is required for ray-tracing and CBET without the EI. Therefore, the EI method is only used in SOLAS simulations for high resolution grid test problems, such as those Sec. 1.4.3. The alternative approach is to implement linear interpolation from the field quantities of all beams onto ray locations, such as in Ref. [34]. This was not deemed a viable approach however, because the mesh resolution for spherical simulations was found to not be well-enough angularly resolved to interpolate the phase with sufficient accuracy to the rays. The standard procedure for CBET simulations in SOLAS is to use the FL approach, which was found to give satisfactory results compared to the EI method.

1.4.3 Field Reconstruction Validation

In this section, several test problems will be presented that compare electric fields obtained using the SOLAS field solver in the absence of CBET, to those from the wave based solver LPSE in direct-drive relevant plasma profiles. The LPSE results are presented in Ref. [34], and are available from the repository [64]. In all the following test problems, the laser has a vacuum wavelength, $\lambda_0 = 0.351 \mu\text{m}$ and a super-Gaussian intensity profile, defined in Eq. 1.1. All 1-D and 2-D validation problems assume lasers polarised out of the simulation plane along the

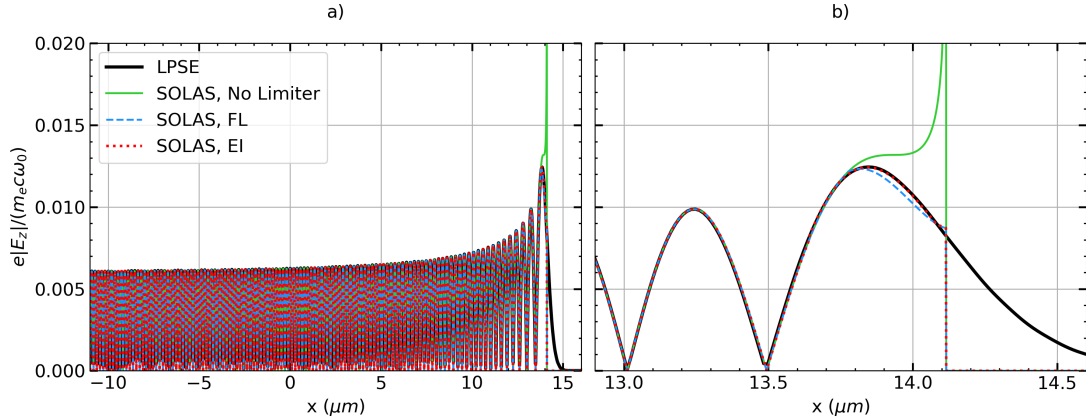


Figure 1.12: Results of the 1-D field reconstruction test, comparing SOLAS fields with different caustic field capping methods to the LPSE results. Panel a) shows the oscillatory behaviour of the field solution which arises due to the interference between the incident and reflected sheet. Panel b) plots the same results, but zoomed in on the caustic region to demonstrate the differences in fields obtained from the different methods.

z axis. The plasma density profiles are given by,

$$n_e(r) = n_0(d/r)^m, \quad (1.20)$$

where $n_0/n_{\text{cr}} = 1.165$, $d = 343 \times S \mu\text{m}$, $m = 3.78$ and S changes the scale of the density profile, where $S = 1$ corresponds to scale lengths from implosions using the full OMEGA laser-energy. These values were obtained from fitting the equation to 1-D Rad-Hydro calculations using the LILAC code.

1.4.3.1 1-D Reflected Beam

The first validation problem is for the case of light propagating normally up a density gradient. For this problem, 1-D Cartesian geometry was used, so the density profile was obtained by transforming the spatial coordinate from equation 1.20, $r \rightarrow x - 36.42 \mu\text{m}$. The beam is travelled in the $+\hat{x}$ direction, with $I_0 = 14 \text{ W/cm}^2$. Only a single ray was used because the ray-trace is completely 1-D. A scale factor of $S = 1/16$ was used, resulting in a critical surface at $x \sim 14.14 \mu\text{m}$. The simulation had bounds $x \in [-16, 20] \mu\text{m}$ with a resolution of $\Delta x \sim 1 \text{ nm}$. A high resolution was used here in order to resolve the highly oscillatory coherent field sum and also enabled use of the EI field capping method. Power changes of the rays due to Inv-Brem and CBET were also neglected.

The laser in this problem travelled up the density gradient, reflecting from the critical surface. For light travelling normally up a density gradient, the critical density is the location of the caustic, because the ray area, $S(\tau)$, is constant and therefore the amplitude diverges when $\epsilon \rightarrow 0$. The total field is given by the coherent sum between the incident and reflected sheets. Fig. 1.12.a shows the LPSE result compared to the field obtained from SOLAS without a cap on the caustic field; using the FL approach; and using the EI approach. The only difference

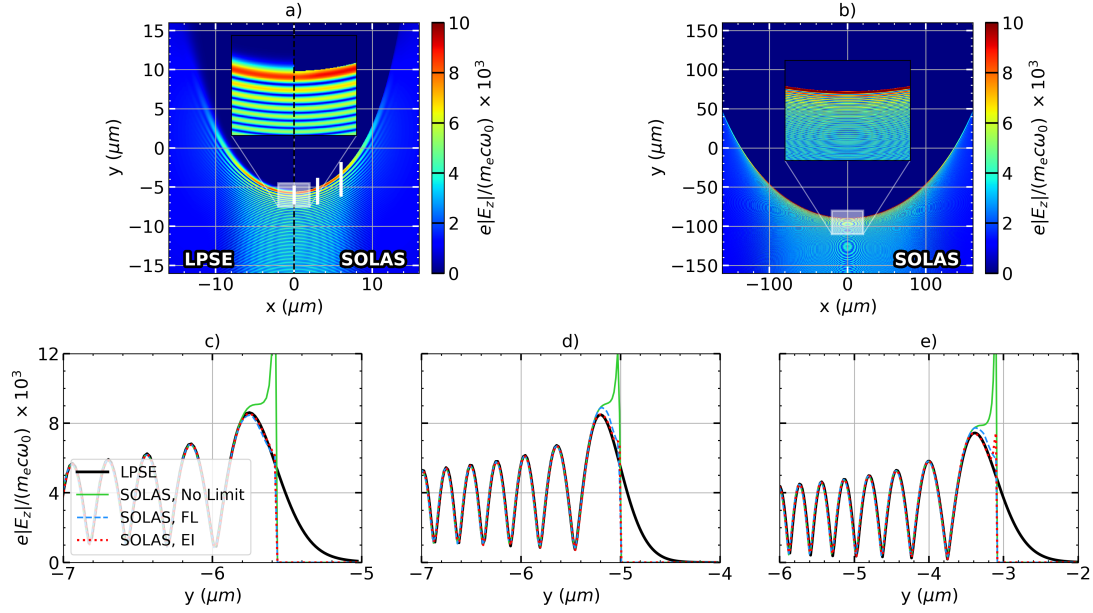


Figure 1.13: Results of the 2-D field reconstruction test. Panel a) plots the field from LPSE on the left side and the SOLAS field on the right for the 1/64 OMEGA scale simulation. Panel b) shows the SOLAS field from the 1/4 scale simulation which, when compared to a), demonstrates that as scale increases, the relative size of the caustic region decreases. Panels c), d) and e) are lineouts near the caustic region along y from the 1/64 scale simulations at $x = 0, 3$ and $6 \mu\text{m}$ respectively, the positions of which are indicated by the white lines on a). Note that the circular features in the field in panels a) and b) arise due to aliasing artefacts between the true solution scale, with the resolution of the image and/ or simulation grid.

between the SOLAS methods occurs in the caustic region¹², shown more clearly in Fig. 1.12.b, which in this problem is for $x > 13.64 \mu\text{m}$. Failure to cap the caustic field leads to a divergent $|E_z|$ at the critical surface, but both the EI and the FL methods show good agreement with LPSE. This justifies the default use of the simpler FL method for SOLAS CBET calculations.

Standard GO cannot capture the field beyond the critical surface because rays cannot propagate beyond $\epsilon = 0$. The evanescent field in this region can be reproduced in the complex-GO framework, which integrates rays which have complex-valued properties and can thus be evolved beyond the critical surface [24]. This, however, is not deemed to be necessary for accurate CBET modelling of OMEGA-scale direct-drive implosions.

1.4.3.2 2-D Reflected Beam

A second field reconstruction test was also implemented in 2-D geometry. Unlike the previous 1-D test, the reconstructed field for this problem also depends on the divergence of neighbouring rays. This is because apart from normally incident rays at the centre of the beam, $\mathbf{k} \nparallel \nabla n_e$, so the area, $S(\tau)$, of the rays vary. Simulations at 1/64 and 1/4 scales are presented here. The $S = 1/64$ simulation bounds were $x, y \in [-20, 20] \mu\text{m}$ and resolution

¹²i.e. where equation 1.19 is satisfied.

$\Delta \sim 20$ nm. The $S = 1/4$ simulation bounds were $x, y \in [-200, 200]$ μm and resolution $\Delta \sim 100$ nm. For both scales, a single beam propagated parallel to $+\hat{y}$ and was centred on $x = 0$ μm . The beam widths were $\sigma = 8$ and 115 μm for the 1/64 and 1/4 scales respectively. The standard uniform sampling procedure described in Sec. 1.3.3 was used with $C_N = 2$. CBET and Inv-Brem were again both neglected.

Fig. 1.13.a shows the LPSE and SOLAS, FL fields for the $S = 1/64$ setup. Qualitative agreement is good between LPSE and the ray-based field in the sub-critical plasma. The field from the SOLAS FL $S = 1/4$ simulation is plotted in Fig. 1.13.b, from which it can be seen that the caustic region, which has a characteristic width $\sim \lambda_0$, shrinks in relative size as the scale increases. This suggests that at increasing scale, the importance of accurate caustic modelling may decrease in importance. Plotted in Figs. 1.13.c, 1.13.d and 1.13.e are lineouts from the 1/64 simulations taken at $x = 0, 3$ and 6 μm respectively. They all include LPSE and SOLAS results with FL, EI caustic field capping along with no limiting. These plots demonstrate that caustic field limiting is necessary to compare favourably to the LPSE solution and that the FL approach slightly overestimates the caustic field compared to LPSE and the EI method. The discrepancy between the FL and EI results is again deemed sufficiently small to justify the default use of the simpler FL approach. To remind the reader, this choice is because the implementation of the EI method in SOLAS requires grid resolution $\Delta \ll \lambda_0$, the reason for which is described at the end of Sec. 1.4.2.

1.5 Ray-Based CBET Model

This section describes the implementation of the CBET model in SOLAS. Fig. 1.14 shows a flowchart which illustrates a broad overview of the operational loop of the CBET model when coupled to CHIMERA. The initial ‘field reconstruction’ ray-trace in the absence of CBET, follows the procedure described in Sec. 1.4 to obtain the field for every sheet on the SOLAS mesh. Ray-based CBET models, including the model in SOLAS, typically must perform repeated ray-traces through the same hydrodynamic profiles to account for pump depletion and optionally energy conservation.

The pump depletion loop, described in more detail in Sec. 1.5.5, is a fixed point iteration method to obtain the new CBET laser fields. This loop is necessary as each iteration produces a new background field which leads to a different CBET interaction, which converges when CBET has been fully accounted for. The resultant solution will not necessarily conserve energy if CBET occurs in the presence of laser caustics, due to errors in field reconstruction and CBET scattering in these locations. To remedy this, additional energy conservation iterations can be performed, where a multiplier on the CBET gain in caustics can be varied to conserve laser energy. Although this is an ad-hoc correction, it is found to lead to better agreement with higher fidelity solver, as is explicitly demonstrated in Sec. 1.5.7.3.

CBET does not affect the trajectory of light, only its power and therefore repeating the calculations of ray trajectories is both computationally costly and unnecessary. Ray locations are therefore stored in a memory-efficient, linked-list to be re-used in both loops. It was found in SOLAS that caching the ray locations in this manner typically leads to an order of

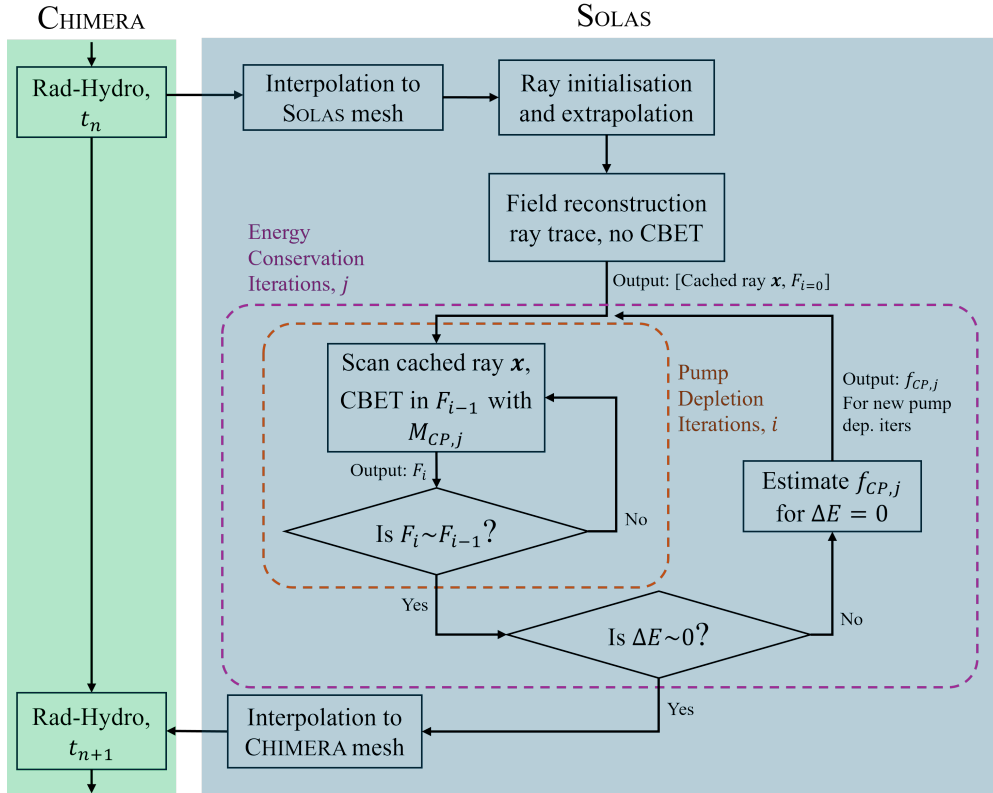


Figure 1.14: The SOLAS CBET model operation loop. F_i is shorthand for the total field from all sheets at pump depletion iteration i and f_{CP} is the modifier to the caustic pump multiplier, described in Sec. 1.5.6 of the j^{th} energy conservation iteration. ΔE denotes the energy conservation error, which is the total incident power minus deposited power exiting the grid.

magnitude speed up compared to performing a new ray-trace for every iteration.

1.5.1 Power Change of Rays due to CBET

Ray-tracing calculations assume steady-state hydrodynamic profiles for rays propagating through the plasma and that the field of a ray propagates as a plane wave along the ray path [65]. The linear gain theory of SBS, which describes the steady-state energy change of locally plane wave light which passes through uniform plasma conditions, can therefore be used [15, 21]. ‘Linear’ in this context means that the plasma response to the driving fields is sufficiently small to be treated by a linear expansion. The uniform assumption here means that the plasma conditions must not vary significantly over the interaction time or length scales. For direct-drive conditions, hydrodynamic time scales are typically $\sim 100\text{ps}$ and CBET saturates on the order of $\sim 10\text{ps}$. Ray steps are also limited to grid cell boundaries, which are smaller than hydrodynamic length-scales, so it is safe to assume a locally uniform plasma background when this model is applied only over a single ray step at a time.

The steady-state interaction between two parallel-polarised sheets (i, j) over a path length $d\tau$ can be written in terms of the field magnitude of the sheet ($|E_{i,j}|$) or equivalently ray

power ($P_{i,j} = A_{i,j}|E_{i,j}|^2$),

$$\begin{aligned}\frac{d|E_i|^2}{d\tau} &= (-\kappa_{IB} + \gamma_{ij}|E_j|^2)|E_i|^2, \\ \frac{dP_i}{d\tau} &= (-\kappa_{IB} + \gamma_{ij}A_j P_j)P_i,\end{aligned}\quad (1.21)$$

where κ_{IB} is the Inv-Brem absorption kernel, A_j is the amplitude of sheet j and γ_{ij} is the CBET gain of sheet i from the interaction with sheet j . The sheet/ray which changes energy in a given interaction (here i), is often called the *probe* while the other beam is termed the *pump*. The gain is a function of both the plasma conditions and the local field profiles for both sheets in the interaction, so a gain must be calculated between every pair of sheets at every location where both are present. Going from the first to the second equation assumes that $dA_j/d\tau = 0$, which is consistent with the assumption from the linear gain theory that the fields are approximately uniform over a small step. Different models exist for the gain, which either use a fluid or kinetic treatment for the plasma IAW response.

When multiple different probe beams are present, the total CBET interaction is treated simply as the sum of all interactions from different sheets,

$$\frac{dP_i}{d\tau} = (-\kappa_{IB} + \kappa_{CBET})P_i, \quad (1.22)$$

where the CBET kernel has been defined $\kappa_{CBET} = \sum_{j \neq i} \gamma_{ij}|E_j|^2$. This summation assumes that the fields from different sheets are uncorrelated. For direct-drive conditions, this assumption is broadly correct, apart from when a probe sheet undergoes a CBET interaction in the caustic region of the probe. In this case, the *Coherent Caustic* correction is applied, which is described in Sec. 1.5.3.

Note that when computing both Inv-Brem and CBET, the partition of power lost to each interaction can be computed as,

$$\begin{aligned}\Delta P_{i,IB} &= -\langle P_i \rangle \frac{\kappa_{IB}}{\kappa_{CBET} - \kappa_{IB}}, \\ \Delta P_{i,CBET} &= \langle P_i \rangle \frac{\kappa_{CBET}}{\kappa_{CBET} - \kappa_{IB}}, \\ \langle P_i \rangle &= P_i + P_i(\kappa_{CBET} - \kappa_{IB})d\tau/2,\end{aligned}\quad (1.23)$$

where $\Delta P_{i,IB}$ and $\Delta P_{i,CBET}$ are the powers lost to Inv-Brem and CBET respectively and $\langle P_i \rangle$ is the average power of the ray over the step, $d\tau$. This can be derived by solving Eq. 1.21 for P_i and then taking the limit $d\tau \rightarrow 0$ [28]. The deposition, $\Delta P_{i,IB}$, can then be interpolated to the grid as an electron energy source as is described in Sec. 1.3.4.

The two formulations of the gain are presented below. Broadly, the gain describes the plasma response to the 2 driving fields and therefore dictates the energy transfer between them. They differ in that the fluid formulation arises by deriving a gain from linearised fluid equations for the plasma response, whereas the kinetic formulation is obtained from a linearisation of the Vlasov equation. The kinetic gain is more complete and should be used for comparison to experimental observables, whereas the fluid gain is useful for comparison with LPSE, which directly solves the linearised fluid equations.

Fluid CBET Gain The linear fluid gain, derived by Randall *et al.* in Ref. [21] is,

$$\begin{aligned}\gamma_{ij} &= \frac{n_e e}{4m_e c \omega_i} \frac{1}{T_e (1 + 3T_i/Z T_e)} \frac{R(\eta_{ij})}{\nu_{ia}}, \\ R(\eta_{ij}) &= \frac{(\nu_{ia}/\omega_s)^2 \eta_{ij}}{(\eta^2 - 1)^2 + (\nu_{ia}/\omega_s)^2 \eta_{ij}^2}, \\ \eta_{ij} &= \frac{(\omega_j - \omega_i) - \mathbf{k}_s \cdot \mathbf{u}}{\omega_s},\end{aligned}\quad (1.24)$$

where T_e and T_i are the electron and ion temperatures in eV respectively, ω_i and \mathbf{k}_i are the frequency and wavevector of sheet i respectively, Z is the ionisation state, \mathbf{u} is the fluid velocity, $\omega_s = |\mathbf{k}_s|c_s$ is the IAW frequency, $\mathbf{k}_s = \mathbf{k}_j - \mathbf{k}_i$ is the IAW wavevector, $c_s = \sqrt{e(Z T_e + 3T_i)/m_i}$ is the sound speed and ν_{ia} is the IAW damping rate. This formulation is useful for comparison with LPSE, which directly solves the linearised fluid equations and therefore in situations where the GO assumptions are valid, the two methods should give similar results. However, it is generally not considered to be a good choice of model to compare to experiment. The damping rate, ν_{ia} does not have an analytic formula for arbitrary plasma conditions and therefore must be prescribed. Additionally, Eq. 1.24 assumes an average ion treatment of the species in the plasma if multiple ion species are present. In reality, both fast and slow modes of IAW can be driven in a 2-species plasma [66], which can independently lead to CBET scattering. This effect cannot be captured using the fluid gain, where the plasma is assumed to be made of a single ion species with a number density averaged ion mass. Codes that use this formulation typically use a damping value $\nu_{ia}/\omega_s = 0.2$ for CH plasmas, which is the value used for all fluid gain simulations in this chapter.

Kinetic CBET Gain The linear kinetic CBET gain, described by Michel in Ref. [67] is,

$$\begin{aligned}\gamma_{ij} &= \frac{e^2 |\mathbf{k}_s|^2}{4m_e^2 c \omega_i^3} \text{Im}(K_{ij}), \\ K_{ij} &= \frac{\chi_e(1 + \chi_i)}{(1 + \chi_e + \chi_i)}, \\ \chi_e &= \frac{-1}{2|\mathbf{k}_s|^2 \lambda_{De}^2} Z' \left(\frac{(\omega_j - \omega_i) - \mathbf{k}_s \cdot \mathbf{u}}{\sqrt{2} |\mathbf{k}_s| v_{Te}} \right), \\ \chi_i &= \frac{-1}{2|\mathbf{k}_s|^2 \lambda_{De}^2 \langle Z \rangle T_i} \sum_{\alpha}^{\text{species}} f_{\alpha} Z_{\alpha}^2 Z' \left(\frac{(\omega_j - \omega_i) - \mathbf{k}_s \cdot \mathbf{u}}{\sqrt{2} |\mathbf{k}_s| v_{T\alpha}} \right),\end{aligned}\quad (1.25)$$

where χ_e and χ_i are the electron and ion susceptibilities respectively, f_{α} and Z_{α} are the number fraction and ionisation of ion species α respectively, Z' is the derivative of the plasma dispersion function, $v_{Tn} = \sqrt{e T_n / m_n}$ is the thermal velocity of species n with temperature T_n in eV and mass m_n , $\lambda_{De} = \sqrt{\epsilon_0 e T_e / n_e e^2}$ is the electron Debye length and $\langle Z \rangle = \sum_{\alpha} f_{\alpha} Z_{\alpha}$ is the average ionisation. Note that the susceptibilities $\chi_{i,e}$ are complex. In order to compute Z' in SOLAS, the CALGO library is used to numerically compute the value of the *Faddeeva function*, $w(x)$ [68]. This is then related to the plasma dispersion function and its derivative

by,

$$\begin{aligned} Z(x) &= i\sqrt{\pi}w(x), \\ Z'(x) &= -2[1 + xZ(x)], \end{aligned} \tag{1.26}$$

where $i = \sqrt{-1}$ and $w(x)$, $Z(x)$ and $Z'(x)$ are all complex numbers [69]. Unlike the fluid gain, this theory correctly captures the resonance and has no effective free parameters, making it the judicious choice for predictive simulations. The plasma dispersion function is however relatively slow to numerically evaluate and dominates computational runtime if evaluated every ray step. SOLAS therefore calculates γ_{ij} between each sheet in every grid cell at the end of the field reconstruction ray-trace (from Fig. 1.14) and then interpolates this pre-calculated value onto the ray locations for the pump-depletion iterations. This reduces computational runtimes by orders of magnitude for many beam direct-drive simulations, but has an associated memory overhead, which is discussed in more detail in Sec. 1.5.4. All simulations in this thesis use the kinetic CBET gain unless explicitly stated otherwise.

Random Polarisation Correction The gains calculated above all assume that the interacting fields have parallel polarisations. For many laser systems, beams may have arbitrary or random polarisations, such as at the OMEGA laser facility where Distributed Polarization Rotators (DPRs) separate each beam into 2 orthogonally polarised sub-beams which overlap to effectively have one spot with random polarisation [70]. If a simulation is conducted with multiple beams of random polarisation, a *Polarisation Smoothing* multiplier, M_{PS} , must be applied to the value of γ_{12} which accounts for random polarisation angles between the field from different sheets,

$$M_{PS} = \frac{1}{4}(1 + \cos^2 \theta), \tag{1.27}$$

where θ is the angle between the wavevectors of the interacting sheets.

MAYBE TRANSFER BELOW TO THEORY SECTION!

In reality, the DPRs on OMEGA do not actually create a single, mixed polarisation laser spot, but 2 slightly offset sub-beams on the target. CBET models which track polarisation or rays have been developed which account for the true polarisation angle between 2 sheets [71–74]. These models have demonstrated that polarised CBET on OMEGA creates a mode-1 which is always in the same direction. This persistent mode-1 was experimentally observed from neutron time of flight diagnostics before its origin was understood [75].

1.5.2 Caustic Gain Truncation

For rays propagating through SOLAS cells, nearest neighbour interpolation is used to interpolate field quantities to the rays. This is generally an adequate approximation for field magnitudes, frequencies and wavevectors, which vary over greater length scales than typical cell resolutions $\mathcal{O}(1\mu\text{m})$, apart from in the vicinity of a caustic [34]. Near caustics, rays turn sharply and fields have a sharp cut-off, dropping to zero sharply, as be seen in the lineouts from Fig. 1.13. The sharp turning of rays mean that \mathbf{k} can vary rapidly within a cell. Although SOLAS does have variable radial resolution, as described in Sec. 1.4, this resolution

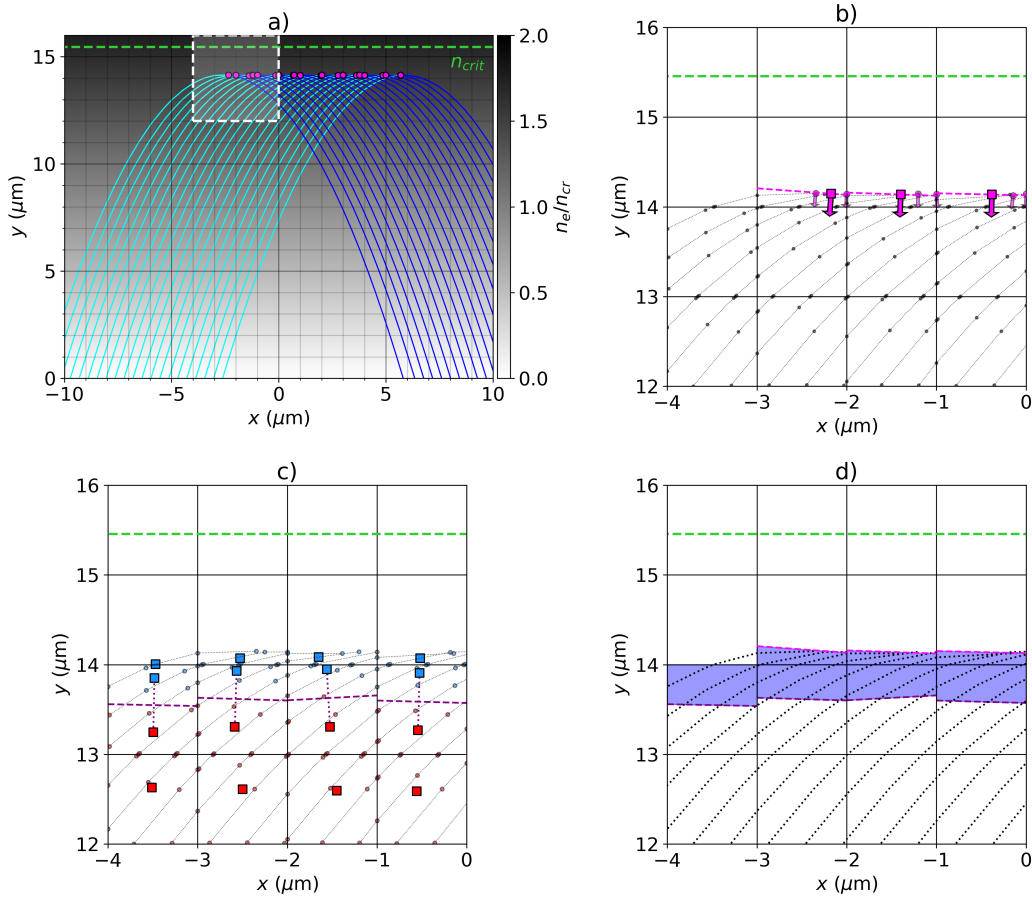


Figure 1.15: Illustration of the CGT and caustic region identification algorithms. Panel a) shows a laser, separated into incident and reflected sheets by a caustic, propagating up and reflecting in a linear density ramp. CGT is illustrated in b) where a cell is separated into a *lit* and *unlit* region by the reconstructed *caustic plane* (dashed magenta line). Panels c) and d) illustrate the method used to identify the *caustic region* (shaded blue), where the coherent caustic modifier is applied. c) shows that cells are geometrically separated into *capped* (blue squares) and *uncapped* (red squares) regions and the coherent caustic modifier to the gain is applied in this capped, caustic-region.

is limited to the minimum radial cell size from the hydrodynamic grid, which is not dictated from laser parameters and cells are typically larger than the caustic region width $\mathcal{O}(\lambda_0)$. The issue of \mathbf{k} variation is not addressed in SOLAS, but linear interpolation or a truly adaptive mesh, separate from the CHIMERA grid could be implemented to address this.

The field cut-off is an issue however, as it can significantly affect energy conservation in ray-based CBET models. CGT is an algorithm that effectively improves the resolution of the grid near laser caustics [33]. This method separates cells into *lit* and *unlit* regions. If rays travel in the *unlit* region, then the CBET gain is not applied. For example, Fig. 1.15.a shows a beam propagating up a linear density gradient, separated by the caustic into incident and reflected sheets. Fig. 1.15.b shows a zoomed in view of in the vicinity of the caustic of the incident sheet ray locations, plotted as grey dots. If a ray from another beam were present

with $14.3 \lesssim y < 15 \mu\text{m}$, nearest neighbour interpolation would lead to the ray undergoing a CBET interaction in this *unlit* region, where no rays from the pump sheet are present. Field magnitudes in this caustic region are typically large, so even though this is a small region of space, it can lead to significant errors, especially at lower resolutions.

The CGT algorithm described by Follett in Ref. [33] defines the *lit* region for each sheet by creating a mesh of the caustic locations from every ray on the sheet and only applying CBET gains in on the side of this mesh that rays traversed. A different algorithm has been developed for SOLAS, which geometrically splits each cell into *lit* and *unlit* regions by a *caustic plane* if at least one ray caustic occurs in the cell. The *caustic plane*¹³ is defined by a point \mathbf{x}_{caus} and normal $\hat{\mathbf{n}}_{\text{caus}}$. The location, \mathbf{x}_{caus} , is simply the average of all ray caustic locations from the sheet present in the cell, for example shown in Fig. 1.15.b by the small pink circles for each ray caustic and the larger pink square for the cell averaged location. The normal is estimated by the average over all ray caustics in the cell of the ray tangent vector just after the caustic $\hat{\mathbf{t}}_{\text{After}}$, minus the velocity just before $\hat{\mathbf{t}}_{\text{Before}}$,

$$\hat{\mathbf{n}}_{\text{caus}} = \left\langle \frac{\hat{\mathbf{t}}_{\text{After}} - \hat{\mathbf{t}}_{\text{Before}}}{|\hat{\mathbf{t}}_{\text{After}} - \hat{\mathbf{t}}_{\text{Before}}|} \right\rangle, \quad (1.28)$$

such that the normal points to the lit side. This is plotted in Fig. 1.15.b as small pink arrows for each ray caustic normal and the large arrows in each cell for the cell averaged value. The planes defined by these points and normals for each cell that contains a sheet caustic is shown as a pink dashed line. If a probe ray at location $\mathbf{x}_{\text{probe}}$ is propagating in a cell where there is a pump sheet caustic, it will only experience a CBET interaction if $\hat{\mathbf{n}}_{\text{caus}} \cdot (\mathbf{x}_{\text{probe}} - \mathbf{x}_{\text{caus}}) > 0$. Rays from other sheets also have their steps limited by the caustic plane.

This is a slightly lower fidelity implementation of the more complete CGT model from Ref. [33]. The model implemented by Follett can represent caustics which, within a grid cell, are not locally well approximated by planes. The SOLAS model is however simpler to implement and also acts to effectively increase the resolution of the cells near caustics. The caustic test problem presented in Sec. 1.5.7.2 illustrates the effectiveness of the SOLAS-CGT model at reducing energy conservation errors for caustic CBET interactions where the grid cells are significantly larger than the caustic region.

1.5.3 Coherent Caustic Correction and Caustic Region Identification

In Sec. 1.5.1, in order to obtain Eq. 1.22, it was assumed that when a ray undergoes CBET interactions with multiple pump sheets, the field from the pump sheets can be treated independently. This is equivalent to assuming that over a ray propagation path, $d\tau$, the fields from the sheets do not add coherently,

$$\int d\tau \sum_j^{\text{sheets}} |E_j|^2 \approx \int d\tau \left| \sum_j^{\text{sheets}} E_j \right|^2, \quad (1.29)$$

¹³In cylindrical and spherical simulation geometries, the ‘planes’ are defined in the native coordinate system, which creates manifolds that better reflect the assumed geometry of the problem.

where E_j is the field from the j^{th} sheet. Eq. 1.29 is valid for all regions of space where the phase from different sheets are uncorrelated. For direct-drive configurations, this assumption holds everywhere apart from the caustic region of the pump sheet, where fields add coherently. Thus, the coherent sum of fields in the caustic region is larger than the incoherent sum, so without correcting for this, CBET scattering through a pump beam in its caustic region will be underestimated.

The ratio of the coherent and incoherent sums of incident (E_{inc}) and reflected (E_{refl}) fields of the pump sheet in its caustic region is called the *coherent caustic multiplier*,

$$M_{\text{CP}} = \frac{|E_{\text{inc}}|e^{i\phi_{\text{inc}}} + |E_{\text{refl}}|e^{i\phi_{\text{refl}}}}{|E_{\text{inc}}|^2 + |E_{\text{refl}}|^2}. \quad (1.30)$$

By making the same assumption as used to obtain Eq. 1.18, that $|E_{\text{inc}}| \sim |E_{\text{refl}}|$, this simplifies to,

$$M_{\text{CP}} = 1 + \sin(\phi_{\text{refl}} - \phi_{\text{inc}}), \quad (1.31)$$

which should be applied in the caustic region, (defined in Eq. 1.19), as the region where $|\varphi_1 - \varphi_2| \leq \lambda_0/2$. As stated in the discussion in Sec. 1.4.2, grid cells are typically larger than the size of the caustic region, $\mathcal{O}(\lambda_0)$, and SOLAS does not include linear interpolation of field quantities. Therefore, Eq. 1.31 cannot robustly be evaluated at the relevant scales. The caustic region is identified by a geometric algorithm, similar to the *caustic plane* method discussed in Sec. 1.5.2 and the ‘average’ value of the coherent caustic multiplier is used,

$$M_{\text{CP}} = 1 + 2/\pi, \quad (1.32)$$

when a ray undergoes CBET with a pump sheet in its caustic region. This coherent caustic correction increases the CBET scattering and is an important addition to make sure that ray-based CBET models are energy conserving.

The geometric approach that was developed to estimate when a ray is in the caustic region of another beam, ($|\varphi_1 - \varphi_2| \leq \lambda_0/2$), is described here. Similar to the *caustic plane* method from Sec. 1.5.2, this algorithm works by finding planes that divide cells and thus effectively increase their resolution, improving the accuracy of the nearest neighbour interpolation. The key assumptions of the method are that the boundary of the caustic region can be treated locally in grid cells as a plane and that the caustic region is approximately where ray amplitudes are greater than the FL capped amplitude, $A_{\text{ray}} > A_{\text{FL}}$. Fig. 1.15.c plots the trajectory of incident sheet rays from Fig. 1.15.a, with the locations of capped and uncapped rays plotted as small transparent red and blue dots respectively. The average value of each of these locations is represented by the larger blue ($\langle \mathbf{x}_{\text{cap}} \rangle$) and red squares ($\langle \mathbf{x}_{\text{uncap}} \rangle$) respectively, which are stored (only where present), in each SOLAS grid cell. The region of the cell occupied by these capped (blue) ray locations is assumed to be equivalent to the caustic region. The validity of the assumption was tested by conducting high resolution simulations of the 2-D reflected beam field reconstruction test in Sec. 1.4.3 to accurately reconstruct the phase and amplitudes of incident and reflected sheets on a high resolution mesh. It was found that the assumption is adequate, although it typically slightly overestimates the width

of the caustic region by $\mathcal{O}(10\%)$. This is not considered to be a significant issue, because energy conservation iterations are employed which minimise errors by varying M_{CP} over multiple iterations. Therefore, errors in the initial iteration are compensated by this minimisation.

To geometrically estimate the caustic region in cells which contain both capped (blue) and uncapped (red) ray locations, a *caustic region plane* is defined to separate these regions, defined by a point, \mathbf{x}_{CR} , and normal, $\hat{\mathbf{n}}_{\text{CR}}$,

$$\begin{aligned}\mathbf{x}_{\text{CR}} &= \frac{\langle \mathbf{x}_{\text{cap}} \rangle + \langle \mathbf{x}_{\text{uncap}} \rangle}{2}, \\ \hat{\mathbf{n}}_{\text{CR}} &= \frac{\langle \mathbf{x}_{\text{cap}} \rangle - \langle \mathbf{x}_{\text{uncap}} \rangle}{|\langle \mathbf{x}_{\text{cap}} \rangle - \langle \mathbf{x}_{\text{uncap}} \rangle|},\end{aligned}\quad (1.33)$$

where $\hat{\mathbf{n}}_{\text{CR}}$ is defined such that it points toward the caustic region. For a probe ray propagating through a mesh which contains a pump field, the ray is inside the caustic region if $\hat{\mathbf{n}}_{\text{CR}} \cdot (\mathbf{x}_{\text{probe}} - \mathbf{x}_{\text{CR}}) > 0$, under which circumstances, the pump-probe CBET gain is multiplied by the average value of M_{CP} defined in 1.32. This is illustrated in Fig. 1.15.c by the purple dashed lines. If a cell contains both a *caustic region plane* and a *caustic plane* (from Sec. 1.5.2), then the ray must be inside the caustic and on the lit side of the caustic to undergo CBET with M_{CP} applied. Fig. 1.15.d plots the caustic region, as obtained by the algorithm, as a transparent blue shaded area.

1.5.4 Dynamic Memory for Storing Fields and CBET Gains

CBET gains must be calculated between every pair of sheets that cross at a given location. For N_b beams, each with 2 possible sheets, discretised on a grid with N_x cells in each dimension, a total of $N_f \sim 2N_x^3 N_b$ *field data points* must be stored. Each of these data points must store the field magnitude, phase, wavevector and information used to evaluate CGT and the coherent caustic correction where necessary, as described in Sec. 1.5.2 and 1.5.3 respectively. This amounts to large computational memory requirements to store the fields. Additionally, SOLAS stores the CBET gains between each laser sheet to improve the code execution time. A separate gain exists between each sheet and therefore the memory cost to store this information scales as $N_g \sim 2N_f^3 N_b^2$.

N_g is a single number and N_f represents all field information, so for simulations with small numbers of beams, N_f is the dominant memory cost, whereas for large number of overlapping beams such as direct-drive simulations, N_g dominates. It is therefore important to use a memory efficient method to store this data so that large scale, 3-D simulations can be completed. SOLAS utilises pointers in each grid cell to dynamically allocate the field data, such that only where a sheet is present is its corresponding field magnitude, phase *etc.* stored. Additionally, gains between sheets are an attribute of the field data and are stored as single-precision floats, rather than the native SOLAS double precision, which also reduces memory costs for large simulations. These measures significantly reduce memory overhead for multi-dimensional CBET simulations, however high resolution 3-D simulations are still extremely memory intensive, which is an issue also experienced by IFRIT, the other 3-D CBET code

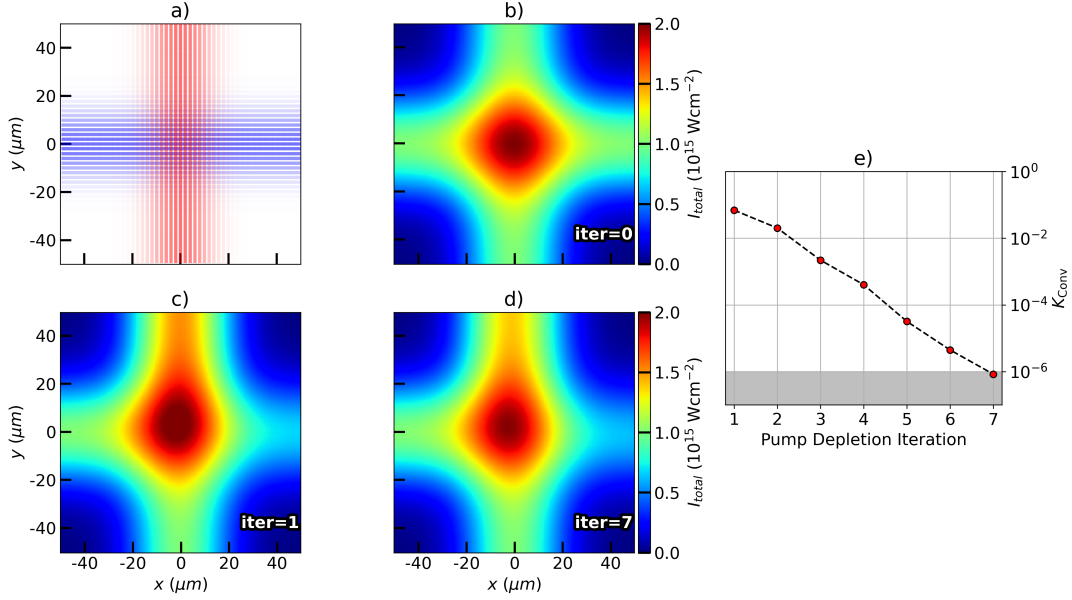


Figure 1.16: Results of successive pump depletion iterations for an illustrative simulation of two beams crossing and undergoing a CBET resonance in a uniform plasma background. Each beams' rays from the field reconstruction ray-trace are plotted in a), where more opaque rays indicate a higher power. Panel b) plots the reconstructed intensity from this ray-trace, where $i = 0$ indicates the field reconstruction ray-trace and therefore no CBET occurs. Panels c) and d) plot the intensity reconstructed from the 1st and 7th pump depletion iterations respectively, where the effect of transfer of powers between beams due to CBET is evident. Panel e) plots the convergence parameter from the simulation over successive pump depletion iterations, with convergence defined here as $K_{\text{Conv},0} = 10^{-6}$.

coupled to hydrodynamics.

1.5.5 Pump Depletion Iterations

The field reconstruction ray-trace (the initial ray-trace performed in the absence of CBET) returns the field from each sheet $|E_j^{i=0}|(\mathbf{x}, \mathbf{k}, \omega, \phi)$, where j is the sheet index and $i = 0$ indicates the field reconstruction ray-trace. This field is discretised on the SOLAS mesh using nearest neighbour interpolation, so that a ray passing through a cell updates the field in that cell. Rays can then be re-traced through this mesh and undergo changes in power due to CBET interactions with the fields from other sheets. The solution obtained from a single ray-trace with CBET is not the true solution however, because the field that the rays see throughout the CBET ray-trace is not dynamically updated by the change in ray power due to CBET as they propagate. This necessitates iteratively solving the ray-trace to account for CBET in *pump depletion iterations*, whereby for iteration i , the rays from sheet j propagate through the mesh and undergo CBET through $|E_{\text{sheet} \neq j}^{i-1}|$, while building up a new field, $|\tilde{E}_j^i|$. The new *build-up* fields, $|\tilde{E}_j^i|$, are introduced for the next iteration. This loop is repeated until convergence of the field has been achieved. Convergence is tested each iteration ($i > 0$) against the total power of rays $\tilde{P}_{j,n}^i$, from each sheet j travelling through each cell, explicitly defined by

the convergence parameter,

$$K_{\text{Conv}}^i = \max_{\substack{j \in \text{sheets} \\ n \in \text{cells}}} \left| \left(\tilde{P}_{j,n}^i / \tilde{P}_{j,n}^{i-1} \right) - 1 \right| < K_{\text{Conv},0}, \quad (1.34)$$

where $K_{\text{Conv},0}$ is a user defined parameter, typically set to 10^{-5} unless stated otherwise.

This procedure is illustrated in Fig. 1.16 for a simple, illustrative problem of two beams crossing in a uniform, stationary plasma background with a frequency difference between the beams tuned to give a CBET resonance. The effect of Inv-Brem deposition has been neglected in this simulation. Fig. 1.16.a shows the ray trajectories for the two crossing beams and Fig. 1.16.b plots the intensity from the field reconstruction iteration, without CBET. The intensities after one and seven pump depletion iterations are plotted in Fig. 1.16.c and Fig. 1.16.d respectively, which show that a single re-trace through the no-CBET fields does not return the converged solution. Fig. 1.16.e plots the convergence parameter after each iteration, illustrating that seven iterations were required to obtain the converged solution, plotted in Fig. 1.16.d.

For many beam simulations with complicated beam trajectories and many overlapping crossings such as direct-drive calculations, the problem is asymptotically unstable. This means that for iteration i , allowing rays to undergo CBET in the full $|\tilde{E}_{\text{sheet} \neq j}^{i-1}|$ causes unbounded gains on ray powers leading to divergent results for $|\tilde{E}_j^i|$. Numerical damping is therefore applied for these calculations to stabilise the solution. The actual fields that a ray will see for the subsequent iteration, $i + 1$, are composed of the weighted sum of the two *build-up* fields,

$$|E_j^i| = f_{\text{damp}} |\tilde{E}_j^i| + (1 - f_{\text{damp}}) |\tilde{E}_j^{i-1}|, \quad (1.35)$$

where f_{damp} is a user-defined damping value, which is by default set to a (relatively conservative) value of 0.75, to ensure that the solver does not diverge for complex problems.

1.5.6 Energy Conservation Iterations

The converged field solution from the pump depletion iterations returns the steady-state field and deposition profiles, accounting for CBET, given a field reconstruction algorithm, interpolation scheme *etc*. If there are errors in, for example, the field reconstruction algorithm, then the pump depletion iterations will return a steady-state solution, however this is not guaranteed to be accurate, *i.e.* the same as the result from a higher fidelity solver. The main cause of errors in field reconstruction is the treatment of laser caustics, as demonstrated for example in Fig. 1.13. This figure demonstrates that the SOLAS field reconstruction algorithm obtains essentially perfect agreement with LPSE everywhere apart from in the vicinity of the caustic. It can therefore be assumed that any errors in the CBET profiles, returned from the pump depletion iterations, occur due to errors in the field reconstruction and CBET scattering in the caustic region. The energy conservation error, ΔE , is a good proxy for the accuracy of the fields obtained from CBET, as in the absence of laser caustics, energy is conserved in

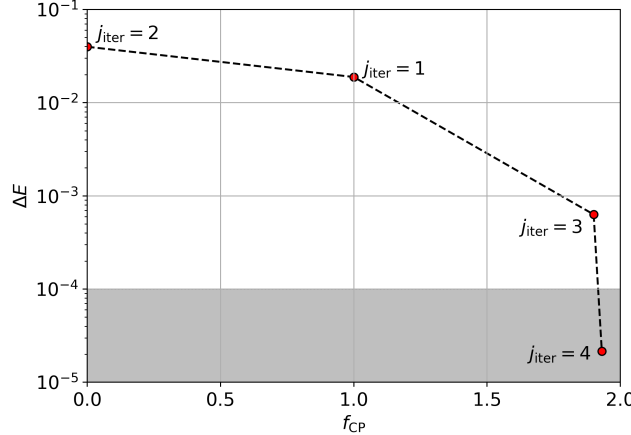


Figure 1.17: Energy conservation iterations for a two-beam caustic test problem, which is presented in Sec. 1.5.7.2. 4 iterations were required to achieve energy conservation, which was defined to be $\delta E < 1 \times 10^{-4}$. The order of the iterations is indicated by the text next to each point.

ray-based algorithms [34]. This is defined as,

$$\Delta E = \frac{P_{\text{dep}} + P_{\text{out}} - P_{\text{inc}}}{P_{\text{inc}}}, \quad (1.36)$$

where P_{dep} , P_{out} and P_{inc} are the power deposited by Inv-Brem, the ray-power leaving the domain and the incident power respectively. If this value is not small, it suggests that caustics are not accurately treated in the CBET scattering.

As in the BEAMCROSSER code, the assumption in SOLAS is made that minimising ΔE by altering the CBET gains in the caustic region will bring the result into better agreement with the true solution [34]. M_{CP} is modified to include a new *caustic pump multiplier*, f_{CP} , which is applied to probe ray CBET gains, when they are in the caustic region of the pump sheet,

$$\tilde{M}_{\text{CP}} = \begin{cases} 1 + f_{\text{CP}} \left(\frac{2}{\pi} \right), & \text{if in caustic region} \\ 1, & \text{otherwise} \end{cases} \quad (1.37)$$

where the same, geometric identification for the pump sheet caustic region is used as in Sec. 1.5.3. $f_{\text{CP}} = 1$ initially and is varied between $f_{\text{CP}} \in [-\pi/2, 2]$ over several *energy conservation* iterations¹⁴ to minimise ΔE . The lower bound on f_{CP} is to prevent ‘negative scattering’ in the caustic region, where the sign of the gain flips. The upper bound was selected by experimentation to prevent excessively large gains which result in the exponential power gain of rays blowing up to infinity.

An implementation of the Secant method is used to estimate the next value of f_{CP} . The first and second energy conservation iterations in a simulation use $f_{\text{CP}} = 1$ and 0, to obtain a gradient with which to estimate values of the multiplier. The Secant method was chosen for its simplicity and the fact that bracketing values of the root are not required. An example of

¹⁴Each energy conservation iteration contains a new set of pump depletion iterations, as is shown in Fig. 1.14.

the minimisation results are shown in Fig. 1.17. These results are from a two-beam caustic test problem, presented in Sec. 1.5.7.2, but the specifics of the problem are not important for the discussion here, simply that CBET in the presence of a caustic occurs. Therefore, a caustic region exists inside which f_{CP} will lead to modified gains which reduce energy conservation errors. The curve of $\Delta E(f_{\text{CP}})$ is simple and monotonic, which is observed for all simulations conducted with SOLAS, regardless of the complexity of the laser and target configuration. This means a more complex algorithm than the Secant method is not required for minimisation. When the CBET model runs in-line with the hydrodynamics, the value of f_{CP} from the last timestep that CBET was calculated is used, which means that energy conservation iterations are often not necessary. This is shown explicitly in Fig. 1.23.c, which shows the results of a 1-D CHIMERA-SOLAS simulation of OMEGA shot 89224. The bottom panel in the figure shows that energy conservation is frequently achieved by simply re-using the value of f_{CP} from the previous timestep.

To summarise, the total CBET gain that a probe ray (i) experiences in a pump sheet (j) is,

$$\tilde{\gamma}_{ij} = \gamma_{ij} M_{\text{PS}} \tilde{M}_{\text{CP}}, \quad (1.38)$$

where γ_{ij} is the value defined in Sec. 1.5.1 (depending on if using the kinetic or fluid gain model), the modified coherent caustic multiplier \tilde{M}_{CP} is defined in Eq. 1.37 and the polarisation smoothing multiplier, M_{PS} , defined in Eq. 1.27, is applied if the beams are assumed to be randomly rather than parallel-polarised.

1.5.7 CBET Validation

This section presents results from several CBET test problems where the results from SOLAS are compared to the wave based solver LPSE. Because LPSE is a wave-solver coupled to a linearised fluid response, the fluid CBET gain was used for all simulations in this section. Beams in the simulations all had a vacuum wavelength, $\lambda_0 = 0.351$ nm and a super-Gaussian spot profile, which was defined in Eq. 1.1. For consistency with LPSE, the Doppler shift of laser frequency was not calculated in these simulations so its effect on CBET is neglected, *i.e.* the right-hand side of Eq. 1.5 was forced to be zero. The plasma backgrounds for all initialisations were fully-ionised CH with $Z = 3.1$ and $T_i = T_e/2$. All tests are presented in Ref. [34] and the LPSE data is available from the repository in Ref. [64].

1.5.7.1 2-D CBET Without Caustics

Table 1.1: The ratio of the power of the seed beam as it exits the domain to its initial power.

	$P_{\text{seed,out}}^{\text{LPSE}} / P_{\text{seed,in}}^{\text{LPSE}}$	$P_{\text{seed,out}}^{\text{BEAMCROSSER}} / P_{\text{seed,in}}^{\text{BEAMCROSSER}}$	$P_{\text{seed,out}}^{\text{SOLAS}} / P_{\text{seed,in}}^{\text{SOLAS}}$
CBET + Absorption	1.315	1.325	1.320
CBET only	1.551	1.561	1.558
Absorption only	0.856	0.856	0.852

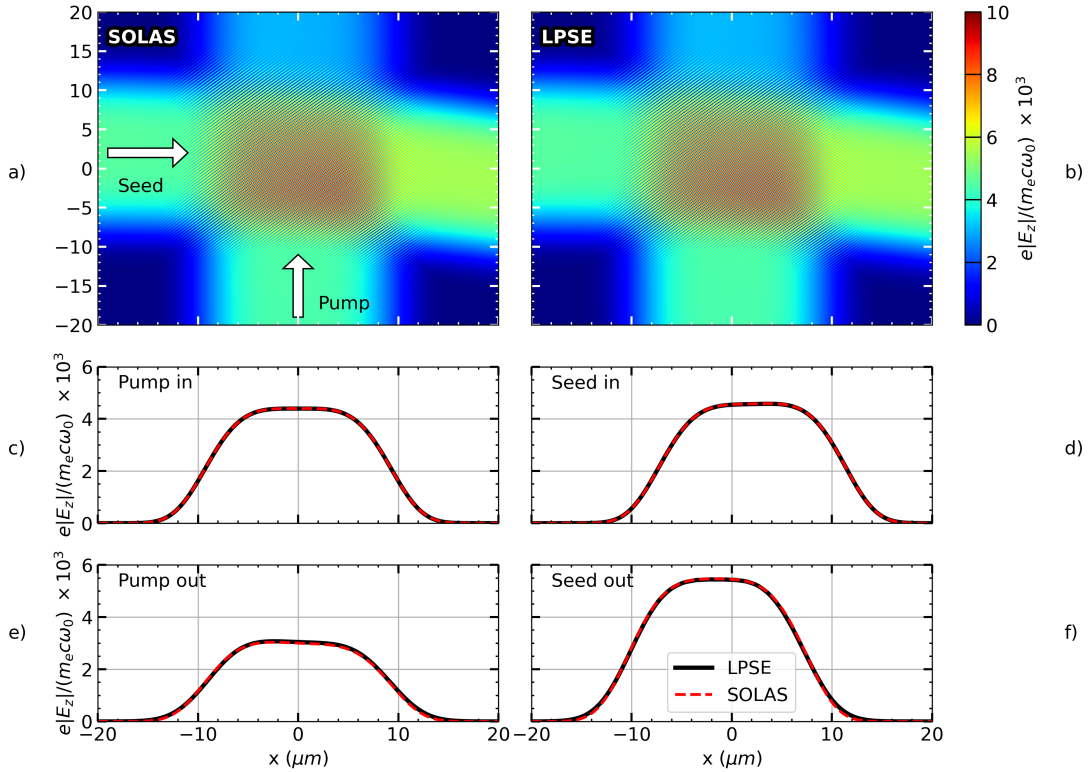


Figure 1.18: Results of the 2-D CBET test in the absence of laser caustics. Panels a) and b) show the electric field from the SOLAS and LPSE simulations respectively, after the pump depletion iterations have occurred. Panels c) and d) plot lineouts from the inbound fields of the pump and seed beams respectively for both SOLAS and LPSE. e) and f) plot the same for the outbound fields.

The first test problem is for the case of two beams crossing in a non-uniform, non-stationary plasma in the absence of laser caustics. The grid used for the problem was $x, y \in [-21, 22] \mu m$ and 2160 cells were used in each direction. This led to a resolution of $\Delta x \sim \lambda_0/20$ such that the beat field between the two beams could be resolved. The electron temperature was uniform, $T_e = 1$ keV. The density and fluid velocity profiles were,

$$n_e(y) = n_{cr}(0.006y_{\mu m} + 0.25), \quad (1.39)$$

$$\mathbf{u}(y) = -\hat{\mathbf{y}}(1.4 - 0.008y_{\mu m})c_s, \quad (1.40)$$

where $y_{\mu m}$ is the coordinate in microns. The beams both had widths $\sigma = 8.41 \mu m$ and peak intensities $I_0 = 2 \times 10^{18} W/m^2$. The beams were defined as *pump* and *seed* and launched from $\mathbf{x} = [-21, 2] \mu m$ and $\mathbf{x} = [0, -21] \mu m$ along the $+\hat{\mathbf{x}}$ and $+\hat{\mathbf{y}}$ directions respectively. The beam and plasma configuration were chosen to create a strong CBET resonance where the beams cross one another.

Fig. 1.18.a and Fig. 1.18.b show the electric field obtained from the SOLAS and LPSE simulations respectively. It can be seen that the density gradient in $\hat{\mathbf{y}}$ causes the seed beam to refract somewhat and that CBET results in a significant energy transfer from the pump to the

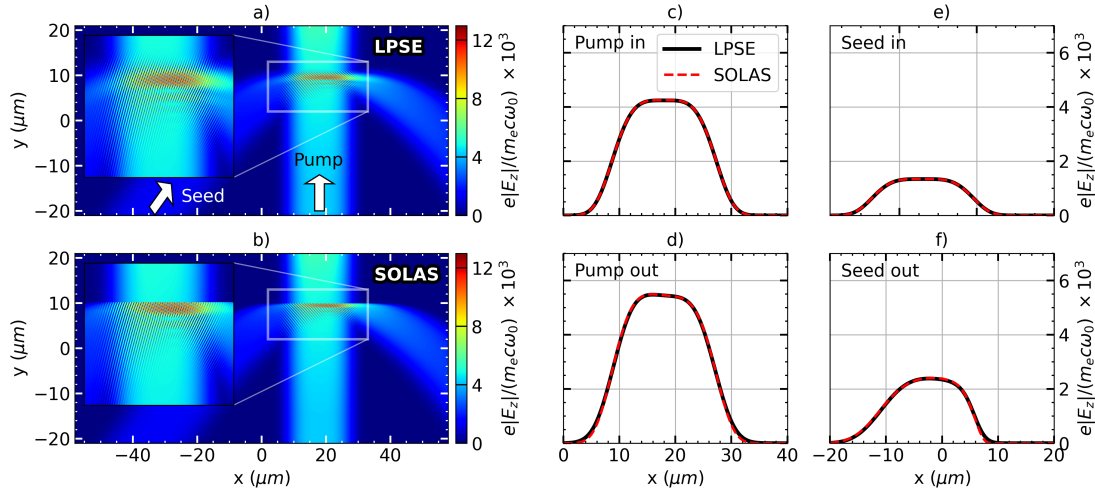


Figure 1.19: Results of the 2-D CBET test in the presence of a laser caustic. Panels a) and b) show the electric field from the LPSE and SOLAS simulations respectively. Also plotted is an inset zoom on the caustic region of the seed beam, which demonstrates that SOLAS does not capture the evanescent field. Panels c) and e) plot lineouts from the inbound fields of the pump and seed beams respectively for both SOLAS and LPSE. d) and f) plot the same for the outbound fields.

seed beam. The lineouts in Fig. 1.18.c, Fig. 1.18.d, Fig. 1.18.e and Fig. 1.18.f all show excellent agreement between SOLAS and LPSE. This is further demonstrated in Tab. 1.1, which lists the ratio of the outgoing seed beam power to the incident power for LPSE, SOLAS and the BEAM-CROSSER post-processor, the results from which are also presented in Ref. [34]. The energy conservation error after the pump depletion iterations was small, $\Delta E \sim 10^{-6}$, as expected because the CBET interaction does not involve any caustics.

1.5.7.2 2-D CBET With Caustics

Another two-beam problem was implemented to test CBET in the presence of a caustic. For this simulation, the grid was $x, y \in [-21, 21] \mu m$ and $x, y \in [-60, 60] \mu m$ with a minimum resolution of $\Delta x = \Delta y \sim \lambda_0/20$. A uniform electron temperature was used, $T_e = 2 \text{ keV}$. The pump beam travelled straight up a linear density gradient and therefore did not refract, whereas the seed beam reflected in the gradient and travels out. The beam geometry was chosen so that the pump beam crossed through the middle of the seed beam caustic and the density and flow profiles were tuned to create a resonance at this crossing location,

$$n_e(y) = \begin{cases} 0.02y_{\mu m} + 0.3, & x \geq -15 \mu m, \\ 0, & x < -15 \mu m, \end{cases} \quad (1.41)$$

$$\mathbf{u} = -1.14c_s \hat{\mathbf{y}}. \quad (1.42)$$

Both beams again had widths $\sigma = 8.41 \mu m$. The pump and seed beams were launched from $\mathbf{x} = [18, -21] \mu m$ and $\mathbf{x} = [-35, -21] \mu m$ and pointed along $\hat{\mathbf{k}} = [0, 1]$ and $\hat{\mathbf{k}} = [0.707, 0.707]$ respectively. The peak intensities were $I_0 = 2 \times 10^{18} \text{ W/m}^2$ and $I_0 = 2 \times 10^{17} \text{ W/m}^2$ for the

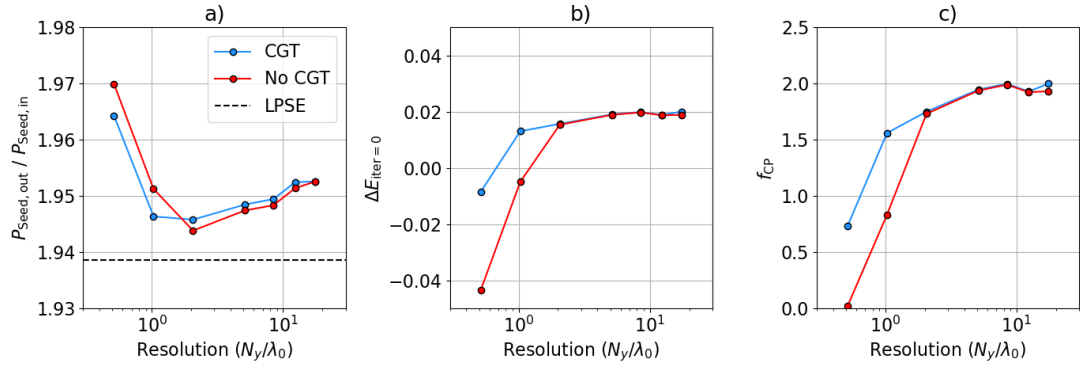


Figure 1.20: Results from a resolution scan of the two-beam caustic CBET test both with CGT and without. Plotted in a), b) and c) are the power amplification of the seed beam, initial energy conservation error before energy conservation iterations and caustic pump multiplier used to obtain energy conservation respectively.

pump and seed respectively.

Fig. 1.19.a and Fig. 1.19.b plot the LPSE and SOLAS¹⁵ total fields respectively. The inset zooms demonstrate that the evanescent fields are not captured in the GO framework. Fig. 1.19.c, Fig. 1.19.d, Fig. 1.19.e and Fig. 1.19.f plot the lineouts of the LPSE and SOLAS field solutions at their exit from the grid, which all demonstrate excellent agreement. The LPSE seed beam amplification was $P_{\text{seed,out}}/P_{\text{seed,in}} = 1.94$ [34]. This test was run both with and without the CGT model described in Sec. 1.5.2 and at a variety of resolutions, to demonstrate how energy conservation at caustics are partially a resolution problem and how CGT mitigates for this somewhat.

Fig. 1.20 plots the results of the resolution scans both with and without CGT. The seed beam amplification after energy conservation iterations is plotted in Fig. 1.20.a, which demonstrates that even at lower resolutions, SOLAS is manages to reproduce the LPSE result to an accuracy of $\mathcal{O}(1\%)$. The energy conservation error from the first energy conservation iteration (*i.e.* after the first set of pump depletion iterations, but before energy conservation was achieved), is plotted in Fig. 1.20.b. This plot shows convergence in the physics at higher resolutions, although the converged solution (without enforced energy conservation) indicates small errors in the handling of the caustics, which energy conservation is able to correct in an *ad-hoc* manner. Fig. 1.20.c plots the caustic pump multiplier that was required to achieve energy conservation. Both Fig. 1.20.b and Fig. 1.20.c show that CGT improves the convergence of the SOLAS solution when the caustic region width $\sim \lambda_0$ is not properly resolved by the mesh.

1.5.7.3 16 Beam CBET in 2-D

The final CBET test problem presented as validation is a planar, azimuthally symmetric CBET test with 16 beams in a direct-drive like plasma at the OMEGA scale [34]. This problem involves many beams, all of which undergo laser caustics and CBET scattering with multiple

¹⁵The field from SOLAS simulation with the minimum resolution, $\Delta x \sim \lambda_0/20$ is plotted in Fig. 1.19.b.

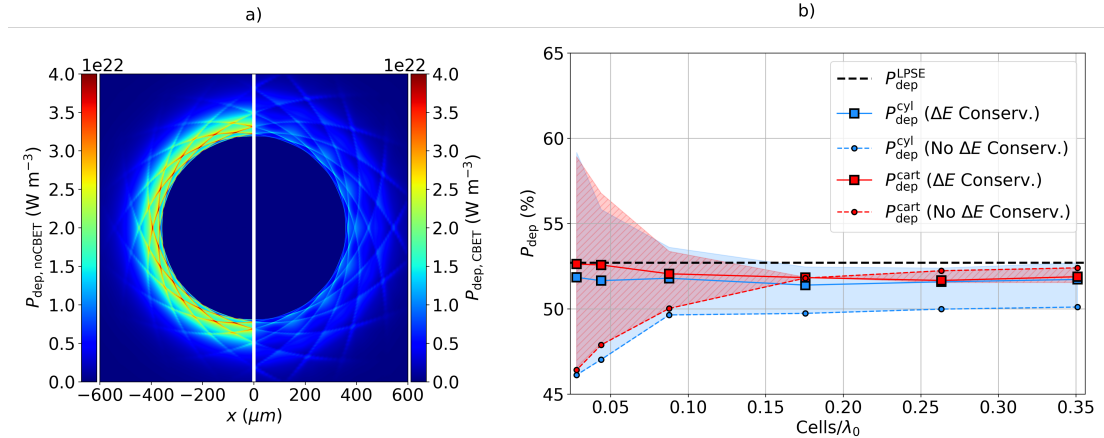


Figure 1.21: Results from the 16 beam CBET test problem. Panel a) plots the deposited power both without (left) and with (right) CBET from the simulation ran in cylindrical coordinates at $1 \mu\text{m}$ radial resolution. Panel b) plots the results of the resolution scan for both Cartesian and cylindrical coordinates. The circles and squares are the values of power deposition without and with enforced energy conservation respectively. The shaded regions illustrate the magnitude of energy conservation error from the initial energy conservation iteration, which can be thought of as the (single-sided) error on the circular points.

other laser sheets. It is also well suited to test the implementation of the SOLAS CBET model in non-Cartesian geometries, unlike the previous problems which did not have an angle of symmetry. The same setup can be easily initialised in both Cartesian and cylindrical geometry to cross-compare the results.

All beams were pointed toward the origin with an initial starting radius of 1 mm, equally spaced around the circle with a width $\sigma = 386.8 \mu\text{m}$. The peak intensity of each beam was $I_0 = 0.68 \times 10^{18} \text{ W m}^{-2}$ and each had an incident power $P_{\text{inc}} = 76.3 \text{ TW}$. The electron temperature was set to $T_e = 2 \text{ keV}$ and the ion temperature $T_i = T_e/2$. The electron density used the profile from Eq. 1.20, with the scale factor, $S = 1$. A radial velocity profile was used, which was obtained from a fit to a 1-D LILAC simulation,

$$\mathbf{u}(r) = c_s \left[M_0 + M_1 \log\left(\frac{r - x_0}{x_1}\right) \right], \quad (1.43)$$

where $M_0 = 1.41$, $M_1 = 1.37$, $x_0 = 204 \mu\text{m}$ and $x_1 = 343 \mu\text{m}$. The Cartesian simulations had a bounding domain $x, y \in [-800, 800] \mu\text{m}$, with a resolution ranging from $\Delta_{x,y} = 1 \rightarrow 12.5 \mu\text{m}$. The cylindrical simulations had domain $r \in [0, 800] \mu\text{m}$ and $\phi \in [-\pi, \pi]$, with radial resolutions $\Delta_r = 1 \rightarrow 12.5 \mu\text{m}$ and a fixed ϕ resolution of $\Delta_\phi = 0.025$. These simulations are compared to an LPSE simulation of the same problem below.

In the absence of CBET, LPSE calculated 90.5 % power deposition. All SOLAS simulations agree with this result to within $\mathcal{O}(0.1 \%)$. Including CBET, LPSE obtained an absorption of 52.7 %. Deposited power from the $\Delta_r = 1 \mu\text{m}$ simulation is plotted in Fig. 1.21.a, both without CBET, and with CBET after energy conservation was achieved. Power deposition from the Cartesian simulation at $\Delta_x = 1 \mu\text{m}$ is not plotted, but looks almost identical, apart from the

small grid artefacts. The reduction in magnitude of deposition is clearly visible, along with a slight radial broadening of the deposition region. The angled-line features in both plots are from the caustic region of the beam, where a 16-fold symmetry can be seen in both of the results, due to the beam geometry of the problem. The finer scale thin structures in both of these plots is due to enhanced deposition occurring at the beam caustic, where the ray amplitude swells to a maximum, enhancing the field strength.

Plotted in Fig. 1.21.b are the values of deposited power in the presence of CBET for both the cylindrical and Cartesian simulations, compared to the LPSE result. Circular markers are the values obtained for CBET deposition after the first set of pump-depletion iterations, *i.e.* before energy conservation was achieved. The larger square markers are the results after energy conservation was achieved. Shaded regions correspond to the magnitude and sign of the energy conservation error, $\Delta E_{j=0}$, *before* energy conservation was achieved, *i.e.*, for the circular points. This region corresponds to the deposition that could be achieved if any, arbitrary approach was taken to enforce conservation, for example if the value $\Delta E_{j=0} = \pm 10\%$ for one simulation, then up to 10 % could be added to (subtracted from) P_{dep} . The trend, especially at lower resolution demonstrates that enforcing energy conservation brings the SOLAS result closer to LPSE, motivating the use of the approach in later chapters of this thesis. Although the cylindrical results typically appear to have a larger value for $\Delta E_{j=0}$ compared to the Cartesian results, the post conservation results are all deemed sufficiently close to both the Cartesian result and LPSE. The saturation of error for cylindrical geometry at higher radial resolutions seem to indicate that $\Delta E_{j=0}$ is dominated by the ϕ resolution in this region, which was kept fixed across all simulations.

1.6 Simulations of CBET for OMEGA Direct-Drive Implosions

This Section presents CHIMERA-SOLAS simulations of OMEGA direct-drive implosions. In Sec. 1.6.1, 1-D Rad-Hydro simulations of OMEGA shot 89224 coupled to a 3-D ray-trace from SOLAS will be presented, both with and without the effect of CBET. This illustrates that the implementation of the CBET model in SOLAS correctly captures the loss of drive efficiency. In Sec. 1.6.1, 3-D SOLAS post-processes of spherically symmetric hydrodynamic data from the LILAC code are presented both with and without CBET. It is compared to results from the 3-D CBET codes IFRIIT and BEAMCROSSER. These simulations demonstrate that the SOLAS CBET model also correctly captures the enhancement of beam-mode drive asymmetry introduced by CBET in spherical illumination geometries.

1.6.1 1-D hydrodynamics, 3-D Ray-Trace Simulation of OMEGA Shot 89224

A 1-D CHIMERA-SOLAS Rad-Hydro simulation of OMEGA 89224 was performed to illustrate the effect that CBET has on drive efficiency of direct-drive implosions. Drive efficiency is lost primarily due a reduction in the magnitude of deposited energy. A secondary effect is that the radii where deposition occurs is pushed slightly further away from the ablation surface. This happens because beams only lose energy inside the CBET resonance volume, which

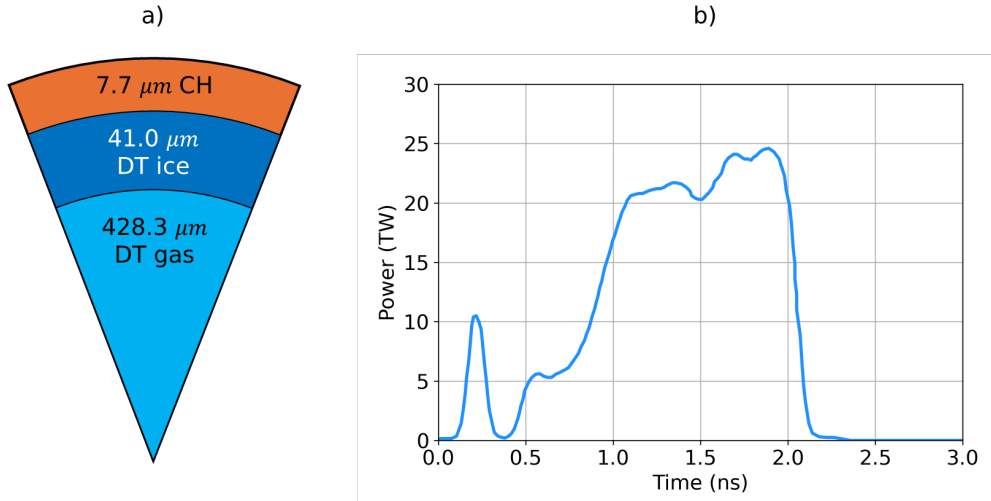


Figure 1.22: The initial conditions for OMEGA shot 89224. The shot was a cryogenic, DT implosion with materials and radii shown in panel a). Panel b) plots the incident laser pulse shape.

Table 1.2: Integrated metrics from simulations of OMEGA 89224. LILAC metrics are from Refs. [1–3].

	Yield ($\times 10^{14}$)	$\langle T_i \rangle$ (keV)	t_{bang} (ns)	V_{imp} (km/s)
LILAC, CBET	4.00	4.8	2.17	476
CHIMERA, CBET	1.78	4.2	2.16	490
CHIMERA, no CBET	6.77	6.2	1.94	661

for backscatter CBET occurs at the Mach-1 surface, as explained in Sec. ???. Therefore, the deposited power vs. radius curve is shifted to slightly higher radii. Both of these effects are captured by a 3-D CBET model coupled to 1-D Rad-Hydro.

The initial conditions for shot 89224 are plotted in Fig. 1.22.a, with vacuum outside the outer radius. The incident laser pulse is also plotted in Fig. 1.22.b, which has a total incident energy of 28.7 kJ. An experimental yield of 1.17×10^{14} neutrons was observed for this shot. A tabulated Sesame table of state was used for each material [76] and a $P_{1/3}$ radiation transport algorithm was used with tabulated opacities and emissivities from the SPK code [77]. Thermal conduction was solved with using a fully implicit algorithm for flux-limited Spitzer conductivities [78]. The electron flux limiter was set by using the default CHIMERA direct-drive method,

$$f_{\lim,e} = \begin{cases} 0.06, & \text{if in picket pulse} \\ 0.15, & \text{otherwise.} \end{cases} \quad (1.44)$$

The simulation domain was $r \in [0, 1680]$ μm , with a fixed radial resolution $\Delta_r = 1$ μm . Two simulations were conducted, one with the effect of CBET on power deposition and one without. In order to load balance the ray-trace and discretise CBET interactions between different beams around the spherical 4π sr, SOLAS used a sparse angular grid with $N_\phi = 51$ and

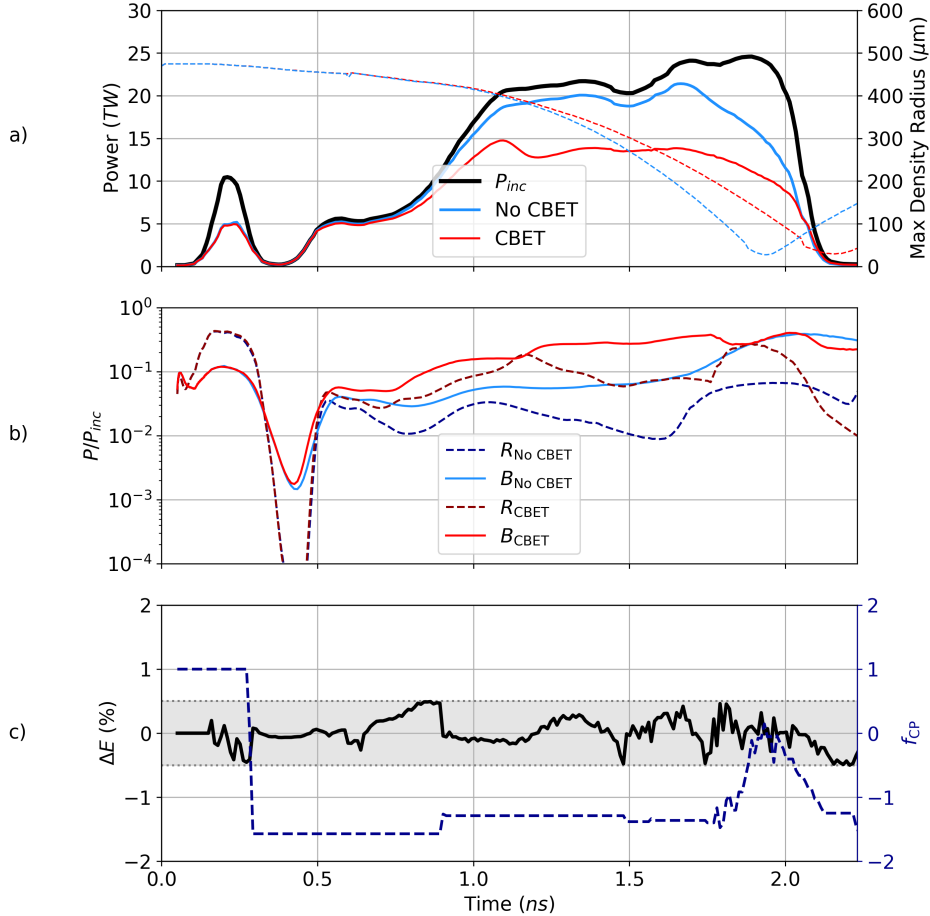


Figure 1.23: CHIMERA-SOLAS simulation of OMEGA shot 89224. Panel a) shows the deposited power both from 2 separate simulations of 89224, one with and one without CBET as red and blue solid curves respectively. The shell radius, defined at the radius of maximum density, is also plotted on the right axis as dashed curves. Panel b) plots the time resolved partition of non-absorbed light for these simulations. Plotted in c) is the energy conservation error after energy conservation was achieved, alongside the value of f_{CP} that was used to achieve conservation.

$N_\theta = 30$ azimuthal and polar cells respectively. At times earlier than 10 ps, a *cold start* routine was employed, where 50 % of the incident power was deposited at the critical radius to create a finite scale length of underdense plasma, which rays could deposit and refract in. Ray-traces were conducted every hydrodynamic timestep, without computing CBET up to 150 ps¹⁶ after which a full ray-trace routine, including the effect of CBET was conducted every 10 ps. For hydrodynamic steps in between these CBET ray-traces, the most recently computed P_{dep} profile (normalised to 1 and then scaled to the incident power), was used as the laser source term for the timestep. Parameter scans of the ray-trace frequency confirmed that the behaviour of OMEGA simulations is well converged with this frequency.

The spatially integrated absorbed power is plotted in Fig. 1.23.a as solid curves. 62.8 % and

¹⁶Note that the low intensity from this section of the pulse means that the CBET gains are negligible.

83.9 % of the incident energy was absorbed for the CBET and no-CBET simulations respectively. Also plotted as dashed curves are the shell trajectories from the two simulations. It can be seen that the reduction in drive efficiency leads to a significantly slower implosion with a delayed bangtime. Tab. 1.2 gives temporally and spatially integrated implosion metrics from the CHIMERA-SOLAS simulations, along with a comparison to a post-shot LILAC simulation which includes a 1-D model for CBET. Including CBET in the CHIMERA-SOLAS simulation gives significantly better agreement across all metrics, which is primarily due to correctly capturing the reduction in absorption. The most interesting metrics to compare across the codes when looking at the effect of CBET in 1-D are the implosion velocity and bangtime, which are in excellent agreement with LILAC. This is because these metrics are primarily functions of the absorbed laser energy, whereas the yield and burn averaged temperature additionally depend strongly on shock timing and compression [79, 80]. Shock timing between codes is particularly sensitive to differences in the thermal conduction modelling, equation of states, grid resolution and preheat modelling, all of which are likely to have been different between the LILAC and CHIMERA simulations. The strong agreement between the CHIMERA CBET simulation and the LILAC results for the bangtime and implosion velocity metrics provide evidence that direct-drive implosions can be accurately modelled without using artificial multipliers to the laser power.

Fig. 1.23.b plots the partition of the non-absorbed power for both simulations. This is divided between *blowby* light (B), which is light that left the computational domain travelling quasi parallel to the beam normal and *reflected* light, which leaves the domain travelling quasi antiparallel. Note that the plot is on a log axis. Examining first the blue curves which are from the no-CBET simulation, it can be seen that initially during the main pulse, from $t \sim 1.0 \rightarrow 1.6$ ns, the reflected light fraction decreases while the blowby goes up. This is because the critical radius converges, so the wings of the laser beam are less efficiently absorbed. The reflected light fraction increases sharply at $t \sim 1.6$ ns and $t \sim 1.8$ ns for the no-CBET and CBET simulations respectively. This corresponds to the time when the critical density crosses from the CH ablator material to DT fuel. DT has a significantly lower ionisation state compared to the ablator and therefore the electron-ion collision frequency decreases, corresponding to a drop in the Inv-Brem absorption and therefore an increase in the reflected light fraction. Both simulations show that blowby light is the most significant loss of coupling both with and without CBET, especially late in the implosion as the capsule converges.

Plotted in Fig. 1.23.c are the laser energy conservation, ΔE , and the modification to the caustic pump multiplier f_{CP} that was found to achieve energy conservation. The grey bounds indicate the accepted criteria to satisfy energy conservation, which was 0.5 % of the incident power. The plot of f_{CP} illustrates that the value remained constant over many timesteps and therefore only a single set of pump depletion iterations was required for the majority of timesteps. This is not true late in the implosion, when the critical radius converges and CBET is responsible for ~ 40 % reductions in deposited power. At these times, caustic CBET interactions are important and therefore ΔE is sensitive to the value of f_{CP} . As shown in Sec. 1.5.7.3 however, the iterations are believed to improve the fidelity of the modelling which

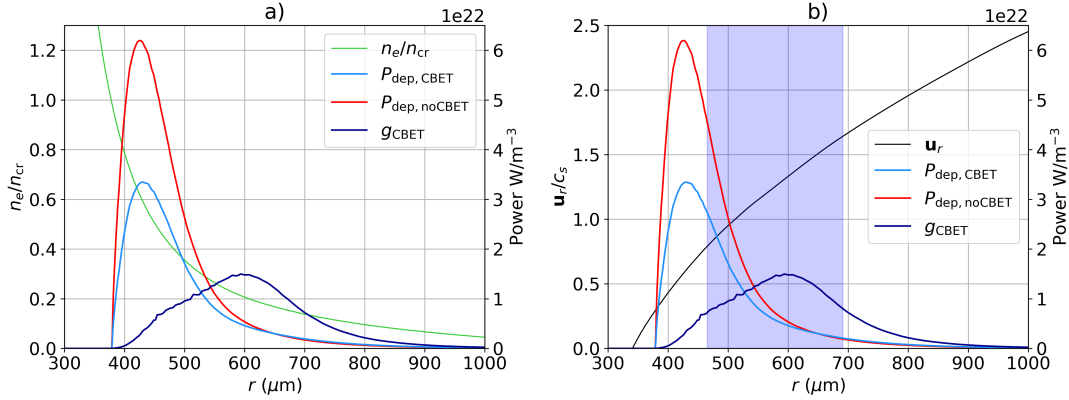


Figure 1.24: CBET deposition diagnostics from $t = 1.6$ ns into the CHIMERA-SOLAS simulation of OMEGA 89224, with CBET. Both sub-plots plot the power deposition with and without CBET, along with the g_{CBET} , which is defined as the sum of the absolute value of all power lost or gained by rays via CBET in the cell. The electron density normalised to critical density and radial velocity normalised to the sound speed are also plotted in panel a) and b) respectively. The blue shaded region in b) represents the full-width half-maximum of the g_{CBET} curve.

is validated here by strong agreement with tuned, post-shot LILAC simulations.

Plotted in Fig. 1.24.a are the instantaneous power deposition profiles from the CHIMERA-SOLAS simulation with CBET at $t = 1.6$ ns, alongside the n_e profile in the under-dense region. Note that the no-CBET profile plotted here is not from the no-CBET simulation of OMEGA 89224, but the power deposition from the field reconstruction ray-trace of the CBET simulation, *i.e.*, the deposition through the same hydrodynamic profiles, but without the effect of CBET on the power deposition. At this time, SOLAS estimates that CBET reduces the deposition versus by about 40 % compared to the no-CBET deposition. No rays go beyond n_{cr} and therefore all deposition occurs outside of the critical radius. Also plotted in dark blue is the CBET scattering, g_{CBET} , defined as the sum of the absolute value of all power lost or gained by rays due to CBET in a SOLAS cell,

$$g_{\text{CBET}}(\mathbf{x}) = \sum_i^{\text{rays}} |\Delta P_{i,\text{CBET}}(\mathbf{x})|, \quad (1.45)$$

where \mathbf{x} represents the position of the power gain/ loss, discretised within cells on the SOLAS grid. The deposition is broadly reduced only inside the peak of the scattering curve, because backscatter CBET transfers energy from inbound light to outbound light in direct-drive. Deposition is marginally increased outside the peak of the scattering curve, because the reflected and blowby light has been amplified due to CBET.

These power profiles are also plotted alongside the coronal radial velocity profile, normalised to the sound speed. The full-width half-maximum of the scattering curve is shown as the shaded blue region. Resonance occurs close to the Mach-1 surface as expected, which is where the plasma flow shifts the frequencies of radially inbound and outbound light such that they can excite an IAW. The peak scattering also is shifted slightly further out, because

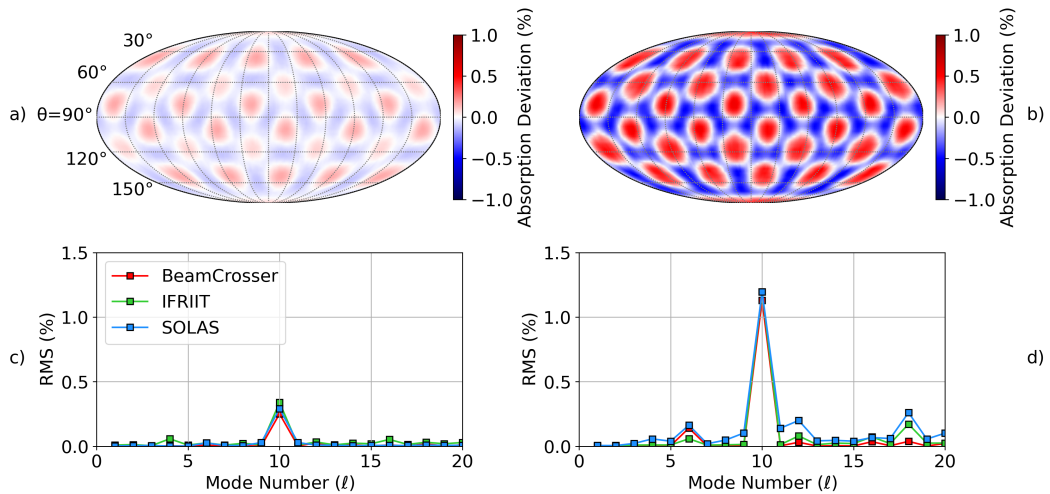


Figure 1.25: 3-D SOLAS post-process of spherically symmetric hydrodynamic data obtained from a LILAC simulation of an OMEGA direct-drive implosion. Figures a) and b) show the deviation in radially integrated deposited power without and with CBET respectively. Figures c) and d) plot the spherical harmonic modal decomposition for these maps alongside results from the IFRIIT and BEAMCROSSER codes without and with CBET respectively.

the outbound light mostly does not travel radially outward. Assuming the fluid CBET gain formulation and neglecting the $(\omega_j - \omega_i)$ in Eq. 1.24, it can be shown that non-radial light shifts the resonance to larger u_r and therefore greater radii.

1.6.2 3-D Post Process of Absorption Non-Uniformity

A final problem used to validate the CBET model from SOLAS was to compute the instantaneous 3-D effect of CBET on power deposition through spherically symmetric hydrodynamic data from a LILAC simulation of an OMEGA implosion. The same problem has been computed with both the IFRIIT and BEAMCROSSER codes allowing cross-code validation of the 3-D deposition asymmetry. The LILAC profiles were taken from Ref. [20], and the IFRIIT and BEAMCROSSER results are presented in Ref. [73]. CBET is known to enhance the beam-mode asymmetry which arises from the number and geometry of laser beams used to illuminate the target [32]. Correctly capturing this enhancement of asymmetry relies on a field reconstruction algorithm with good treatment of laser caustics and sufficient ray statistics in every cell across the computational grid to reconstruct the field everywhere that CBET is important.

This problem is a particularly stringent test of the grid discretisation for field reconstruction. The use of an underlying spherical polar grid for the SOLAS semi-structured mesh leads to cells that vary in volume from pole to pole. Some differences in the reconstructed field are therefore inevitable between the capsule waist and pole purely from this grid discretisation. If this difference was insufficiently small, the power deposition with CBET would contain a conspicuous mode-2 which, for simulations integrated with the hydrodynamics, would lead

to undesirable stagnation asymmetries, purely seeded from the computational mesh.

The simulation had a radial domain $r \in [350, 1362] \mu\text{m}$ with underlying grid resolution $\Delta_r = 1 \mu\text{m}$ ¹⁷. The full 4π sr was simulated, where an underlying polar mesh was used for the SOLAS grid with $N_\phi = 160$ and $N_\theta = 82$, which was then combined to give approximately equal area cells as described in Sec. 1.3.2. Fig. 1.25.a and Fig. 1.25.b show the deviation in radially integrated power deposition from the mean value for the no-CBET and CBET simulations respectively. The mode-10 pattern is clearly visible in both plots, although the magnitude is greatly increased by CBET, as expected. No clear mode-2 from the capsule pole to waist is seen which indicates that the SOLAS mesh is sufficiently close to equal-area to not result in significant grid artefacts.

A function, f discretised over azimuthal (ϕ) and polar (θ) angles can be decomposed into spherical harmonics,

$$f(\phi, \theta) = \sum_{\ell=0}^{\ell_{\max}} \sum_{m=-\ell}^{m=\ell} a_{\ell m} Y_\ell^m(\phi, \theta), \quad (1.46)$$

where $Y_{\ell m}$ are the spherical harmonic basis vectors and $a_{\ell m}$ are the associated coefficients [73]. The modal asymmetry of a given mode number, ℓ , is then defined as,

$$\sigma_\ell = \sqrt{\frac{1}{4\pi} \sum_{m=-\ell}^{m=\ell} a_{\ell m} a_{\ell m}^*}, \quad (1.47)$$

where the $a_{\ell m}^*$ is the conjugate of $a_{\ell m}$. Fig. 1.25.c plots the modal decomposition of the no-CBET radially integrated power deposition deviation from the mean, *i.e.* σ_ℓ up to mode $\ell = 20$. Excellent agreement is observed between SOLAS and the other codes. The dominant mode is $\ell = 10$, as is expected due to the beam port geometry.

Fig. 1.25.d plots the same, but now for the power deposition including CBET. As is also seen in the skymaps, the asymmetry is significantly amplified by CBET. Good agreement is again observed between SOLAS, IFRIIT and BEAMCROSSER across the spectrum. CBET appears to induce small amplitude modes other than just the $\ell = 10$ such as $\ell = 6$, $\ell = 12$ and $\ell = 18$. These are all multiples of 6, and therefore are likely induced by some OMEGA beam ports having 6 nearest neighbours [81, 82]. Small differences are observed between all codes, which is expected due to the different solvers and grids employed by each. SOLAS appears to slightly overestimate the modes 9 and 11, which have negligible values for both IFRIIT and BEAMCROSSER. This is potentially due to the ray shape function smearing routine used, that was described in Sec. 1.3.4, which smear power from a ray in one cell into neighbours. This could bleed some $\ell = 10$ into neighbouring modes. In future, a more robust spherical harmonic smoothing could be introduced to address this issue, although the effect is not likely to be significant for integrated simulations due to the small amplitude.

The incident and reflected sheet fields¹⁸ for a single beam both with and without CBET are plotted in Fig. 1.26. The incident fields without and with CBET are plotted in Fig. 1.26.a and

¹⁷Note that the adaptive radial resolution of the SOLAS mesh had a maximum radial resolution $\Delta_{r,\max} = 10 \mu\text{m}$.

¹⁸Note that incident and reflected here refer to which sheet the ray belongs to, *i.e.* if it is before or after the caustic location.

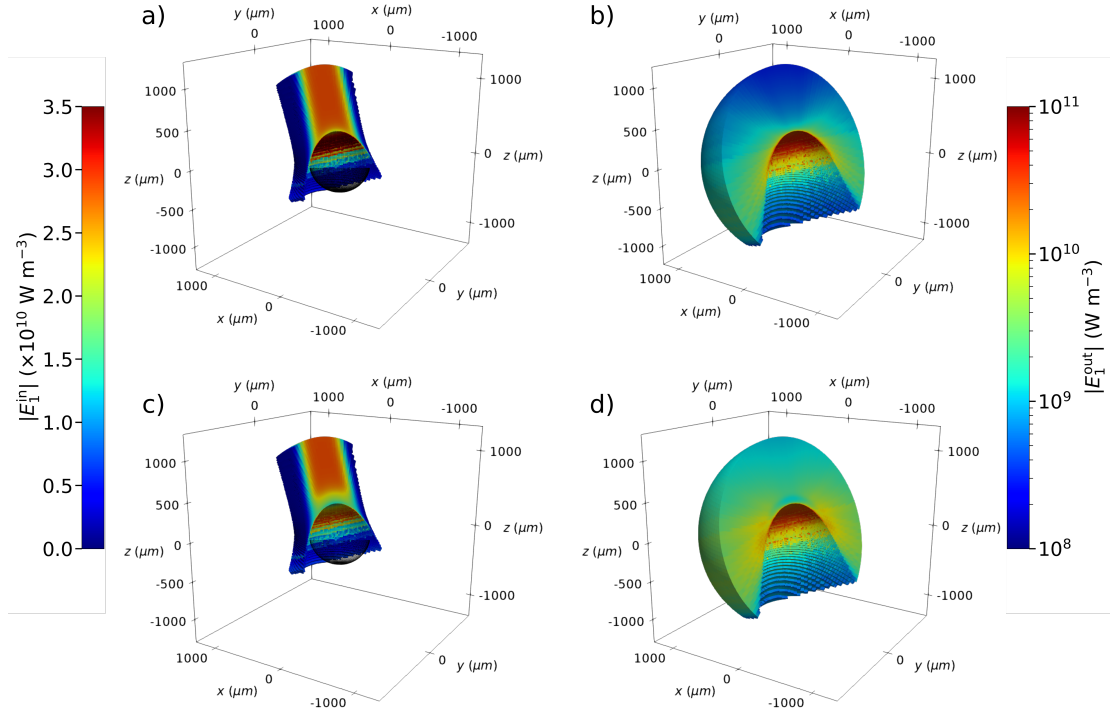


Figure 1.26: Electric fields from the 3-D post-process. Panels a), b), c) and d) plot the incident sheet without CBET, the reflected sheet without CBET, the incident sheet with CBET and the reflected sheet with CBET respectively. The critical surface is plotted with the inbound sheets as a transparent spherical wireframe. Note that the outbound sheets are plotted on a log scale.

Fig. 1.26.c respectively, and share the left colourbar. The inbound CBET sheet field shows a clear depletion of the field strength near the critical surface compared to the no-CBET field, which is the result of energy transfer from radially inward propagating light to outward travelling light via backscatter. This leads to the reduction in absorbed energy. Fig. 1.26.b and Fig. 1.26.d plot the reflected fields without and with CBET respectively, and share the right colourbar. The reflected sheet travels mostly radially outward and therefore has been significantly amplified by the CBET backscatter mechanism compared to the no-CBET case. In the absence of CBET, the field strength of the reflected sheet is significantly lower than the incident sheet field strengths for two reasons. Firstly, peak absorption occurs at the maximum radial penetration depth of the light into plasma, which is typically close to where rays experience their caustic and change sheet. Additionally, the rays diverge after reflecting from the critical surface leading to a reduction in ray amplitude and therefore field strength.

1.7 Conclusions

This chapter presented the implementation and validation of a 3-D ray-trace and CBET model, SOLAS, for the 3-D Rad-Hydro code CHIMERA. Prior to this work, a simple 1-D ray-trace was used to model the laser for direct-drive implosions which was strongly detrimental to the ability of the code to accurately model these experiments. Radially tracing rays

inward, even for 1-D Rad-Hydro simulations, misses the important interplay between the convergence of the target and loss of deposition. The lack of a CBET model, which is responsible for significant energy coupling loss at OMEGA laser facility energy scale implosions, also meant that deposited power had to be reduced in an *ad-hoc* manner to obtain agreement with experiments. These factors severely limited the predictive capability of the code to model these experiments.

Sec. 1.3 described the implementation of the 3-D ray-trace in the SOLAS laser package. An adaptive solver is used to trace rays through a semi-structured Eulerian mesh in Cartesian, cylindrical or spherical geometries. Validation of this implementation was also presented. The 3-D laser ray-trace enables CHIMERA to model direct-drive implosions and other laser-driven HEDP experiments. It is also a crucial prerequisite to a ray-based CBET model.

Issues with ray-based CBET models often stem from a poorly reconstructed laser electric field profile. The approach taken in SOLAS to obtain the electric field was described in Sec. 1.4, which is to trace a set of neighbouring rays around each ray and then relate the area of the ray to the field strength. Validation problems were conducted for this section which illustrated that this approach yields excellent agreement with the wave-based solver LPSE. Caustics are also identified and the field near them is capped to a diffraction limited value. Validation problems showed that the field solver was robust and suitable for use within the CBET model.

The implementation of the SOLAS CBET model was described in Sec. 1.5. This model employs the linear kinetic or fluid gain formulations and the reconstructed field to estimate power changes of rays due to CBET. Fixed point iteration is then used to find the equilibrium solution and additional energy conservation iterations can be used to account for small errors in the caustic field reconstruction. Validation problems against LPSE and the ray-based BEAMCROSSER post-processor demonstrated that SOLAS correctly computes CBET for direct-drive conditions in Cartesian and cylindrical geometries.

A 1-D, spherical Rad-Hydro, CHIMERA-SOLAS simulation of the OMEGA shot 89224 was presented in Sec. 1.6.1, alongside a comparison to a LILAC simulation. The CBET model behaved as expected, significantly reducing the power deposition and slowing the implosion. Excellent agreement was obtained between CHIMERA-SOLAS and LILAC for integrated parameters which primarily depend on the amount of energy coupled to the target. Sec. 1.6.2 presented a 3-D post-process of spherically symmetric hydrodynamic data from a LILAC simulation. The power deposition asymmetry was compared to the IFRIIT and BEAMCROSSER codes and good agreement was found with those models. CBET was shown to significantly enhance the deposition asymmetries as expected. The results from this section showed that the SOLAS CBET model functions as expected in spherical geometry and therefore CHIMERA-SOLAS is capable of performing 3-D spherical direct-drive implosions with CBET which could previously only be conducted with the ASTER-IFRIIT code combination.

2 Cylindrical Simulations to Study the Effect of Beam Radius in Direct-Drive

This chapter describes a cylindrical, direct-drive implosion simulation platform and its use to study the effect of the beam radius initial condition on OMEGA laser facility experiments. Although results from the cylindrical simulations do not have the same convergence properties of spherical implosions, the essential physics for studying the effect of beam radius is preserved. The main benefit of the geometry is that a 2-D ray-trace can be used to model the lasers, which yields several orders of magnitude speed-up, compared to spherical 3-D implosions. The reduction in computational expense enables an ensemble of CBET simulations to be performed, which would be exceedingly expensive for 3-D spherical calculations. Beam radius strongly effects CBET and therefore including a model for the interaction in computational studies is crucial [4].

The chapter begins with a review of existing literature concerning the beam radius initial condition for direct-drive implosions, with an emphasis on the use of this parameter in statistical modelling of OMEGA campaigns. A description of the cylindrical simulations is then provided, which includes a discussion of its advantages, weaknesses and applicability to current OMEGA experiments. A tuning procedure which was followed to obtain hydrodynamically similar implosions at different beam radii is then described. The main results of the chapter are then presented, which include calculations of the power deposition asymmetry both with and without CBET and an explanation of why CBET typically amplifies the asymmetry. CBET is also shown to introduce *modal-flips* of the deposition, where the power deposition asymmetry inverts. Stagnation state asymmetries of the hydrodynamic profiles are then studied for all implosions and these demonstrate that while increasing beam radius in the absence of CBET reduces beam-mode asymmetries, the opposite behaviour is observed in the presence of CBET, although the exact relationship is complex. The chapter concludes with a summary of the work and suggestions of further work that could be undertaken using the same cylindrical platform.

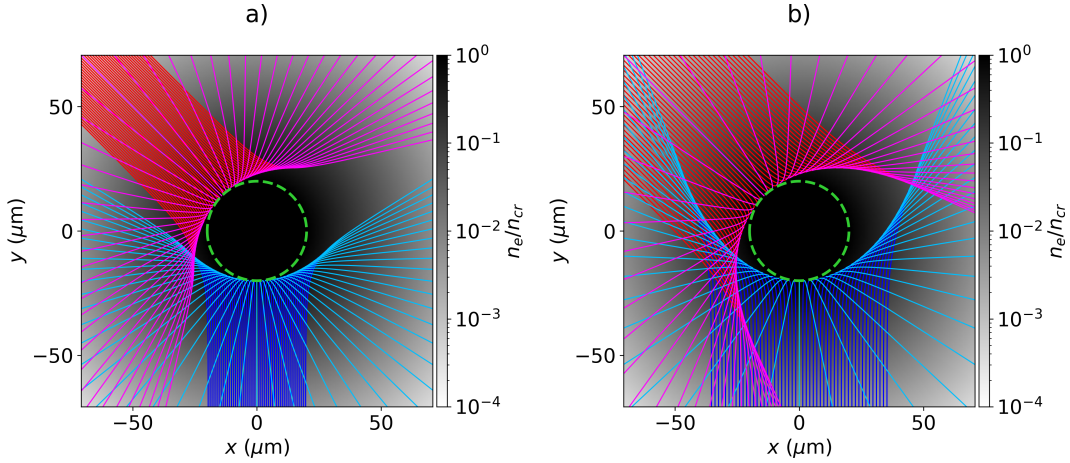


Figure 2.1: The trajectory of rays from two beams through a direct-drive like coronal plasma.

The density profile for both simulations is $n_e = n_{cr} \exp [-(r_{\mu m} - 20)/100]$. Panels a) and b) plot rays from beams with widths $\sigma = 10$ and $18 \mu m$ respectively. Ray trajectories are separated for each beam by colour depending on their sheet. Rays coloured in red and dark blue are from the incident sheet (before the ray caustic) and rays coloured in magenta and light blue are from the reflected sheet (after the ray caustic).

2.1 Introduction to Beam Radius in Direct-Drive Inertial Confinement Fusion

An idealised direct drive implosion (neglecting the effect of random or otherwise, shot-to-shot variations), has a limited number of initial conditions which define the implosion. The target can be described by a set of materials and their thicknesses. Initial target parameters are intimately coupled to the physics of the implosion and, in part, dictate the propagation time of shocks through the target, hydrodynamic stability and absorption of the laser energy. The pulse shape defines the laser power which is incident of the target as a function of time. It can be designed to, for example, drive shocks by introducing sharp rises in the incident power with time, which leads to large changes of ablation pressure [83]. A given facility also has a number of beam ports, each of which has a specific origin and pointing location, which influence the magnitude of the *beam-mode* asymmetry, arising from the uniformity of laser absorption. The intensity profile of each laser and specifically the beam radius is an additional parameter which can be varied and plays an important role in defining both the power which can be coupled to the target and the magnitude of beam-mode asymmetry.

As shall be explored in this chapter, increasing the beam radius alters the magnitude of energy lost via CBET, leading to a reduction in the maximum target mass that can be imploded at a given speed [4]. The beam radius relative to the target is therefore often effectively varied from shot to shot, by changing the outer radius (and therefore mass) of the target, while fixing the width of the beam. This defines a dimensional variable, which is the radius of the beam divided by the target radius, R_b/R_t . Typically, at the OMEGA laser facility, this is explic-

itly defined as the radius of the beam which contains 95 % of the incident power divided by the initial outer target radius [4, 84, 85],

$$R_b/R_t = \frac{r_{95}}{R_t}, \quad (2.1)$$

where r_{95} is defined by the integral,

$$\int_0^{r_{95}} e^{-\left|\frac{r}{\sigma}\right|^{n_s}} dr = 0.95, \quad (2.2)$$

and the definition of a circular, super-Gaussian beam profile from Eq. 1.1 has been used. In the absence of CBET, it can intuitively be understood that increasing this parameter should improve the uniformity of the laser illumination, because beam spots overlap each other more on the target, and therefore reduce the beam-mode [5]. Larger R_b/R_t also lead to slightly less absorption in the absence of CBET, because a larger fraction of the incident light (especially at late time as the target converges) would reach lower density plasma and therefore not be absorbed. CBET significantly complicates this interpretation, however.

Fig. 2.1.a and Fig. 2.1.b plot results of ray-tracing calculations, in a direct-drive relevant, exponentially decaying density profile, with a smaller and larger beam respectively. In direct-drive, backscatter CBET is the dominant mechanism to depletes absorption, which occurs when outbound light gains energy from inbound light¹. The outward rays from the small beam radius simulation in Fig. 2.1.a do not overlap the incident light from the other beam and therefore limited CBET between these beams will occur. The trajectories from the larger radius simulation in Fig. 2.1.b, however do cross the inbound rays from the other beam, which could lead to a resonant CBET interaction, and significant reduction of the absorbed power. As was shown in Fig. 1.25, CBET substantially increases absorption asymmetry on the OMEGA laser facility. This means that in the presence of CBET, the effect of increasing R_b/R_t on illumination asymmetry is not clear. While in the absence of CBET, it should lead to greater beam overlap, this increased overlap will result in more CBET which could reduce uniformity of absorption.

Isolating the contribution of CBET in particular is important to enable extrapolation of experimental results to future facilities. It is hoped that next generation direct-drive facilities will have broad bandwidth lasers² which are expected to almost entirely eliminate CBET [86–88]. Studying how CBET specifically affects absorption and stagnation symmetry can not currently be done experimentally, as significant backscatter CBET occurs at all laser facilities which are capable of conducting compression experiments. Therefore, computational studies are well suited to investigate how R_b/R_t influences the role of CBET.

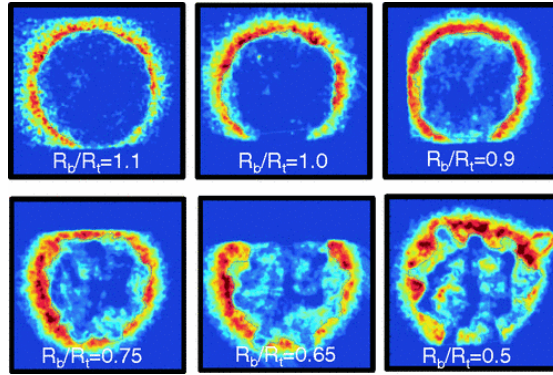


Figure 2.2: Soft x-rays emitted from the ablation surface of direct-drive implosions with various R_b/R_t values, as measured by an x-ray framing camera. All images were taken at a constant capsule radius of $R = 175 \mu\text{m}$. The figure has been reproduced with permission from Ref. [4].

2.1.1 Previous Work Studying the Effect of Beam Radius on OMEGA

Experimental and computational work has been conducted to explore the effect that the beam radius has on direct-drive implosions. Froula *et al.* conducted a series of implosions which systematically varied R_b/R_t to explore the balance between loss of coupling due to increasing CBET at large radii, and increased illumination non-uniformity at lower radii [4]. Soft x-ray emission data from a selection of implosions with different radii are plotted in Fig. 2.2, all of which are taken at the same target shell radius. These images show that at lower values of R_b/R_t , mid-mode perturbations³ become increasingly significant. The results of these experiments found that neutron yield was maximised at $R_b/R_t \sim 0.8$. 1-D modelling using the CBET model in LILAC was in good agreement with the experimental results, verifying that CBET was responsible for the decrease in coupled energy to the target [36].

During direct-drive implosions, the target implodes radially inward, therefore the critical radius decreases with time. At the OMEGA laser facility, beam radii are fixed for a single shot, and therefore it makes sense to parameterise the initial condition by the ratio of the beam radius to the initial target radius. A promising laser optics technique known as *zooming*, could significantly enhance performance by reducing the focal spot of the laser to track the critical radius as the target implodes [89]. The reduced beam radius late in the implosion reduces blowby light and leads to more deposition closer to the ablation surface which enhances the ablation pressure and overall performance. Simulations by Trickey *et al.* in Ref. [80] have demonstrated that, assuming full CBET mitigation, zooming can enhance ablation pressures by $\sim 50\%$ for ignition scale direct-drive experiments. If zooming is employed without full CBET mitigation, the fractional increases would be substantially larger, because CBET losses scale very strongly with R_b/r_{cr} , the ratio of beam radius to critical radius [84]. In other words, zooming is itself expected to act as a CBET mitigation tool. The

¹Note that outbound here, means light travelling quasi-parallel to the approximately radially outward fluid velocity, and inbound means quasi-anti-parallel.

²It is expected that $\Delta\omega/\omega_0 \sim 1\%$ will be sufficient to eliminate CBET in direct-drive for frequency-tripled lasers.

³In direct-drive, *mid-modes* are loosely defined as modes similar to $\ell = 10$.

simulation platform described in this section could prove to be a promising computational design tool to help to understand how to optimise zooming to mitigate CBET, without introducing overly detrimental beam-mode degradation.

2.1.2 Statistical Modelling of OMEGA Direct-Drive Implosions

In recent years, a lot of work has been carried out to develop a statistical modelling capability for direct-drive implosions on the OMEGA laser facility. This modelling serves several critical purposes, including enhancing the predictive capability of simulations [90], guiding experimental design to achieve higher performance implosions [91], identifying important sources of degradation on current facilities [5, 92] and validating simulation codes to help ensure they produce physically relevant results [93]. The first generation statistical model, described by Lees *et al.* in Ref. [90], uses a high dimensional fit, to create a mapping between experimental and 1-D simulation results in order to explain significant differences in their results. A next generation statistical model has recently been developed by Ejaz *et al.*, which uses auto-encoders to reduce the design-space dimensionality and subsequently transfer learning to calibrate simulation outputs to experimental data. The subsequent review shall however, focus on the more widely studied results of the first model.

In the model described by Lees *et al.* [90], 1-D simulation results are fed into the model and degraded by a series of power law multiplications, which returns a more physically accurate experimental yield. Each power law multiplication represents a physical process for yield degradation with respect to 1-D physics, not included in the simulation. Each of these is termed a *yield-over-clean* (YOC_i), where the i refers to each source of degradation. The neutron yield from the 1-D simulation ($Y_{1\text{-D}}^{\text{sim}}$) can thus be converted to a prediction of the experimental yield [90],

$$Y^{\text{exp}} = (\text{YOC}_h \text{YOC}_f \text{YOC}_{\ell=1} \text{YOC}_b \text{YOC}_{\text{res}}) Y_{1\text{-D}}^{\text{sim}}, \quad (2.3)$$

where YOC_h is a degradation term from hydrodynamics and instability growth, YOC_f is degradation due to radioactive decay of the Tritium fill, $\text{YOC}_{\ell=1}$ is degradation from $\ell = 1$ modes, YOC_b is degradation from a finite number and radius of beams and YOC_{res} is a residual size scaling which is required to reduce performance of hydrodynamically downscaled implosions [94]. Each of these terms and their functional forms shall be discussed briefly, in order to provide context for the utility of the model and highlight that understanding the relevant physical processes which lead to degradation can improve its performance.

Hydrodynamic Degradation 1-D simulations do not capture short wavelength perturbations which grow via the Rayleigh–Taylor Instability (RTI) and reduce the yield of experiments by puncturing and breaking up the shell as the capsule implodes inwards. Instabilities may be seeded by laser imprint [95–97], or small scale defects in the target materials [98, 99]. Degradation can be reduced either by altering implosion design to increase the shell adiabat which increases the ablative stabilisation of the RTI [100, 101], or by lowering the In-Flight Aspect Ratio (IFAR), which increases the distance that the instability must grow through to

puncture the shell [102]. The degradation term includes scaling with the target convergence ratio, $C_R \equiv R_0/R_{\text{stag}}$, and with the ratio of outer to inner shell radius, $\hat{D} \equiv R_{\text{out}}/R_{\text{in}}$, which is believed to compensate for inaccuracies in modelling the shock propagation speed through the target. The hydrodynamic degradation term thus has the functional form,

$$\text{YOC}_h = \left[\frac{(\alpha/3)^{1.1}}{\text{IFAR}/20} \right]^{\mu_1} C_R^{\mu_2} \hat{D}^{\mu_3}, \quad (2.4)$$

where μ_i are the fitting parameters, which are obtained from nonlinear regression across many OMEGA shots. The fitting procedure demonstrated that experimental yields are very significantly reduced by these hydrodynamic degradations, with the most unstable shots yielding values of $\text{YOC}_h \sim 0.1$ [5].

Fill Age Degradation OMEGA cryogenic implosions contain a DT fuel gas fill with a surrounding ice layer. The tritium in this fuel is unstable and undergoes radioactive decay to ${}^3\text{He}$. This occurs over a period of days to weeks, which typically elapse between the initial gas filling procedure to the shot day [103]. ${}^3\text{He}$ has a lower freezing temperature than DT and thus sublimates, accumulating in the fill region. The accumulation of Helium in the gas reduces the final yield, both by increasing radiative losses due to its higher ionisation, and by increasing density of the vapour, which reduces compressibility and thus stagnation pressure in the hot-spot. Both of these effects can be captured by conducting 1-D simulations with a ${}^3\text{He}$ concentration (and corresponding reduction of tritium density) which is a function of fill age. The yield over clean due to the fill age and radioactive decay can then be taken as the ratio of these 1-D simulation yields,

$$\text{YOC}_h = \left(\frac{Y_{1\text{-D},\text{He}}^{\text{sim}}}{Y_{1\text{-D}}^{\text{sim}}} \right)^{\mu_4}, \quad (2.5)$$

where $Y_{1\text{-D},\text{He}}^{\text{sim}}$ is the yield from the 1-D simulation with accumulated ${}^3\text{He}$ and μ_4 is a fitting parameter. Good agreement is observed with a fitted parameter value of $\mu_4 = 1.3$. The value is larger than 1 (and the 95 % confidence interval does not include 1), which suggests stronger degradation than observed in 1-D calculations. This could be due to radioactive decay damaging the shell, leading to increased hydrodynamic instability growth [5].

Mode 1 Degradation In direct-drive implosions on the OMEGA facility, $\ell = 1$ modes can be introduced to an implosion by a global offset of the capsule from the target chamber centre, mispointing of the laser beams or a power imbalance. These are random and uncontrollable and therefore the statistical models can only account for their effect after the shot has occurred. By conducting post-shot analysis of an implosion, the model returns an estimated yield which could have been achieved, if no $\ell = 1$ were present, $Y^{\text{exp}}/\text{YOC}_{\ell=1}$. Mode 1 asymmetries have a clear signature in the broadening of the neutron time-of-flight detector peaks, when observed from orthogonal lines of sight [75]. The width of the peaks from multiple lines of sight can be analysed to return an angularly resolved apparent ion temperature

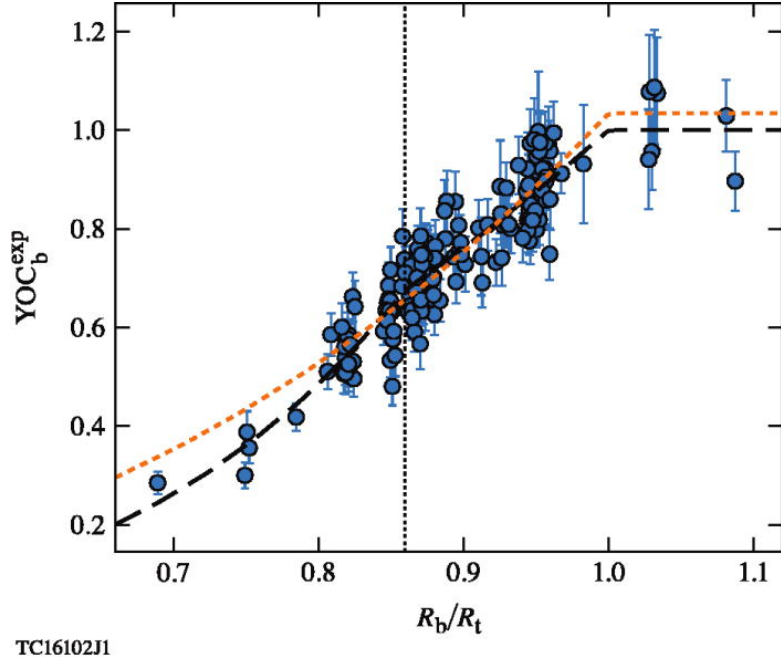


Figure 2.3: Experimentally inferred fusion yield degradation due to the finite beams on the OMEGA laser facility. The dotted orange curve is the fit obtained from just using the $\bar{R}_{b/t}$ relation, while the black dashed curve uses the full relation in Eq. 2.7. The vertical dotted line indicates the critical threshold, $\hat{R}_{b/t}^{\text{crit}} = 0.86$, after which the $\hat{R}_{b/t}$ also has an effect. The cross validation error from the $\bar{R}_{b/t}$ and full fit is -1.0% and -0.5% respectively. The figure has been reproduced with permission from Ref. [5].

map, the asymmetry of which is dominated by the lowest mode of the hot-spot [104]. Thus, it is deduced that the ratio of the maximum to minimum apparent ion temperatures from the experimental neutron time-of-flight signal can be used as a proxy for the amplitude of the mode 1, $R_T = T_{\max}/T_{\min}$. This leads to a yield over clean expression for the $\ell = 1$ degradation source,

$$\begin{aligned} \text{YOC}_{\ell=1} &= \hat{R}_T^{\mu_5}, \\ \hat{R}_t &\equiv \max\left(\frac{R_T}{R_T^{\min}}\right), \end{aligned} \quad (2.6)$$

where μ_5 is the fitting parameter and the minimum threshold value, R_T^{\min} is introduced due to imperfect reconstruction of the apparent ion temperature map and is fitted separately. Work has been conducted to minimise the effect of the $\ell = 1$ on OMEGA by repositioning the target after several initial shots to minimise the asymmetry in the apparent ion temperature measurement and thus increase performance [75].

Finite Beam Degradation The OMEGA laser facility has 60 beams arranged around a sphere, which generally gives good illumination uniformity on a hard sphere surface, less than the 1 % deviation which is believed to be necessary to achieve ignition [105, 106]. An $\ell = 10$ remains in the deposition however, as is demonstrated in Fig. 1.25, which is often referred to as the beam-mode. In the absence of CBET, increasing R_b/R_t increases the hard-sphere

illumination uniformity [92]. As already described however, increasing beam radius leads to more blowby light and therefore more CBET. This reduces the coupled energy and potentially introduces additional asymmetry to the implosion. Additionally, increasing the overlap of beams on the target could reduce the amplitude of the imprint seed and therefore increase performance. The uncertainty as to which physical mechanisms are important, is highlighted by the complexity of the degradation parameter compared to those already described,

$$\begin{aligned} \text{YOC}_b &= \left(\bar{R}_{b/t} \right)^{\mu_6} \left(\hat{R}_{b/t} \right)^{\mu_7}, \\ \bar{R}_{b/t} &= \begin{cases} R_b/R_t & \text{if } R_b < R_t, \\ 1 & \text{if } R_b \geq R_t, \end{cases} \\ \hat{R}_{b/t} &= \begin{cases} \frac{R_b}{R_t R_{b/t}^{\text{crit}}} & \text{if } R_b/R_t < R_{b/t}^{\text{crit}}, \\ 1 & \text{if } R_b/R_t \geq R_{b/t}^{\text{crit}}, \end{cases} \end{aligned} \quad (2.7)$$

where μ_6 & μ_7 are fitting parameters, the threshold behaviour in $\bar{R}_{b/t}$ was chosen to fit a small number of shots (< 10) at $R_b/R_t > 1$ and the threshold behaviour at $R_{b/t}^{\text{crit}}$ was introduced to fit a physically unexplained transition between two regimes in the data.

The fitted curve from the model is shown in Fig. 2.3, as the black dashed curve alongside the inferred values from experimental data points. Also plotted in orange is a fitted curve obtained from just using the simple $\bar{R}_{b/t}$ degradation. Introducing the $R_{b/t}^{\text{crit}}$ threshold significantly reduces the cross validation error of the fit. The switch between the two regimes is found from the fitting procedure to occur at $R_{b/t}^{\text{crit}} = 0.86$. This is close to value of minimum illumination asymmetry for beams incident on a hard hard-sphere ($R_b/R_t = 0.82$), which suggests that the degradation at the lowest values of R_b/R_t is dominated by beam-mode, however this has not been experimentally or computationally verified. Experiments between $R_{b/t}^{\text{crit}} < R_b/R_t < 1$ could be influenced by changing behaviour due to CBET or imprint, which is not properly captured by the 1-D LILAC simulations included in the model.

The hypothesis tested in this chapter is that the change in yield over clean at $R_b/R_t = R_{b/t}^{\text{crit}}$ is due to increasing CBET as beam radius increases, which increases beam-mode asymmetry and therefore suppresses the YOC_b term. Although LILAC does include a model for CBET, it is a 1-D code and therefore the 3-D beam-mode perturbations cannot be inferred from its results. Qualitatively, this hypothesis can explain the observed behaviour in Fig. 2.3, which demonstrates that at $R_{b/t}^{\text{crit}}$, the gradient of YOC_b decreases. This behaviour should occur if CBET acted to amplify the asymmetry of the stagnation state, causing the simulation to be less similar to the 1-D LILAC results, than if CBET did not significantly amplify asymmetries.

2.2 Cylindrical Simulation Platform for Beam Radius Parameter Scan

The method employed to study whether CBET induced beam-mode asymmetry at $R_b/R_t \gtrsim R_{b/t}^{\text{crit}}$ contributes to the second distinct regime from Eq. 2.7, was to conduct a series of cylin-

drical direct-drive simulations. These simulations are in a different convergence regime to spherical implosions, but retain much of the key physics relevant to the study, such as CBET, target convergence and beam-mode perturbations of the target. Crucially, it circumvents the large computational run-times of 3-D spherical simulations which include a CBET model. Inspiration for the cylindrical implosion platform was taken from the work of Follett *et al.* in Ref. [34], where a similar, 16-beam, planar configuration was used for a 2-D CBET test problem. The SOLAS result for this validation problem is presented in Sec. 1.5.7.3.

2.2.1 Advantages and Validity Considerations of the Cylindrical Simulation Platform

Ideally, fully 3-D Rad-Hydro simulations, coupled to a 3-D CBET model would be used for this work. This would retain the spherical convergence of the implosion and the 3-D nature of the beam-mode perturbation growth through stagnation, while also capturing how CBET influences these effects. These simulations are extremely expensive however and can take months to complete. A 2-D ray-trace (where rays can only move in two cardinal directions rather than 3) leads to large reductions in cost.

Ray-based CBET models require a ray from every laser sheet to pass through every computational grid cell where CBET scattering is significant. Therefore, by reducing the dimensionality of the problem, savings are made proportional to the reduction in number of cells, which is $\mathcal{O}(100)$ from 3-D spherical direct-drive calculations to the 2-D simulations presented in this chapter. Additionally, 10 beams were used to produce a mode-10, rather than the 60 on OMEGA, yielding another factor of 6 fewer rays. Each of the eight 2-D CBET simulation presented here took $\mathcal{O}(10^3)$ CPU hours, whereas (assuming the above logic), $\mathcal{O}(10^6)$ CPU hours would be required for each equivalent 3-D spherical simulation. On 1000 processors, each 3-D simulation would therefore take over a month to finish, as opposed to these simulations which all ran to completion within a day on 128 cores. Note that the above scaling assumes that the laser ray-trace and CBET computation costs dominate the simulation run-time, which is found to be the case for all CHIMERA-SOLAS simulations.

The physics of the implosion is however different in cylindrical as opposed to spherical geometry. Firstly, the mass converges in only 2 directions rather than 3 as the target implodes, which results in increased convergence at stagnation, potentially altering the beam-mode asymmetry growth. The 2-D cylindrical perturbations will also only evolve in the simulation plane, unlike the true 3-D case where they interact with material ‘above’ and ‘below’ them as well. This could lead to the cylindrical simulations overpredicting the beam-mode degradation compared to 3-D spherical simulations. In the corona, the expanding plasma also diverges in only 2 directions rather than 3 as it rockets away from the capsule, which leads to reduced density gradients in the corona, where the laser propagates and deposits energy. This could have the effect of shifting the deposition to greater radii above the critical surface, reducing the drive efficiency.

Despite these differences, implosion simulations were produced which were, qualitatively, sufficiently hydrodynamically similar to spherical implosions to suggest that parallels can be

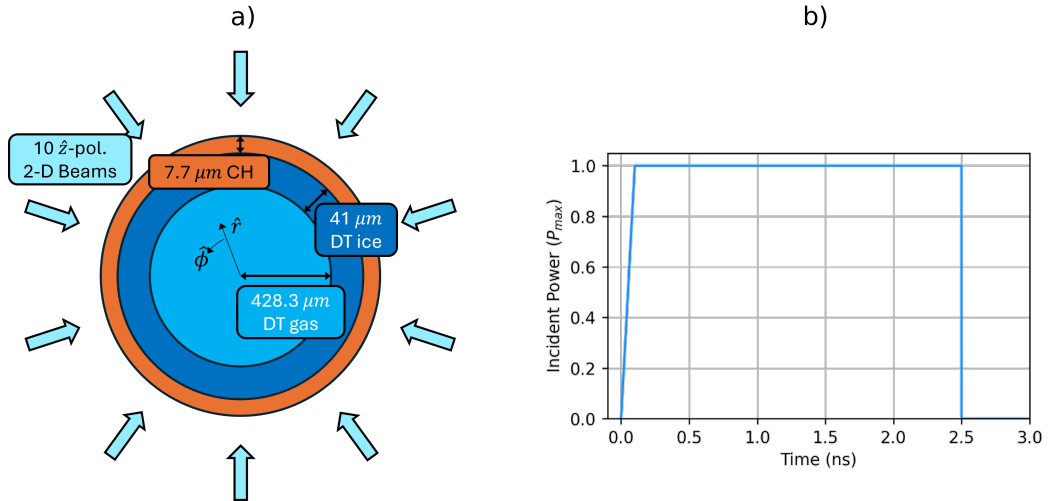


Figure 2.4: The a) target initial conditions with beam geometry, and b) pulse shape used for the 2-D cylindrical simulations. All beams were polarised out of the simulation plane, in the $+\hat{z}$ direction. Initial layer radii were taken from the initial conditions for OMEGA shot 89224, presented in Fig. 1.22.a.

drawn from the work done here to spherical implosion data. Cylindrical implosion experiments are also conducted on laser facilities, which explicitly relate their work to spherical implosions, suggesting that the approach is valid and accepted within the community [107, 108]. Although the differences between the two regimes are not quantified in the work conducted in this chapter, future work could be done to extend the platform to a 2-D ‘plane’ in spherical rather than cylindrical geometry, which would capture the spherical convergence of the target and divergence of the coronal flow. This is discussed in more detail at the end of the chapter, in Sec. 2.5.

2.2.2 Pulse Shape and Target Initial Conditions

The base simulation initial conditions are plotted in Fig. 2.4. The initial conditions are symmetric about the azimuth and in the plane normal to the \hat{z} direction. A target with the same initial layer radii as OMEGA shot 89224 was constructed with a DT gas fill, a layer of DT ice and a CH plastic ablator with vacuum outside, shown in Fig. 2.4.a. 10 beam were placed around the target, equally space in azimuthal angle and all were polarised in the out of plane, \hat{z} direction. The beams all had super-Gaussian spot profiles with $n_s = 5.2$ and σ set by Eq. 2.2. A simple, 2.5 ns square pulse (including a 0.1 ns ramp to full power) was used for all simulations, plotted in Fig. 2.4.b. The maximum power of the pulse for each 2-D simulation was tuned from a separate set of 1-D simulations, such that the bangtime occurred at 2.5 ns.

By tuning the simulations such that the bangtime was consistent across all simulations, the coupled energy and implosion velocity was kept the same across all implosions. The difference between implosions was therefore primarily due to differences in the spatial location of the deposited power. If the incident energy were fixed, increasing R_b/R_t would lead to more CBET, which would result in less energy coupled to the target. Therefore, to compare simulations, the target would also have to be altered to reduce the imploding mass

Table 2.1: Results of the 1-D Tuning Simulations.

R_b/R_t		P_{\max} (TW/cm)	I_0 (10^{14} W/cm 2)	t_{bang} (ns)	Y_{DT} (10^{13} /cm)
0.75	No CBET	54.44	0.85	2.49	1.53
	CBET			2.51	1.44
0.80	No CBET	58.25	0.83	2.49	1.56
	CBET			2.51	1.45
0.85	No CBET	63.44	0.83	2.48	1.67
	CBET			2.51	1.43
0.90	No CBET	70.00	0.85	2.47	1.82
	CBET			2.50	1.41
0.95	No CBET	77.94	0.89	2.46	1.99
	CBET			2.49	1.49
1.00	No CBET	87.25	0.93	2.45	2.15
	CBET			2.49	1.60
1.05	No CBET	97.94	0.99	2.46	2.27
	CBET			2.50	1.61
1.10	No CBET	110.00	1.06	2.47	2.31
	CBET			2.51	1.52

with less coupled energy. This was deemed beyond the scope of the work presented in this chapter and therefore only the incident energy was altered to maintain the 1-D implosion hydrodynamics.

Every simulation in this chapter used a grid with radial extent $r \in [0, 1600]$ with resolution $\Delta r = 1 \mu\text{m}$ and 256 cells in the azimuthal direction. A tabulated Sesame table of state was used for each material [76] and thermal conduction routine was solved using an Alternating-Direction Implicit (ADI) method with flux-limited Spitzer conductivities [109]. The electron flux limiter was set using the default CHIMERA direct-drive setting, outlined in Eq. 1.44. Radiation transport was not included in simulations, because the small cells on the $r = 0$ boundary led to significant computational expense. 1-D calculations showed that the effect of including radiation transport was relatively small. The dominant effect was that radiation transport reduced the bangtime by ~ 0.1 ns, primarily due to temperature losses in the corona. Future work could therefore include the dominant radiation effect by using a radiative loss model rather than full transport.

2.2.3 1-D Implosion Tuning

As already mentioned, the energy of the laser was varied to maintain a consistent bang-time across all R_b/R_t values, so that the target parameters did not have to be separately optimised for each simulation. This was done via a series of 1-D, with-CBET simulations which varied the maximum power of each beam, P_{\max} , at each R_b/R_t to obtain an implo-

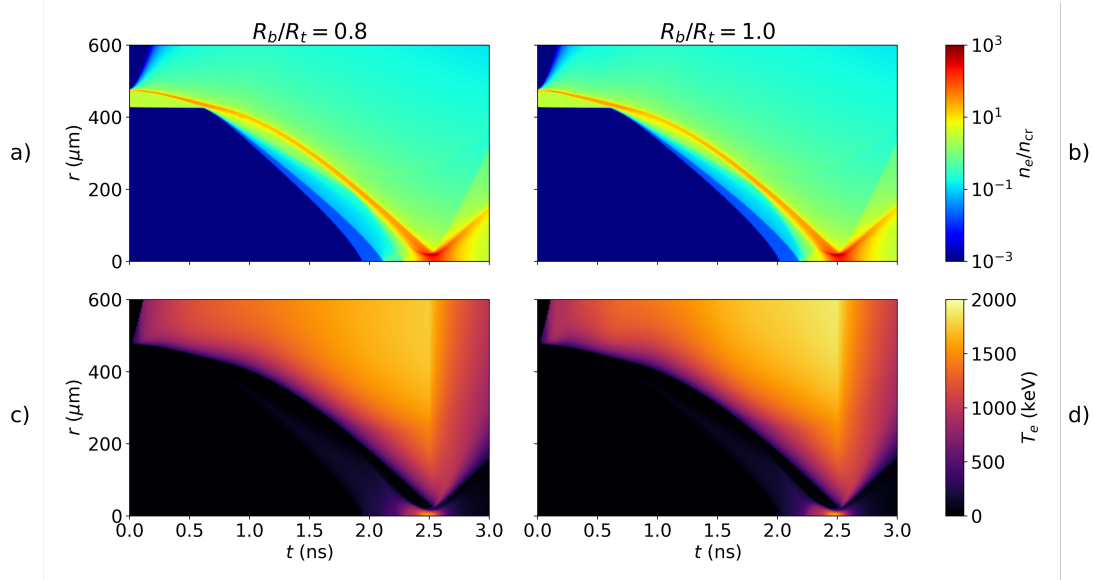


Figure 2.5: Streak plots from two of the 1-D tuning simulations including CBET. Panels a) and b) plot the electron density of the $R_b/R_t = 0.8$ and $R_b/R_t = 1.0$ simulations respectively, as a function of time (x -axis) and radius (y -axis). Panels c) and d) plot the electron temperature for the $R_b/R_t = 0.8$ and $R_b/R_t = 1.0$ simulations respectively.

sion with $t_{\text{bang}} = 2.50 \pm 0.01$ ns. For no-CBET simulations, the absorbed power vs time from the CBET simulation with the same R_b/R_t was enforced. Thus, when comparing any two simulations, the absorbed energy is equivalent, but the spatial location of the deposition is different. This manifests both as different azimuthal asymmetries in the deposition, which alters the stagnation state asymmetry, and different radial location of absorption. For example, the with-CBET power deposition occurs at slightly larger radii compared to no-CBET profiles, as is shown in Fig. 1.24. This means that the no-CBET implosions have a slightly increased drive efficiency compared to CBET implosions, because thermal conduction does not have to transport energy as far from the absorption region to the ablation surface.

Tab. 2.1 shows implosion metrics from all the tuned 1-D implosions. As can be seen, the incident maximum power of each beam for the CBET simulations, P_{\max} , increases with increasing R_b/R_t because larger R_b/R_t leads to more CBET and therefore less absorption, so more incident power is required to maintain the same absorbed energy. The maximum intensity of each beam at peak power, I_0 is non-monotonic, because although the maximum power increases, the beam radius also increases, which limits the increase in maximum intensity. As can be seen, bangtimes and yields are similar across all simulations. Note that at increasing R_b/R_t , bangtime and yield difference between the CBET and no-CBET results at the same R_b/R_t increase. This is because more CBET occurs for the larger R_b/R_t simulations and therefore the difference in deposition radius increases between CBET and no-CBET simulations, marginally improving the effective drive efficiency of the no-CBET results.

Streak plots, which plot hydrodynamic quantities as a function of radius and time, of n_e and T_e are plotted in Fig. 2.5 for 1-D, with-CBET simulations at two separate R_b/R_t values.

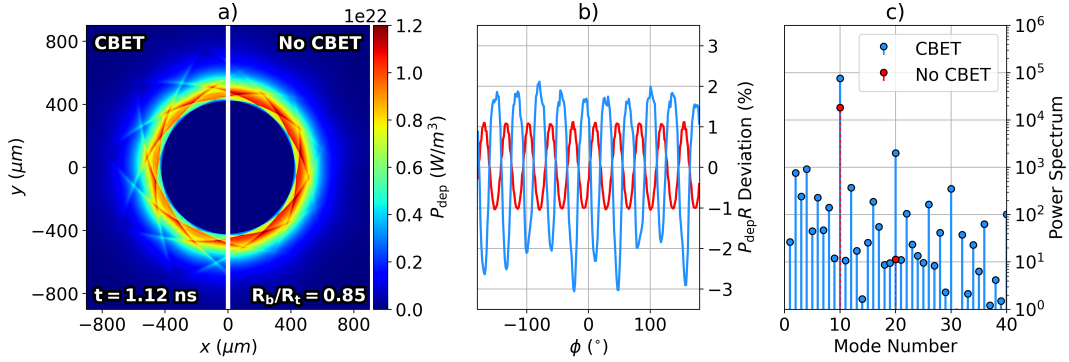


Figure 2.6: Demonstration of the analysis workflow to obtain the key results for this chapter. The power deposition at $t = 1.12$ ns from the CBET (left) and no-CBET (right) simulations are plotted in panel a) for the $R_b/R_t = 0.85$ case. Panel b) plots the radially integrated deposition from the profiles in a) as a function of azimuthal angle. It can be seen from this plot, that the CBET asymmetry (light-blue) is greater than the no-CBET asymmetry (red). The power spectrum of these profiles is then plotted in panel c). This demonstrates that the dominant modes in the spectrum are multiples of the number of beams.

Qualitatively, the 1-D implosion trajectories from these plots are similar. Small differences in shock timing exist between simulations, as is evidenced by the initial shock for the $R_b/R_t = 0.8$ hitting the $r = 0$ axis at $t \sim 1.9$ ns, which is about 0.1 ns earlier than the $R_b/R_t = 1.0$ simulation ($t \gtrsim 2.0$ ns). Despite these small differences in both the metrics from Tab. 2.1 and the streaks from Fig. 2.5, all simulations were deemed sufficiently similar that implosions could be cross-compared.

2.3 Asymmetry of Deposited Power

This section describes the asymmetry of the deposited power profile for simulations with and without CBET. The effect of this asymmetry on the in-flight and stagnation state hot-spot profiles are discussed in Sec. 2.4. Analysis of the deposited power profile shows that the growth of asymmetries in the target are the result of a complex, space- and time-dependent evolution of the deposition. In the absence of CBET, *modal-flips* of the deposition occur, where the phase of the driving asymmetry flips in time, due to the overlapping beam intensity changing in the region where Inv-Brem deposition is important. The pattern of these modal flips depend on the width of the beams, the time-dependent convergence of the target and the time-dependent coronal plasma altering the radius above the target where deposition is important. It is observed that in the presence of CBET, due to the non-uniform resonance of CBET gains across inbound laser sheets, additional asymmetries in the deposition are seeded and lead to more modal-flips than are observed without CBET.

2.3.1 Analysis and Quantity Definitions

Initially, definitions of key variables used in the analysis of the results of the chapter shall be provided. These are introduced for the example of the with-CBET and no-CBET $R_b/R_t = 0.85$ simulations, plotted instantaneously at $t = 1.12$ ns in Fig. 2.6.

Fig. 2.6.a shows the volumetric deposited power for the CBET (left) and no-CBET (right) simulations. Note that, as described in Sec. 2.2.3, the no-CBET simulation is forced to absorb the same magnitude of power as a function of time as the CBET simulation. Therefore, the total absorbed power is identical for both simulations, even though the no-CBET plot appears more saturated on the colour scale. This difference in saturation is partially due to the non-linear colour scale used for the plot, and also because the CBET result has more power deposited at larger radii, which widens the profile and reduces saturation on the colour scale. The mode-10 in the deposition due to the number of beams is clearly visible on both plots. Significant deposition in the caustic region, especially for the CBET result, is visible as the cross-structure in the deposited power. This suggests (and shall subsequently be shown explicitly in Sec. 2.3.3), that the caustic fields are strongly amplified by CBET, leading to more Inv-Brem in this region.

In order to quantify azimuthal asymmetry, radial integrals of the deposited power and fuel density are taken,

$$\begin{aligned} P_{\text{dep}}R(\phi) &= \int_{r=0}^{\infty} P_{\text{dep}}(r, \phi) dr, \\ \rho_{\text{DT}}R(\phi) &= \int_{r=0}^{\infty} \rho_{\text{DT}}(r, \phi) dr, \end{aligned} \quad (2.8)$$

where P_{dep} is power, in units [W/m^3], unlike the volumetric power plotted in Fig. 2.6.a. The deviation from the mean of these profiles can then be taken,

$$\text{Deviation}(f[\phi]) = \frac{f[\phi] - \int_{-\pi}^{\pi} f[\phi] d\phi}{\int_{-\pi}^{\pi} f[\phi] d\phi}. \quad (2.9)$$

The deviation of the CBET and no-CBET deposited power profiles shown in Fig. 2.6.a are plotted in Fig. 2.6.b. It can be seen that at this time, CBET considerably amplifies the instantaneous deposition asymmetry. It also distorts the sinusoidal profile of the no-CBET simulation, marginally widening and narrowing the curve peaks and troughs respectively. Interestingly, CBET has also resulted in a phase-inversion of the deposition profile, where the peaks of the CBET deviation occur at the angles of the troughs of the no-CBET curve. This behaviour shall be called a *modal-flip* throughout this chapter. Note that modal-flips are also observed in the same simulation through time, *i.e.* as the target converges, the beam overlap pattern changes which results in phase inversions of the deposition, relative to earlier deposition profiles.

A Discrete Fourier Transform (DFT) is then used to analyse the modes which contribute to the signal. A signal $f(\phi)$, which is sampled N times in the interval $\phi \in [\phi_{\min}, \phi_{\max}]$ where

$n = 0 \rightarrow N - 1$, has a DFT defined by,

$$F_\ell = \sum_{n=0}^{N-1} f_n \exp\left(-i2\pi \frac{\ell}{N} n\right), \quad (2.10)$$

where f_n is the sample at $\phi = (\phi_{\max} - \phi_{\min})n/N$ and ℓ is the frequency mode number. The power spectrum, which gives the power of each mode, is then given by,

$$P_\ell = \frac{1}{N^2} |F_\ell|^2. \quad (2.11)$$

The power spectra of the deposited power deviations from Fig. 2.6.b are plotted in Fig. 2.6.c on a log scale. The no-CBET profile is dominated by the $\ell = 10$ mode, with only a small $\ell = 20$ present. This yields the sinusoidal curve in Fig. 2.6.b. Many more modes are present for the CBET power spectrum, and (compared to the no-CBET results) a clear amplification of multiples of the $\ell = 10$ are visible. The significant $\ell = 20$ distorts the curve in Fig. 2.6.b, slightly widening the peaks and narrowing the troughs. Modes with $\ell < 10$ are presumed to be mostly spurious and introduced by relatively small, instantaneous errors in the field reconstruction algorithm. Unlike the $\ell = 10, 20, 30, \dots$, the $\ell < 10$ exhibit oscillatory, random growth from timestep to timestep. Therefore, they do not significantly imprint on the hydrodynamic profiles over the timescale of the implosion.

2.3.2 Deposition Asymmetries in the Absence of CBET

This section presents results of the deposited power in the absence of CBET for several implosions. Plotted in Figs. 2.7.a, 2.7.c and 2.7.e are $P_{\text{dep}} R(t, \phi)$ for $R_b/R_t = 0.8, 0.9$ and 1.0 respectively. Explicitly, this is the radially integrated power from Eq. 2.8, plotted as a function of time (x -axis) and azimuthal angle (y -axis). The $\ell = 10$ deposition asymmetry at a single time (for example the red curve in Fig. 2.6.b) is visible as ten peaks to troughs along a vertical lineout. As expected, comparison of the colour scale saturation between these three plots demonstrates that at smaller beam radii, no-CBET asymmetries are much more significant. Figs. 2.7.b, 2.7.d and 2.7.f plot the power spectrum amplitude of the dominant $\ell = 10$ and 20 modes, as a function of time, on a log scale.

At times $t \sim 0.7, 0.9$ and 1.1 ns for the $R_b/R_t = 0.8, 0.9$ and 1.0 simulations respectively, a modal-flip of the deposited power is observed. This occurs because the plasma scale length increases in time, widening the plasma region above the critical surface where Inv-Brem is significant. Thus, the wings of the beams, which do not penetrate as far radially in, contribute more to deposition after this longer scale-length coronal plasma region has evolved. This eventually leads to a modal flip, when more deposition occurs between beam angles than at the angle of the beam itself. The flips occur later in time for wider beams, because the wings of the beams penetrate less far into the plasma, so a longer plasma scale length must develop before deposition from these edge rays becomes significant.

This is shown explicitly in Fig. 2.8, which plots the P_{dep} profiles for the $R_b/R_t = 0.8$, no-CBET simulation at $t = 0.6$ ns, $t = 0.7$ ns and $t = 0.8$ ns, i.e. just before, during and after the

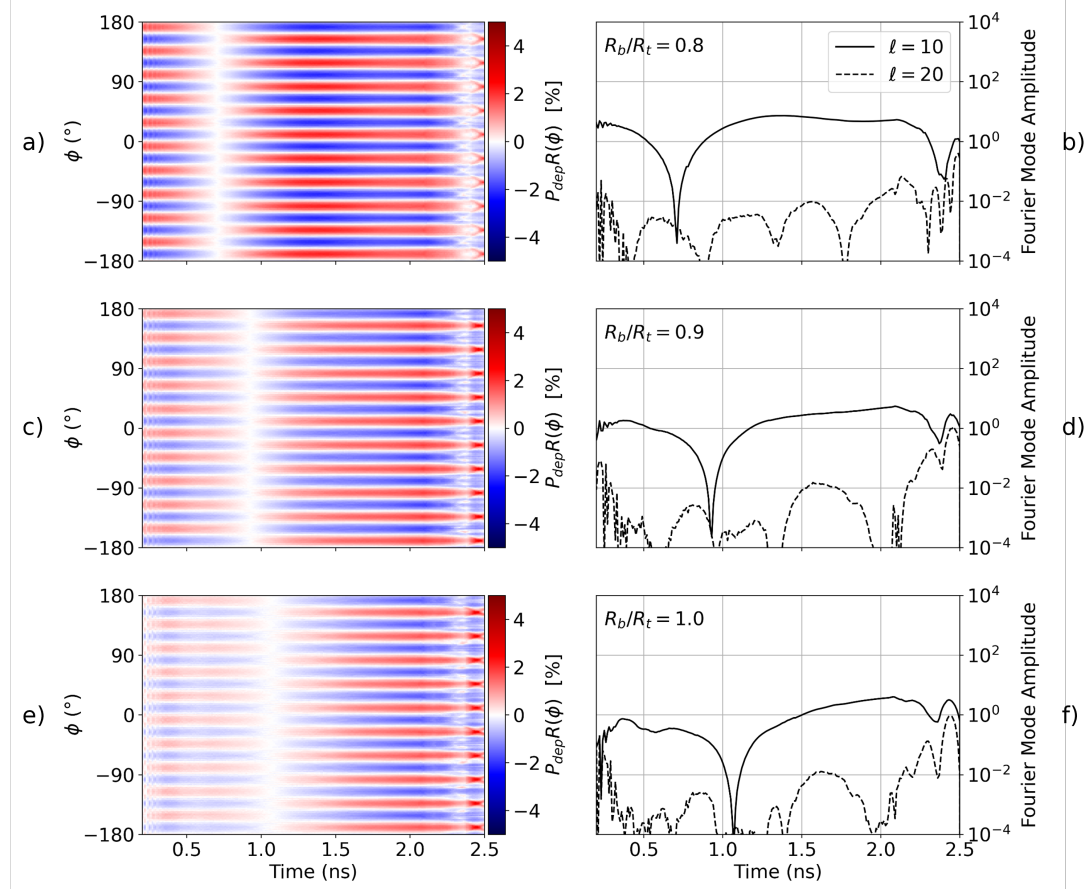


Figure 2.7: Radially integrated deposited power from no-CBET simulations as a function of time (x -axis) and angle (y -axis), alongside amplitudes of the dominant modes from a Fourier power spectrum. Panels a) and b) plot the radially integrated deposited power and Fourier modes respectively for the $R_b/R_t = 0.8$ simulation. The same is plotted for the $R_b/R_t = 0.9$ simulation in c) & d) and for the $R_b/R_t = 1.0$ simulation in e) & f). The mode 10 from the number of beams is clearly visible in the radially integrated power plots as 10 peaks to troughs in angle at a given time, *i.e.* 10 cyclical perturbations along a vertical lineout.

modal-flip respectively. Particularly, Fig. 2.8.d plots the radially integrated powers plotted in Figs. 2.8.a, 2.8.b and 2.8.c. Before the modal-flip, at $t = 0.6$ ns, maximum deposition occurs at the angles of the beams, shown by dashed magenta lines. During the flip, at $t = 0.7$ ns, very symmetric deposition is observed and just after, at $t = 0.8$ ns, maximum deposition occurs between beam angles. Examining Figs. 2.8.a, 2.8.b and 2.8.c, the highlighted ‘cross’ feature (white dashed circle) between beam angles becomes increasingly saturated as more Inv-Brem occurs here. This occurs due to the plasma scale length increasing, raising the density further away from the critical surface and thus increasing deposition where the wings of neighbouring beams overlap.

2.3.3 CBET Imprint on Incident Field

When CBET is included in these simulations, it acts to significantly alter the field structure of the inbound laser sheets. This leads to additional asymmetry in the deposition, which

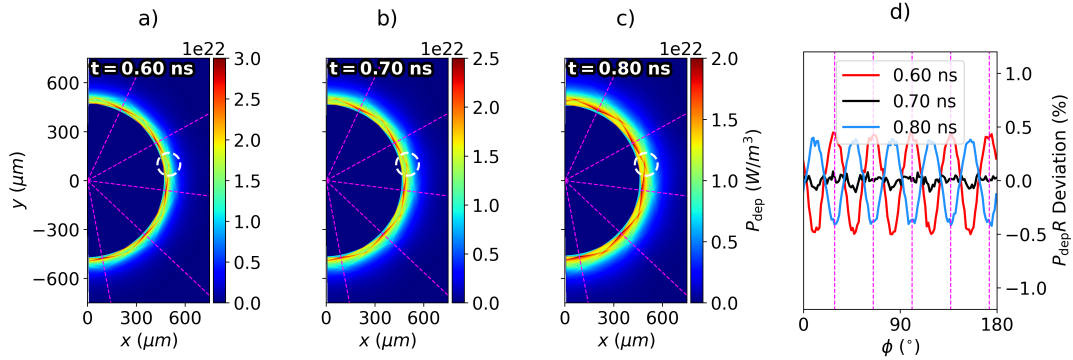


Figure 2.8: Demonstration of a mode-flip in P_{dep} for the no-CBET $R_b/R_t = 0.8$ simulation. Panel a), b) and c) plot the power deposition just before, during and just after the mode-flip. Panel d) plots the deviation from the mean of the radially profiles around the azimuthal angle for all 3 times. It can be seen from this plot that the deposition is very symmetric at $t = 0.7$ ns. In all 4 panels, the angles of the beams are shown by the dashed magenta lines. The overlap region where deposition rises as the scale length increases, is highlighted with a white circle in panels a), b) and c).

predominantly occurs closer to the critical surface than the CBET scattering. Extra asymmetry is introduced, because the resonant CBET interaction is spatially localised, as opposed to azimuthally symmetric around the target. Fig. 2.9.a illustrates this, by plotting the electric field magnitude from the incident sheet of ‘beam-1’ from the $R_b/R_t = 0.9$ CBET simulation at $t = 1.0$ ns, along with the $|E_z^{\text{in}}| = 1 \times 10^{10} \text{ Vm}^{-1}$ contour of ‘beam-4’ (magenta line). These two beams are separated from each other by 108° . It can be seen that there are two ‘holes’ in the beam-1 incident field profile, on either side of the beam centre. These are due to CBET interactions with other beams, for example, the resonance with the caustic field region of beam-4 is responsible for the hole at $[x, y] \sim [-500, -400] \mu\text{m}$. Typically, a large fraction of CBET scattering occurs in the caustic field region of beams for direct-drive implosions, due to the refractive swelling of the ray amplitude and therefore large electric fields present [25]. Caustic regions are narrow structures, typically with width $\sim \mathcal{O}(\lambda_0)$, therefore the region of maximal CBET scattering is strongly localised, leading to the non-uniform imprint on the fields of inbound beams.

The trajectory that the light follows, and therefore the location of the caustic, depend on the electron density profile. For a direct-drive implosion, the critical density falls inward throughout the implosion, leading to a caustic field structure which ‘wraps around’ the target more, *i.e.* rays at an equivalent impact parameter are deflected less, as the critical radius converges. This can be seen by comparing Fig. 2.9.a ($t = 1.0$ ns) and Fig. 2.9.b ($t = 1.5$ ns), with critical radii $r_{\text{cr}} \sim 430$ and $360 \mu\text{m}$ respectively. The shrinking of r_{cr} has allowed beam-4 to wrap around the target more, such that the caustic CBET interaction now occurs in the middle of the incident field of beam-1. Comparing the field structures from Fig. 2.9.a and Fig. 2.9.b, the deposition of beam-1 at $t = 1.0$ ns will peak at the incident beam angle due to the depleted field on either side, whereas at $t = 1.0$ ns, the depletion of the field in the

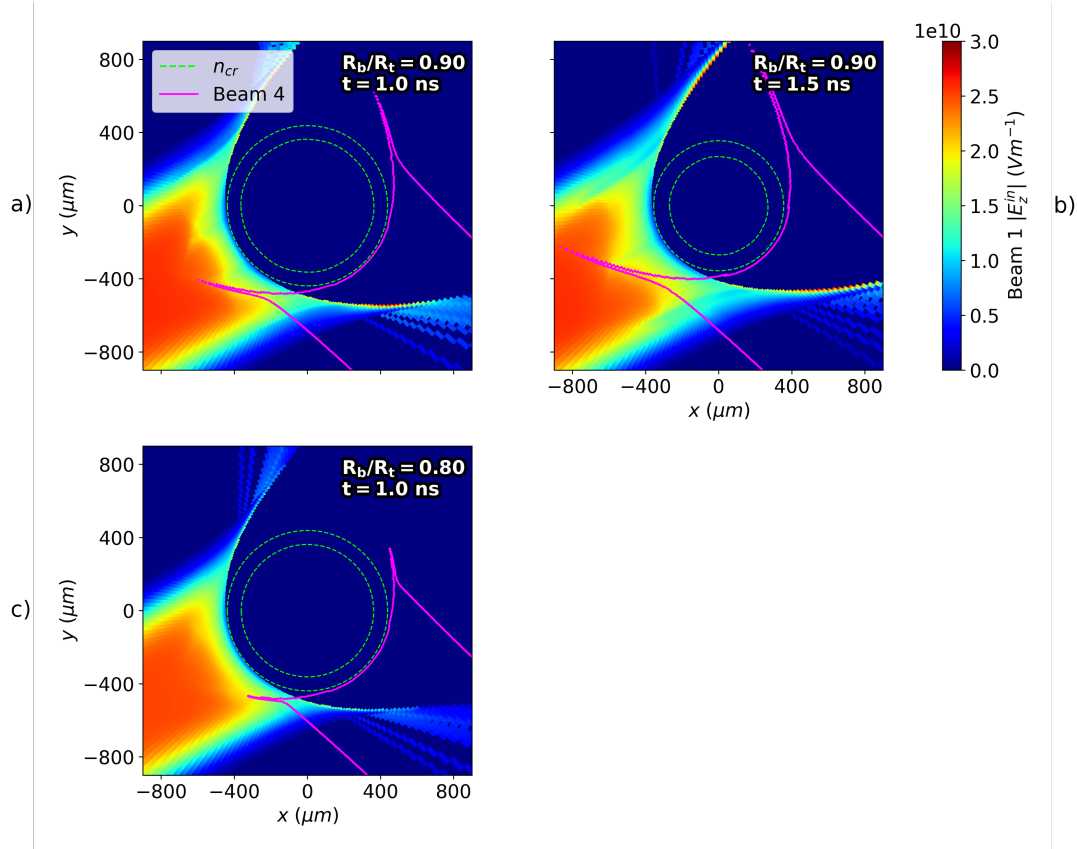


Figure 2.9: Field structure which leads to CBET induced asymmetry on power deposition and its dependence on R_b/R_t and target convergence. Each panel plots the incident sheet field, which includes the effect of CBET, along with contours of the critical electron density (green) and the incident field, $|E_z^{\text{in}}| = 1 \times 10^{10} \text{ Vm}^{-1}$ contour of another beam (magenta). Panel a) and b) plot this for the $R_b/R_t = 0.9$ simulation at $t = 1.0 \text{ ns}$ and $t = 1.5 \text{ ns}$ respectively. The convergence of the target in this time interval, leads to beams wrapping around the target more, and therefore a change in the spatial location of the resonant CBET interaction. Panel c) plots the same for the $R_b/R_t = 0.80$ simulation at the same time as panel a). This demonstrates that the $R_b/R_t = 0.80$ beam is not wide enough at this time to lead to a resonant CBET interaction, unlike the wider beam in panel a).

beam centre will shift the $P_{\text{dep}} R$ maxima in azimuthal angle. In other words a modal flip of the power deposition occurs between these times, which is due to the localised caustic CBET interaction changing location as the target converges.

Fig. 2.9.c plots the same as Fig. 2.9.a, but for the $R_b/R_t = 0.80$ case, *i.e.* a much narrower beam. From this plot, it can be seen that unlike for the $R_b/R_t = 0.9$ case, beam-4 does not wrap around the target enough for its caustic region to deplete beam-1, leading to a relatively unperturbed incident field profile. This demonstrates that the CBET induced modal flips are different for implosions with different R_b/R_t , because narrower (wider) beam will wrap around the target less (more) at an equivalent critical radius. Therefore, larger R_b/R_t values allow more modal flips to occur, because at a given critical radius, wider beams wrap around more, and therefore can undergo CBET with beams which have a larger angular separation.

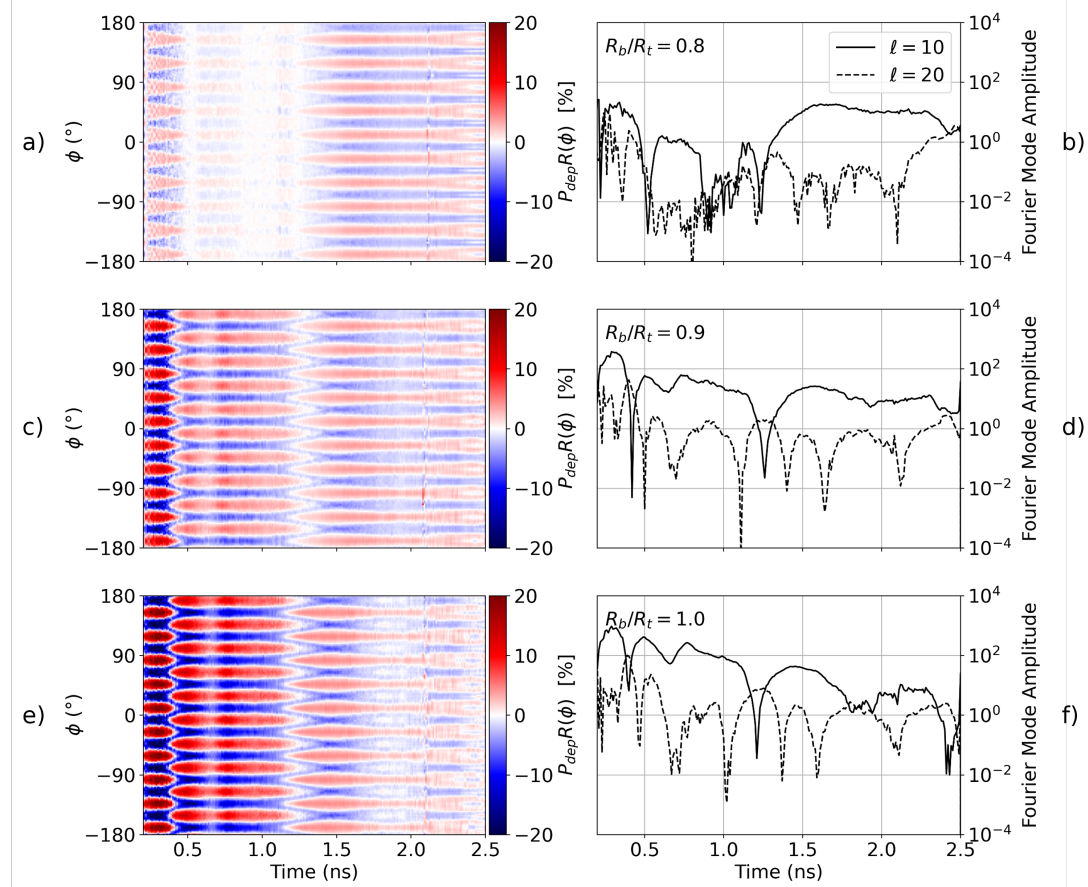


Figure 2.10: This figure plots the same as Fig. 2.7, but now for the equivalent simulations which include the effect of CBET. Comparing these results and those in Fig. 2.7 demonstrates that CBET introduces additional modal-flips of the deposition and amplifies the magnitude of asymmetries.

It is important to note that although this analysis only considers a single beam, the coronal hydrodynamic profiles are approximately azimuthally symmetric and therefore the beams and CBET interactions have rotational symmetry.

2.3.4 Deposition Asymmetries in the Presence of CBET

Results shall be presented in this section of the P_{dep} asymmetries for simulations including CBET, contrasted to Sec. 2.3.2, which presented results for the no-CBET simulations. Similarly to Fig. 2.7, plotted in Figs. 2.10.a, 2.10.c and 2.10.e are $P_{\text{dep}} R(t, \phi)$ for $R_b/R_t = 0.8, 0.9$ and 1.0 respectively. Note that in these plots, the colour scale saturates at 20% rather than 5% , which demonstrates that instantaneous deposition asymmetries are typically much larger when the effects of CBET are included. A small discontinuity is visible in these plots at $t \sim 2.15$ ns, which is the time that the critical density passes from the CH ablator material into the DT fuel. Mix between these materials is not modelled in CHIMERA, so this critical density traversal leads to short-lived, potentially spurious, radially outward ∇n_e near the critical radius, which are visible in the field reconstruction and deposition.

The $P_{\text{dep}} R$ plots in Fig. 2.10 have significantly more structure than the equivalent no-CBET

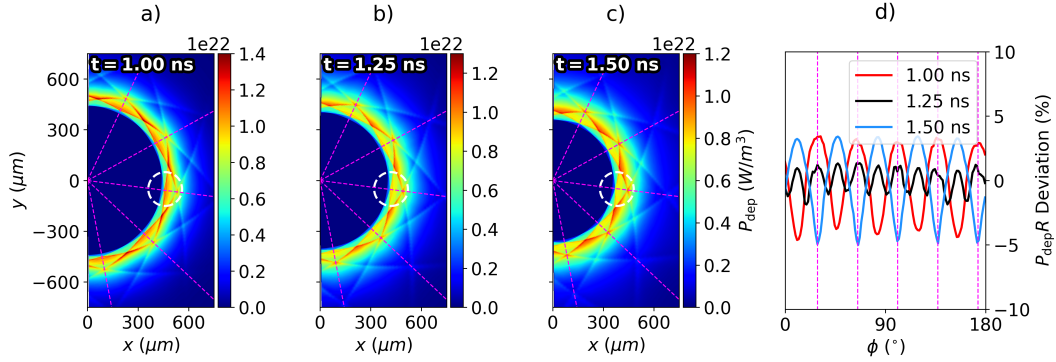


Figure 2.11: Demonstration of a mode-flip in P_{dep} for the CBET, $R_b/R_t = 0.9$ simulation. Panels a), b) and c) plot the power deposition before, during and after the mode-flip. Panel d) plots the deviation from the mean of the radially profiles around the azimuthal angle for all 3 simulations. Fig. 2.9.a and Fig. 2.9.b plot a single, incident sheet field from panels a) and c) respectively. It can be seen that the centre of the beam depletion at $t = 1.5 \text{ ns}$ leads to less deposition at the beam angles (magenta lines) on panel d). Panel b) shows that during the CBET induced mode-flip, a significant $\ell = 20$ occurs in the deposition. The reducing absorption at the centre of one beam is highlighted in by the white dashed circles.

plots in Fig. 2.7. There is an increase in the number of mode-flips, increasing R_b/R_t appears to increase deposition asymmetry (rather than decrease for no-CBET) and more significant higher modes also appear to be present in $P_{\text{dep}}R$. Figs. 2.10.b, 2.10.d and 2.10.f plot the $P_{\text{dep}}R$ Fourier power spectrum amplitudes of the modes $\ell = 10$ and 20 throughout the implosion. The mode-flips can be identified in these plots as the times at which the $\ell = 10$ sharply falls and then quickly rises again.

Comparing Fig. 2.7 and Fig. 2.10, CBET leads to a mode-flip in the deposition at $t \sim 0.4 \text{ ns}$, which does not occur for the no-CBET case. The resulting $\ell = 10$ in the CBET deposition profiles between $t \sim 0.4 \text{ ns}$ and $t \sim 1.2 \text{ ns}$ strongly depends on the R_b/R_t value. For the $R_b/R_t = 0.8$, CBET simulation, the $\ell = 10$ amplitude is low compared to the larger R_b/R_t , CBET simulations. This is because the relatively narrow beams at this time do not sufficiently wrap around the target to give rise to strong caustic fields and subsequent CBET imprints on incident beams. This is seen explicitly, by comparing the incident field profiles at $t = 1.0 \text{ ns}$ for the $R_b/R_t = 0.9$ and 0.8 simulations plotted in Figs. 2.9.a and 2.9.c respectively.

Interesting behaviour is also observed later in the implosion. Comparing the $R_b/R_t = 0.9$ (Fig. 2.10.c) and 1.0 (Fig. 2.10.e) plots at $t \sim 1.8 \text{ ns}$, it can be seen that an additional mode-flip is beginning to develop for the $R_b/R_t = 1.0$ case. This is also seen in Figs. 2.10.d and 2.10.f, by the reduction in amplitude of the $\ell = 10$ and rise of the $\ell = 20$. However, the $R_b/R_t = 1.0$ beams are not quite wide enough to fully translate to an inversion of the deposition asymmetry, so this results in a net decrease in $P_{\text{dep}}R$ asymmetry, compared to the $R_b/R_t = 0.9$ simulation at the same time.

Fig. 2.11 plots the development of the mode-flip which occurs at $t \sim 1.25 \text{ ns}$. Figs. 2.11.a, 2.11.b and 2.11.c plot the deposited power from all beams before, during and after the flip re-

spectively. As can be seen in the area highlighted by the dashed white circles in each plot, the deposition at the angle of the beams (magenta dashed lines) becomes less significant, compared to the angles between beams. Figs. 2.11.a and 2.11.c are from the same time as the single field profiles plotted in Figs. 2.9.a and 2.9.b respectively. These field profiles demonstrate that CBET scattering in the caustic region of the beams separated by 108° , is responsible for the depletion of the inbound beams on either side of the beam centre at $t = 1.0$ ns and in the beam centre at $t = 1.5$ ns. The radially integrated deposition is plotted in Fig. 2.11.d, which shows the $\ell = 20$ of the deposited power during the mode-flip.

2.4 Stagnation State Asymmetry

This section describes how the asymmetry of the deposition profiles, described in Sec. 2.3, imprint upon the hydrodynamics. The stagnation profiles for various R_b/R_t are presented for CBET and no-CBET simulations. These demonstrate that CBET tends to increase the asymmetry of the stagnated state, due to the decreased absorption uniformity. It is observed that CBET changes the trend of the stagnation symmetry with R_b/R_t . While, for the no-CBET simulations, symmetry increases with increasing R_b/R_t , CBET generally reverses this behaviour, with the least symmetric stagnation states observed for the largest R_b/R_t value. The CBET trend is, however, non-monotonic which is due to development of additional mode-flips at specific values of R_b/R_t , slightly increasing the deposition uniformity late in the implosion.

2.4.1 Stagnation State Asymmetry Trend with Beam Radius

Fig. 2.12 plots the stagnation fuel density and ion temperature for both CBET and no-CBET simulations at 4 different R_b/R_t . The beam-mode $\ell = 10$ is clearly identifiable in all plots. Recall that all simulations are tuned to have the same amount of absorbed laser energy, via the tuning process described in Sec. 2.2.3. Therefore, all profiles have approximately the same convergence properties. If 1-D effects of CBET were included, which would involve a much more complex, simultaneous optimisation of pulse and target, the stagnation state of all simulations would likely look far less similar. No-CBET and smaller R_b/R_t results would have significantly more coupled energy, and would therefore have more mass in the final fuel configuration. Instead, these results effectively show, for hydrodynamically similar implosions, how CBET and increasing R_b/R_t affects deposition and stagnation *symmetry* only. This, simpler optimisation also has the advantage that the final fuel configurations do appear more similar and are therefore directly comparable.

The no-CBET results clearly show a trend of increasing stagnation symmetry with increasing R_b/R_t , as expected from the plots in Fig. 2.7, which showed increasing absorption uniformity with increasing beam radius. The pressure of the stagnation state is approximately isobaric, and therefore the temperature profiles are inversely proportional to the density. Peak densities increase and the radii of stagnation decrease marginally as R_b/R_t increases. This improved compression is partially due to increased symmetry providing better com-

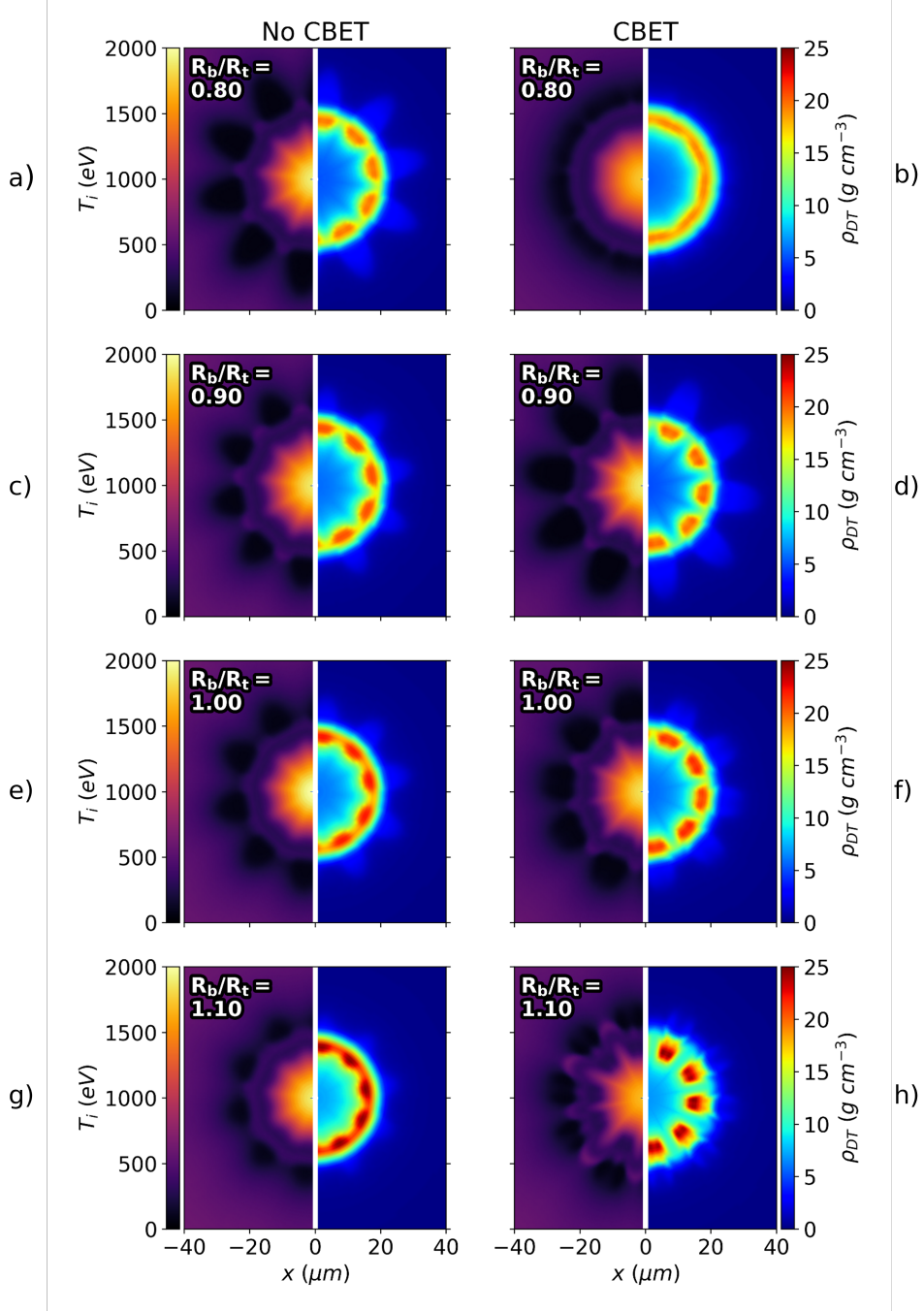


Figure 2.12: Densities of the DT fuel and ion temperatures for various R_b/R_t simulations both with and without CBET. Each row corresponds to a different R_b/R_t value; the left column contains simulations without CBET; and the right column contains simulations with CBET. It is visible from the density plots that increasing R_b/R_t improves stagnation symmetry for the no-CBET simulations, but degrades it for the CBET simulations.

pression, but more optimal shock timing for the larger R_b/R_t implosions also contributes. As is seen in the streak plots in Fig. 2.5, the tuning process led to the first shock hitting the axis slightly earlier at narrower R_b/R_t , than for the larger R_b/R_t implosions. Although the streak plots are for 1-D with-CBET simulations, the same trend is observed for the 2-D with-

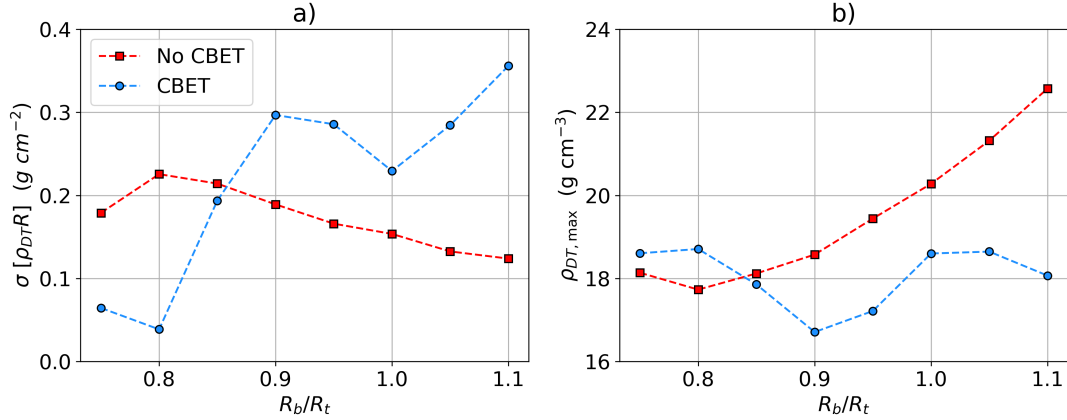


Figure 2.13: Trends of a) stagnation asymmetry and b) maximum (azimuthally averaged) fuel density for CBET and no-CBET simulations. The no-CBET improvement in symmetry with R_b/R_t is observed which also corresponds to improved compression. The symmetry trend including CBET is more complex, but broadly the stagnation state symmetry is worse with increasing R_b/R_t .

and without-CBET simulations. The more optimal shock timing for larger R_b/R_t also has the signature of higher on-axis densities. The contribution of small differences in shock timing is not quantified in the following analysis, but it is assumed that it will have a second-order effect on the stagnation uniformity, compared to asymmetry in deposition.

Increasing R_b/R_t when including CBET broadly shows the opposite behaviour to the no-CBET simulations, leading to highly non-uniform density profiles at large R_b/R_t . This trend was also observed in the deposition plots in Fig. 2.10, with the wider beam simulations leading to a more saturated plot on the colour scale. Higher order modes than $\ell = 10$ also become increasingly evident in the wider beam CBET simulations. Note that the $R_b/R_t = 0.8$ simulation with CBET is more symmetric than the no-CBET simulation at the same beam radius. This is believed to be due to the developing mode-flip, visible in Fig. 2.10.a from $t \sim 0.5 \rightarrow 1.3$ ns, which strongly reduces the absorption asymmetry and subsequent imprinting onto the density.

The standard deviations of the radially integrated stagnation state fuel density,

$$\sigma[\rho_{DT}R] = \sqrt{\langle \rho_{DT}R^2 \rangle - \langle \rho_{DT}R \rangle^2}, \quad (2.12)$$

for the CBET and no-CBET simulations are plotted as a function of R_b/R_t in Fig. 2.13.a. The no-CBET trend from this metric clearly follow the behaviour seen in Fig. 2.12, that increasing beam width results in better symmetry of the hydrodynamic profiles at stagnation. Note that the $R_b/R_t = 0.75$ simulation value is more symmetric than the 0.8 result, suggesting that more complex behaviour may occur at smaller beam radii, $R_b/R_t < 0.8$. However, this is outside the range of typical OMEGA implosions and therefore not studied in detail. The with-CBET curve shows a broad trend of increasing asymmetry with wider beams, which is visible in the stagnation profiles in Fig. 2.12, however the behaviour is clearly more complex than the no-CBET simulations. A local maximum of asymmetry is observed at $R_b/R_t = 0.9$

and minima occur at $R_b/R_t = 0.8$ and $R_b/R_t = 1.0$. As shall be described in the subsequent section, Sec. 2.4.2, these features are explained by the complex, CBET induced modal-flips of the deposition which were described in Sec. 2.3.4.

The azimuthally averaged maximum density,

$$\rho_{DT,max} = \max \left(\int_{-\pi}^{\pi} \rho_{DT}(r, \phi) d\phi \right), \quad (2.13)$$

is plotted in Fig. 2.13.b for both sets of simulations. The behaviour in this plot is inversely proportional to the standard deviation, which suggests that the asymmetry of the density has a detrimental effect on the compression of the target. Lower modes can prove detrimental to compression by introducing significant non-radial motion, resulting in less efficient compression [110, 111]. The (unintended) improved shock timing at larger beam radii does appear to somewhat compensate for the reduction in uniformity, *i.e.* the compression metric at $R_b/R_t = 1.05$ is about the same as $R_b/R_t = 0.8$, despite far worse symmetry. It is therefore, difficult to quantify the contribution to the degradation of compression due to each of these effects, from this set of simulations.

2.4.2 Time Resolved Asymmetry Growth

The time-resolved, $\ell = 10$ mode growth of the fuel density from the $R_b/R_t = 0.8$, 0.9 and 1.0, with-CBET simulations are examined more closely in this section in order to understand the non-monotonic behaviour of the CBET, fuel-symmetry curve from Fig. 2.13.a. These simulations were chosen as they are the local minima and maxima of the curve and therefore should most clearly display the important behaviour. Fig. 2.14.a plots the $\ell = 10$ growth of $\rho_{DT}R$ for each of these simulations. Note that all bangtimes were approximately $t = 2.5$ ns, so the value at this time is the $\ell = 10$ at stagnation. The $\ell = 10$ growth of $P_{dep}R$ for these simulations is plotted in Fig. 2.14.b, which are the same as the curves from the right panels of Fig. 2.10, but are plotted again here for direct comparison with the $\rho_{DT}R$ values. The mode-flips are clearly identifiable in this plot as sharp falls and rises in the $\ell = 10$, which corresponds to an inversion of deposition asymmetry.

Firstly, the growth of the fuel density asymmetry from the $R_b/R_t = 0.8$ simulation shall be studied. It can be seen from the green curve in Fig. 2.14.a, that the growth of this mode is slow from $t \sim 0.5 \rightarrow 1.4$ ns, compared to the $R_b/R_t = 0.9$ and $R_b/R_t = 1.0$ simulations. This is explained due to the low deposition asymmetry in Fig. 2.14.b which is ultimately responsible for imprinting the asymmetry on the hydrodynamics. As was seen from the time-resolved, radially integrated deposition in Fig. 2.10.a, this low asymmetry of the deposition is due to the developing mode-flip. In this simulation, the developing mode-flip at this time ultimately reduces deposition asymmetry, because the beam is not wide enough for the target convergence to truly flip the deposition. Although the $\ell = 10$ of the $\rho_{DT}R$ starts to grow again after the second mode-flip at $t \sim 1.2$ ns, the long period of highly symmetric deposition means that the stagnation state is ultimately relatively symmetric, compared to higher and lower beam radii simulations.

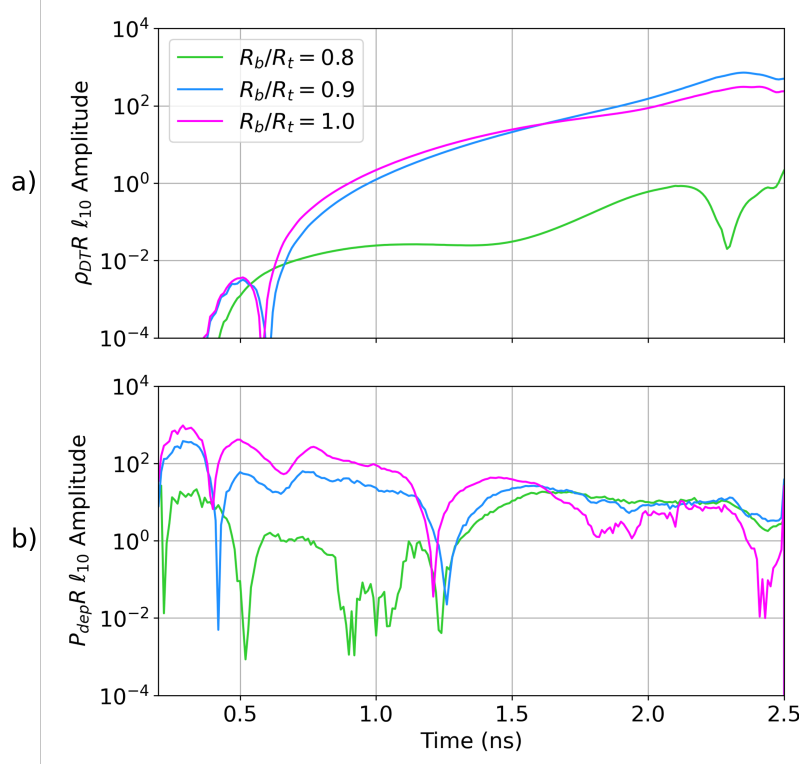


Figure 2.14: Time resolved $\ell = 10$ Fourier power spectrum amplitude for a) $\rho_{DT}R$ and b) $P_{dep}R$ for CBET simulations with 3 R_b/R_t values. The developing, but unrealised, modal-flip for $R_b/R_t = 0.8$ from $t \sim 0.5 \rightarrow 1.2$ ns reduces the $P_{dep}R_{\ell=10}$, leading to slow $\rho_{DT}R_{\ell=10}$ growth and ultimately a relatively symmetric stagnation state. Despite large values of $\rho_{DT}R_{\ell=10}$ initially, the developing modal flip of the $R_b/R_t = 1.0$ simulation from $t \sim 1.8 \rightarrow 2.1$ ns slows the density asymmetry growth.

Comparison of the growth between the $R_b/R_t = 0.9$ and 1.0 simulations is slightly more nuanced. As is seen in the radially integrated power deposition from Figs. 2.10.c and 2.10.e, the mode-flip at $t \sim 0.5$ ns develops into a full inversion of the deposition asymmetry. Because the beams are wider in the $R_b/R_t = 1.0$ simulation, more light wraps around the target. This leads to stronger caustic fields, more CBET and therefore greater distortion of the inbound field profiles. Thus, the $R_b/R_t = 1.0$ has a less symmetric deposition profile than the narrower beam case, until the next mode-flip occurs at $t \sim 1.2$ ns. This explains why the $\ell = 10$ of the $\rho_{DT}R$ is larger for the $R_b/R_t = 1.0$ simulation up until $t \sim 1.5$ ns.

This remains the case, until the wider beam of the $R_b/R_t = 1.0$ case, begins to wrap around the target sufficiently, to begin the development of an additional mode-flip of the deposition at $t \sim 1.6$ ns. Similar to the $R_b/R_t = 0.8$ case from $\sim 0.5 \rightarrow 1.2$ ns, the development of a flip in the deposition profile acts simply to reduce the deposition asymmetry, since the beam is not sufficiently wide. Therefore, the deposition asymmetry of $R_b/R_t = 1.0$ from $\sim 1.6 \rightarrow 2.1$ ns is reduced compared to the $R_b/R_t = 0.9$ simulation, for which the beams are not wide enough to develop another mode-flip. The reduction of deposition asymmetry is again clearly visible by comparing Figs. 2.10.c ($R_b/R_t = 0.9$) and 2.10.e ($R_b/R_t = 1.0$) from $\sim 1.6 \rightarrow 2.1$ ns. More

symmetric deposition during this period reduces the rate of $\rho_{DT}R$ asymmetry growth. This results in a less symmetric $R_b/R_t = 0.9$ stagnation state, as this simulation does have experience the same disruption to the deposition asymmetry source. For $R_b/R_t > 1.0$, the beams are wide enough that the mode-flip at $t \sim 1.6$ ns does lead to a full inversion of the deposition asymmetry and therefore the $\ell = 10$ of the $P_{dep}R$ is not reduced in the same manner for even wider beams. Ultimately this leads to increasing asymmetry of the stagnation state at $R_b/R_t > 1.0$, as is observed in Fig. 2.13.a.

While this analysis does explain the trend observed in Fig. 2.13.a, subtleties exist which are not explicitly addressed, but could offer additional insight to the growth of stagnation state asymmetries in direct-drive implosions. For example, the deposition all occurs below the critical density, which is separated from the ablation surface by a finite stand-off distance. Thus the energy must be transported from the absorption region to the ablation surface by thermal conduction. This leads to a time-lag for asymmetry in Fig. 2.14.b (deposition) to propagate through to the curves in Fig. 2.14.a (fuel density). Changing coronal plasma conditions during the implosion will also change this time-lag in a non-obvious way. For example, early in the implosions, deposition occurs exclusively in the outermost CH material. As time progresses, the CH expands away and the ablation surface changes from CH to the DT layer. Even later, (at $t \sim 2.1$ ns in these simulations), the critical surface moves from CH into DT. All of these changes in coronal and transport layer conditions will impact how conduction propagates asymmetry from the deposition to the fuel, *i.e.* there is additional complexity in mapping from $P_{dep}R$ asymmetry to $\rho_{DT}R$ asymmetry. Future work could perhaps investigate this further, by also comparing the heat flux just above the ablation surface, which may further elucidate the important physics.

2.4.3 Comparison of Results to Statistical Modelling

Ultimately, this work was conducted to try and explain why statistical modelling of OMEGA implosions, demonstrates that distinct regimes exist in the R_b/R_t degradation of implosions from 1-D calculations, *i.e.* to explain the shape of the curve in Fig. 2.3. The fit to the experimental scatter plot has a transition at $R_{b/t}^{\text{crit}} = 0.86$, after which, improvement of the yield for increasing R_b/R_t slows. Neither 1-D codes which include CBET models, or 3-D codes without CBET are able to reproduce this trend, which means that multidimensional effects, seeded by CBET are considered a likely explanation [92]. The work conducted in this chapter is not directly comparable to these plots because a 1-D tuning process was conducted to ensure that all implosions had the same coupled energy. This was to prevent having to perform a far more in depth optimisation procedure for both the pulse and target simultaneously. Therefore, changes in the 1-D effects of CBET at different R_b/R_t are not included in these simulations (changes to magnitude of deposited energy), only the redistribution of deposited energy due to CBET, *i.e.* how CBET alters asymmetry. The differences in cylindrical and spherical geometry also complicate direct comparison between results due to different coronal plasma profiles and convergence properties. For example, the R_b/R_t values of transitions in behaviour would not be expected to be the same between geometries.

Despite this, the asymmetry and compression metrics in Figs. 2.13.a and 2.13.b respectively, clearly demonstrate relatively sharp transitions in behaviour. For example, asymmetry and compression both get worse from $R_b/R_t = 0.8 \rightarrow 0.9$, but improve from $0.9 \rightarrow 1.0$. If this behaviour was also observed in spherical geometry simulations, which is due to CBET introducing mode-flips in the deposited power, it potentially be the cause of the experimental data transition at $R_{b/t}^{\text{crit}} = 0.86$. Explicitly, if CBET acted to degrade deposition symmetry in spherical implosions from $R_b/R_t = 0.86 \rightarrow 1.00$, this would slow the rate of improvement in the yield over clean metric, plotted in Fig. 2.3. While this is not at all a conclusive explanation of the behaviour in the statistical model, results from these simulations do not seem to rule it out. It therefore offers motivation for extending the simulation platform to a spherical geometry and including 1-D effects of CBET in R_b/R_t trends by changing the target and fixing the total incident laser energy. This should conclusively demonstrate that shape degradation due to CBET either is or is not responsible for the transitions.

2.5 Conclusions

2.5.1 Summary of work

This chapter has described the development of a novel, 2-D cylindrical simulation platform to study direct-drive implosion physics, and its use to investigate how altering R_b/R_t changes the stagnation symmetry both with, and without the effects of CBET. The work was conducted to test the hypothesis that changes to stagnation state symmetry due to changing CBET action at different R_b/R_t was responsible for unexplained behaviour in statistical modelling of OMEGA experiments. In order to avoid performing an in-depth optimisation process, where the target and pulse were simultaneously varied, only the incident laser energy was varied, to fix the coupled energy to the target. Therefore, only the changes to deposition symmetry due to CBET were studied at different R_b/R_t . This 1-D tuning procedure yielded 8 implosions both with and without CBET effects.

By conducting 2-D simulations with the initial conditions obtained from the tuning, interesting behaviour was observed for both the CBET and no-CBET cases. In both cases, mode-flips of the deposition were observed, due to different effects. For no-CBET, these mode flips occurred due to increasing plasma scale lengths, which shifted maximum deposition from beam angles to the overlap region between beams. When including CBET, this scale-length behaviour was obscured by much more dominant mode-flips, which were induced due to caustic CBET interactions distorting the incident field profiles of beams.

Without CBET changes to deposition uniformity, the stagnation state asymmetry decreased with increasing R_b/R_t as more beam overlap led to increasingly uniform target illumination. When CBET was included however, increasing CBET with wider beam radii resulted in less and less symmetric deposition, which broadly led to increasing asymmetry with R_b/R_t . The precise behaviour was, however, non-monotonic due to CBET mode-flips increasing the symmetry of illumination at specific R_b/R_t values. This led to distinct transitions regions in the trends of symmetry and compression, plotted against R_b/R_t , which were identified as

a potential explanation of the transitions observed in OMEGA statistical modelling. Further work must however be conducted to obtain direct comparison to the statistical model and thus conclusively state whether CBET asymmetries are, or are not the cause.

2.5.2 Future Work

There are many ways that the work presented in this chapter could be extended, the simulation platform improved to better reflect reality, or additional physics studied on the existing platform. One interesting way to extend the analysis of the work would be to investigate how heat transport affects the conversion of deposition asymmetries into hydrodynamic perturbations. As was discussed at the end of Sec. 2.4.2, there is a lag in the conversion due to thermal conduction taking this information inward via a finite transport region. The transport region would also vary throughout the implosion as the hydrodynamic profiles evolve and the material changes from CH to DT. By including analysis of heat flux, the way that this information is propagated could be studied. Furthermore, a model for non-local heat-flow could be incorporated into CHIMERA, such as SNB [112–114] or FAST-VFP [115]. Due to the strong temperature gradients in the transport layer, non-local effects could significantly affect how this information is propagated to the ablation surface and thus imprints on the hydrodynamics.

The geometry of the platform could also be modified to allow for spherical rather than cylindrical convergence. This would allow for better comparison between simulation results and spherical implosion experiments. Cylindrical geometry leads to greater target convergence for a given incident energy and also less divergence of the outflowing, coronal plasma, thus yielding higher coronal plasma densities for a given ablation velocity. By simulating a thin, equatorial ‘slice’ of a spherical domain, *i.e.* a spherical simulation with bounds $\phi \in [-\pi, \pi]$ and $\theta \in [\lesssim \pi/2, \gtrsim \pi/2]$, a 2-D ray-trace could still be conducted so simulation run-times should be very similar to the cylindrical case. This was not done for the work in this chapter because the SOLAS 2-D ray-trace assumes that the simulation occurs in a plane, and the spherical ‘slice’ is not a plane. Minor development for this specific case could rectify this however and enable similar simulations in spherical geometry.

Similar initial conditions could also be used to study further multidimensional direct-drive physics, without the need to conduct, an expensive, full 3-D ray-trace. For example, laser imprint is a significant issue in direct-drive and means that implosions must be conducted at a high adiabat for optimal yields [116]. This limits the compressibility and therefore maximum performance of ICF experiments [117, 118]. Improved understanding of laser imprint requires high resolution simulations, due to the small spatial scale of the intensity modulations. Typically, high resolution, 2-D, $r - z$ simulations with a 3-D laser ray-trace [119], or lower resolution, fully 3-D simulations [120] are conducted to study the effect of imprint. 2-D $r - z$ Rad-Hydro simulations with a 3-D laser ray-trace average the deposition from the 3-D ray-trace around the azimuthal angle, and therefore artificially smooth out the imprint modulation to power deposition. While 3-D simulations at a sufficiently high resolution should resolve the imprint seed properly, these are extremely expensive to perform, particularly for

the fixed angular resolution, Eulerian code ASTER which is typically used for these problems. By performing a spherical or cylindrical ‘slice’ simulation with an imprint model, the seed and the growth of imprint induced instabilities could be consistently modelled at high resolutions, providing a complimentary study to the existing literature. This setup would not include out-of-plane stabilisation flows however, and could therefore overestimate growth of these small modes.

Appendices

A Numerics Appendices

Bibliography

- [1] Dhrumir Patel, Riccardo Betti, Varchas Gopalaswamy, and Ka Ming Woo. Novel double-spike pulse shape for OMEGA cryogenic implosions. 2018:GO6.006, January 2018. URL <https://ui.adsabs.harvard.edu/abs/2018APS..DPPG06006P>. Conference Name: APS Division of Plasma Physics Meeting Abstracts ADS Bibcode: 2018APS..DPPG06006P. 7, 62
- [2] D. Cao, R. C. Shah, S. P. Regan, R. Epstein, I. V. Igumenshchev, V. Gopalaswamy, A. R. Christopherson, W. Theobald, P. B. Radha, and V. N. Goncharov. Interpreting the electron temperature inferred from x-ray continuum emission for direct-drive inertial confinement fusion implosions on OMEGA. *Physics of Plasmas*, 26(8):082709, August 2019. ISSN 1070-664X, 1089-7674. doi: 10.1063/1.5112759. URL <https://pubs.aip.org/pop/article/26/8/082709/632047/Interpreting-the-electron-temperature-inferred>.
- [3] A. J. Crilly, B. D. Appelbe, O. M. Mannion, C. J. Forrest, V. Gopalaswamy, C. A. Walsh, and J. P. Chittenden. Neutron backscatter edge: A measure of the hydrodynamic properties of the dense DT fuel at stagnation in ICF experiments. *Physics of Plasmas*, 27(1):012701, January 2020. ISSN 1070-664X, 1089-7674. doi: 10.1063/1.5128830. URL <https://pubs.aip.org/pop/article/27/1/012701/262967/Neutron-backscatter-edge-A-measure-of-the>. 7, 62
- [4] D. H. Froula, I. V. Igumenshchev, D. T. Michel, D. H. Edgell, R. Follett, V. Yu. Glebov, V. N. Goncharov, J. Kwiatkowski, F. J. Marshall, P. B. Radha, W. Seka, C. Sorce, S. Stagnitto, C. Stoeckl, and T. C. Sangster. Increasing Hydrodynamic Efficiency by Reducing Cross-Beam Energy Transfer in Direct-Drive-Implosion Experiments. *Physical Review Letters*, 108(12):125003, March 2012. ISSN 0031-9007, 1079-7114. doi: 10.1103/PhysRevLett.108.125003. URL <https://link.aps.org/doi/10.1103/PhysRevLett.108.125003>. 12, 70, 71, 72, 73
- [5] A. Lees, R. Betti, J. P. Knauer, V. Gopalaswamy, D. Patel, K. M. Woo, K. S. Anderson, E. M. Campbell, D. Cao, J. Carroll-Nellenback, R. Epstein, C. J. Forrest, V. N. Goncharov, D. R. Harding, S. X. Hu, I. V. Igumenshchev, R. T. Janezic, O. M. Mannion, P. B. Radha, S. P. Regan, A. Shvydky, R. C. Shah, W. T. Shmayda, C. Stoeckl, W. Theobald, and C. A. Thomas. Understanding the fusion yield dependencies in OMEGA DT-layered implosion experiments using a physics-based statistical mapping model. *Physics of Plasmas*, 30(1):012709, January 2023. ISSN 1070-664X, 1089-7674.

- doi: 10.1063/5.0106515. URL <https://pubs.aip.org/pop/article/30/1/012709/2867741/Understanding-the-fusion-yield-dependencies-in>. 12, 72, 74, 75, 76
- [6] P. Tzeferacos, A. Rigby, A. F. A. Bott, A. R. Bell, R. Bingham, A. Casner, F. Cattaneo, E. M. Churazov, J. Emig, F. Fiuzza, C. B. Forest, J. Foster, C. Graziani, J. Katz, M. Koenig, C.-K. Li, J. Meinecke, R. Petrasso, H.-S. Park, B. A. Remington, J. S. Ross, D. Ryu, D. Ryutov, T. G. White, B. Reville, F. Miniati, A. A. Schekochihin, D. Q. Lamb, D. H. Froula, and G. Gregori. Laboratory evidence of dynamo amplification of magnetic fields in a turbulent plasma. *Nature Communications*, 9(1):591, February 2018. ISSN 2041-1723. doi: 10.1038/s41467-018-02953-2. URL <https://www.nature.com/articles/s41467-018-02953-2>. 17
- [7] F. Fiuzza, G. F. Swadling, A. Grassi, H. G. Rinderknecht, D. P. Higginson, D. D. Ryutov, C. Bruulsema, R. P. Drake, S. Funk, S. Glenzer, G. Gregori, C. K. Li, B. B. Pollock, B. A. Remington, J. S. Ross, W. Rozmus, Y. Sakawa, A. Spitkovsky, S. Wilks, and H.-S. Park. Electron acceleration in laboratory-produced turbulent collisionless shocks. *Nature Physics*, 16(9):916–920, September 2020. ISSN 1745-2481. doi: 10.1038/s41567-020-0919-4. URL <https://www.nature.com/articles/s41567-020-0919-4>. Publisher: Nature Publishing Group.
- [8] Jena Meinecke, Petros Tzeferacos, James S. Ross, Archie F. A. Bott, Scott Feister, Hye-Sook Park, Anthony R. Bell, Roger Blandford, Richard L. Berger, Robert Bingham, Alexis Casner, Laura E. Chen, John Foster, Dustin H. Froula, Clement Goyon, Daniel Kalantar, Michel Koenig, Brandon Lahmann, Chikang Li, Yingchao Lu, Charlotte A. J. Palmer, Richard D. Petrasso, Hannah Poole, Bruce Remington, Brian Reville, Adam Reyes, Alexandra Rigby, Dongsu Ryu, George Swadling, Alex Zylstra, Francesco Miniati, Subir Sarkar, Alexander A. Schekochihin, Donald Q. Lamb, and Gianluca Gregori. Strong suppression of heat conduction in a laboratory replica of galaxy-cluster turbulent plasmas. *Science Advances*, 8(10):eabj6799, March 2022. ISSN 2375-2548. doi: 10.1126/sciadv.abj6799. URL <https://www.science.org/doi/10.1126/sciadv.abj6799>. 17
- [9] Andrea L. Kritcher, Damian C. Swift, Tilo Döppner, Benjamin Bachmann, Lorin X. Benedict, Gilbert W. Collins, Jonathan L. DuBois, Fred Elsner, Gilles Fontaine, Jim A. Gaffney, Sébastien Hamel, Amy Lazicki, Walter R. Johnson, Natalie Kostinski, Dominik Kraus, Michael J. MacDonald, Brian Maddox, Madison E. Martin, Paul Neu-mayer, Abbas Nikroo, Joseph Nilsen, Bruce A. Remington, Didier Saumon, Phillip A. Sterne, Wendi Sweet, Alfredo A. Correa, Heather D. Whitley, Roger W. Falcone, and Siegfried H. Glenzer. A measurement of the equation of state of carbon envelopes of white dwarfs. *Nature*, 584(7819):51–54, August 2020. ISSN 0028-0836, 1476-4687. doi: 10.1038/s41586-020-2535-y. URL <https://www.nature.com/articles/s41586-020-2535-y>. 17
- [10] R. F. Smith, J. H. Eggert, R. Jeanloz, T. S. Duffy, D. G. Braun, J. R. Patterson, R. E. Rudd,

- J. Biener, A. E. Lazicki, A. V. Hamza, J. Wang, T. Braun, L. X. Benedict, P. M. Celliers, and G. W. Collins. Ramp compression of diamond to five terapascals. *Nature*, 511(7509):330–333, July 2014. ISSN 1476-4687. doi: 10.1038/nature13526. URL <https://www.nature.com/articles/nature13526>. Publisher: Nature Publishing Group. 17
- [11] A. B. Zylstra, O. A. Hurricane, D. A. Callahan, A. L. Kritch, J. E. Ralph, H. F. Robey, J. S. Ross, C. V. Young, K. L. Baker, D. T. Casey, T. Döppner, L. Divol, M. Hohenberger, S. Le Pape, A. Pak, P. K. Patel, R. Tommasini, S. J. Ali, P. A. Amendt, L. J. Atherton, B. Bachmann, D. Bailey, L. R. Benedetti, L. Berzak Hopkins, R. Betti, S. D. Bhandarkar, J. Biener, R. M. Bionta, N. W. Birge, E. J. Bond, D. K. Bradley, T. Braun, T. M. Briggs, M. W. Bruhn, P. M. Celliers, B. Chang, T. Chapman, H. Chen, C. Choate, A. R. Christopherson, D. S. Clark, J. W. Crippen, E. L. Dewald, T. R. Dittrich, M. J. Edwards, W. A. Farmer, J. E. Field, D. Fittinghoff, J. Frenje, J. Gaffney, M. Gatu Johnson, S. H. Glenzer, G. P. Grim, S. Haan, K. D. Hahn, G. N. Hall, B. A. Hammel, J. Harte, E. Hartouni, J. E. Heebner, V. J. Hernandez, H. Herrmann, M. C. Herrmann, D. E. Hinkel, D. D. Ho, J. P. Holder, W. W. Hsing, H. Huang, K. D. Humbird, N. Izumi, L. C. Jarrott, J. Jeet, O. Jones, G. D. Kerbel, S. M. Kerr, S. F. Khan, J. Kilkenny, Y. Kim, H. Geppert Kleinrath, V. Geppert Kleinrath, C. Kong, J. M. Koning, J. J. Kroll, M. K. G. Kruse, B. Kustowski, O. L. Landen, S. Langer, D. Larson, N. C. Lemos, J. D. Lindl, T. Ma, M. J. MacDonald, B. J. MacGowan, A. J. Mackinnon, S. A. MacLaren, A. G. MacPhee, M. M. Marinak, D. A. Mariscal, E. V. Marley, L. Masse, K. Meaney, N. B. Meezan, P. A. Michel, M. Millot, J. L. Milovich, J. D. Moody, A. S. Moore, J. W. Morton, T. Murphy, K. Newman, J.-M. G. Di Nicola, A. Nikroo, R. Nora, M. V. Patel, L. J. Pelz, J. L. Peterson, Y. Ping, B. B. Pollock, M. Ratledge, N. G. Rice, H. Rinderknecht, M. Rosen, M. S. Rubery, J. D. Salmonson, J. Sater, S. Schiaffino, D. J. Schlossberg, M. B. Schneider, C. R. Schroeder, H. A. Scott, S. M. Sepke, K. Sequoia, M. W. Sherlock, S. Shin, V. A. Smalyuk, B. K. Spears, P. T. Springer, M. Stadermann, S. Stoupin, D. J. Strozzi, L. J. Suter, C. A. Thomas, R. P. J. Town, E. R. Tubman, C. Trosseille, P. L. Volegov, C. R. Weber, K. Widmann, C. Wild, C. H. Wilde, B. M. Van Wonterghem, D. T. Woods, B. N. Woodworth, M. Yamaguchi, S. T. Yang, and G. B. Zimmerman. Burning plasma achieved in inertial fusion. *Nature*, 601(7894):542–548, January 2022. ISSN 1476-4687. doi: 10.1038/s41586-021-04281-w. URL <https://www.nature.com/articles/s41586-021-04281-w>. Publisher: Nature Publishing Group. 17
- [12] Stephen A. Slutz and Roger A. Vesey. High-Gain Magnetized Inertial Fusion. *Physical Review Letters*, 108(2):025003, January 2012. ISSN 0031-9007, 1079-7114. doi: 10.1103/PhysRevLett.108.025003. URL <https://link.aps.org/doi/10.1103/PhysRevLett.108.025003>.
- [13] C. A. Williams, R. Betti, V. Gopalaswamy, J. P. Knauer, C. J. Forrest, A. Lees, R. Ejaz, P. S. Farmakis, D. Cao, P. B. Radha, K. S. Anderson, S. P. Regan, V. Yu Glebov, R. C. Shah, C. Stoeckl, S. Ivancic, K. Churnetski, R. T. Janezic, C. Fella, M. J. Rosenberg, M. J.

- Bonino, D. R. Harding, W. T. Shmayda, J. Carroll-Nellenback, S. X. Hu, R. Epstein, T. J. B. Collins, C. A. Thomas, I. V. Igumenshchev, V. N. Goncharov, W. Theobald, K. M. Woo, J. A. Marozas, K. A. Bauer, S. Sampat, L. J. Waxer, D. Turnbull, P. V. Heuer, H. McClow, L. Ceurnvorst, W. Scullin, D. H. Edgell, M. Koch, D. Bredesen, M. Gatu Johnson, J. A. Frenje, R. D. Petrasso, C. Shuldborg, M. Farrell, J. Murray, D. Guzman, B. Serrato, S. F. B. Morse, M. Labuzeta, C. Deeney, and E. M. Campbell. Demonstration of hot-spot fuel gain exceeding unity in direct-drive inertial confinement fusion implosions. *Nature Physics*, 20(5):758–764, May 2024. ISSN 1745-2481. doi: 10.1038/s41567-023-02363-2. URL <https://www.nature.com/articles/s41567-023-02363-2>. Publisher: Nature Publishing Group. 17
- [14] K. L. Nguyen, L. Yin, B. J. Albright, A. M. Hansen, D. H. Froula, D. Turnbull, R. K. Follett, and J. P. Palastro. Cross-beam energy transfer saturation by ion trapping-induced detuning. *Physics of Plasmas*, 28(8):082705, August 2021. ISSN 1070-664X, 1089-7674. doi: 10.1063/5.0054008. URL <https://pubs.aip.org/aip/pop/article/106807>. 17, 21
- [15] J. F. Myatt, R. K. Follett, J. G. Shaw, D. H. Edgell, D. H. Froula, I. V. Igumenshchev, and V. N. Goncharov. A wave-based model for cross-beam energy transfer in direct-drive inertial confinement fusion. *Physics of Plasmas*, 24(5):056308, April 2017. ISSN 1070-664X. doi: 10.1063/1.4982059. URL <https://doi.org/10.1063/1.4982059>. 17, 20, 45
- [16] Andrew J. Schmitt and Stephen P. Obenschain. The importance of laser wavelength for driving inertial confinement fusion targets. I. Basic physics. *Physics of Plasmas*, 30(1):012701, January 2023. ISSN 1070-664X, 1089-7674. doi: 10.1063/5.0118080. URL <https://pubs.aip.org/pop/article/30/1/012701/2867678/The-importance-of-laser-wavelength-for-driving>. 17
- [17] Andrew J. Schmitt and Stephen P. Obenschain. The importance of laser wavelength for driving inertial confinement fusion targets. II. Target design. *Physics of Plasmas*, 30(1):012702, January 2023. ISSN 1070-664X. doi: 10.1063/5.0118093. URL <https://doi.org/10.1063/5.0118093>. 17
- [18] J Huba, D. NRL Plasma Formulary. Technical Report NRL/PU/6790-13-589, Naval Research Laboratory, Washington, DC, 2013. 17
- [19] Tudor Wyatt Johnston and John M. Dawson. Correct values for high-frequency power absorption by inverse bremsstrahlung in plasmas. *Physics of Fluids*, 16:722–722, May 1973. ISSN 0899-82131070-6631. doi: 10.1063/1.1694419. URL <https://ui.adsabs.harvard.edu/abs/1973PhFl...16..722J>. Publisher: AIP ADS Bibcode: 1973PhFl...16..722J. 17
- [20] A. Colaïtis, I. Igumenshchev, J. Mathiaud, and V. Goncharov. Inverse ray tracing on icosahedral tetrahedron grids for non-linear laser plasma interaction coupled to

- 3D radiation hydrodynamics. *Journal of Computational Physics*, 443:110537, October 2021. ISSN 0021-9991. doi: 10.1016/j.jcp.2021.110537. URL <https://www.sciencedirect.com/science/article/pii/S0021999121004320>. 17, 19, 28, 29, 39, 66
- [21] C. J. Randall, James R. Albritton, and J. J. Thomson. Theory and simulation of stimulated Brillouin scatter excited by nonabsorbed light in laser fusion systems. *The Physics of Fluids*, 24(8):1474–1484, August 1981. ISSN 0031-9171. doi: 10.1063/1.863551. URL <https://doi.org/10.1063/1.863551>. 17, 45, 47
- [22] A. Colaïtis, G. Duchateau, P. Nicolaï, and V. Tikhonchuk. Towards modeling of nonlinear laser-plasma interactions with hydrocodes: The thick-ray approach. *Physical Review E*, 89(3):033101, March 2014. doi: 10.1103/PhysRevE.89.033101. URL <https://link.aps.org/doi/10.1103/PhysRevE.89.033101>. Publisher: American Physical Society. 18, 20
- [23] R. W. Paddock, H. Martin, R. T. Ruskov, R. H. H. Scott, W. Garbett, B. M. Haines, A. B. Zylstra, R. Aboushelbaya, M. W. Mayr, B. T. Spiers, R. H. W. Wang, and P. A. Norreys. One-dimensional hydrodynamic simulations of low convergence ratio direct-drive inertial confinement fusion implosions. *Philosophical Transactions of the Royal Society A: Mathematical, Physical and Engineering Sciences*, 379(2189):20200224, January 2021. ISSN 1364-503X, 1471-2962. doi: 10.1098/rsta.2020.0224. URL <https://royalsocietypublishing.org/doi/10.1098/rsta.2020.0224>. 18
- [24] A. Colaïtis, J. P. Palastro, R. K. Follett, I. V. Igumenschev, and V. Goncharov. Real and complex valued geometrical optics inverse ray-tracing for inline field calculations. *Physics of Plasmas*, 26(3):032301, March 2019. ISSN 1070-664X, 1089-7674. doi: 10.1063/1.5082951. URL <https://pubs.aip.org/pop/article/26/3/032301/699557/Real-and-complex-valued-geometrical-optics-inverse>. 18, 40, 41, 43
- [25] A. Colaïtis, R. K. Follett, J. P. Palastro, I. Igumenschev, and V. Goncharov. Adaptive inverse ray-tracing for accurate and efficient modeling of cross beam energy transfer in hydrodynamics simulations. *Physics of Plasmas*, 26(7):072706, July 2019. ISSN 1070-664X, 1089-7674. doi: 10.1063/1.5108777. URL <https://pubs.aip.org/pop/article/26/7/072706/1060189/Adaptive-inverse-ray-tracing-for-accurate-and>. 18, 40, 86
- [26] D. J. Strozzi, D. S. Bailey, P. Michel, L. Divol, S. M. Sepke, G. D. Kerbel, C. A. Thomas, J. E. Ralph, J. D. Moody, and M. B. Schneider. Interplay of Laser-Plasma Interactions and Inertial Fusion Hydrodynamics. *Physical Review Letters*, 118(2):025002, January 2017. ISSN 0031-9007, 1079-7114. doi: 10.1103/PhysRevLett.118.025002. URL <https://link.aps.org/doi/10.1103/PhysRevLett.118.025002>. 19
- [27] S. Liberatore, P. Gauthier, J. L. Willien, P. E. Masson-Labordre, F. Philippe, O. Poujade, E. Alozy, R. Botrel, G. Boutoux, J. Bray, T. Caillaud, C. Chicanne, C. Chollet, A. De-

- bayle, S. Depierreux, W. Duchastenier, M. Ferri, O. Henry, P. Hoch, S. Laffite, O. Landoas, L. Le-Deroff, E. Lefebvre, G. Legay, I. Marmajou, C. Meyer, K. Molina, O. Morice, E. Peche, P. Prunet, R. Riquier, R. Rosch, V. Tassin, X. Vaisseau, and B. Villette. First indirect drive inertial confinement fusion campaign at Laser Megajoule. *Physics of Plasmas*, 30(12):122707, December 2023. ISSN 1070-664X, 1089-7674. doi: 10.1063/5.0176446. URL <https://pubs.aip.org/pop/article/30/12/122707/2930727/First-indirect-drive-inertial-confinement-fusion>. 19
- [28] J. A. Marozas, M. Hohenberger, M. J. Rosenberg, D. Turnbull, T. J. B. Collins, P. B. Radha, P. W. McKenty, J. D. Zuegel, F. J. Marshall, S. P. Regan, T. C. Sangster, W. Seka, E. M. Campbell, V. N. Goncharov, M. W. Bowers, J.-M. G. Di Nicola, G. Erbert, B. J. MacGowan, L. J. Pelz, J. Moody, and S. T. Yang. Wavelength-detuning cross-beam energy transfer mitigation scheme for direct drive: Modeling and evidence from National Ignition Facility implosions. *Physics of Plasmas*, 25(5):056314, May 2018. ISSN 1070-664X, 1089-7674. doi: 10.1063/1.5022181. URL <https://pubs.aip.org/pop/article/25/5/056314/1061159/Wavelength-detuning-cross-beam-energy-transfer>. 19, 28, 29, 30, 46
- [29] A. Debayle, C. Ruyer, O. Morice, P.-E. Masson-Laborde, P. Loiseau, and D. Benisti. A unified modeling of wave mixing processes with the ray tracing method. *Physics of Plasmas*, 26(9):092705, September 2019. ISSN 1070-664X, 1089-7674. doi: 10.1063/1.5110247. URL <https://pubs.aip.org/pop/article/26/9/092705/263616/A-unified-modeling-of-wave-mixing-processes-with>. 19
- [30] A. Colaïtis, S. Hüller, D. Pesme, G. Duchateau, and V. T. Tikhonchuk. Crossed beam energy transfer: Assessment of the paraxial complex geometrical optics approach versus a time-dependent paraxial method to describe experimental results. *Physics of Plasmas*, 23(3):032118, March 2016. ISSN 1070-664X, 1089-7674. doi: 10.1063/1.4944496. URL <https://pubs.aip.org/pop/article/23/3/032118/1016773/Crossed-beam-energy-transfer-Assessment-of-the>. 20
- [31] A. Colaïtis, G. Duchateau, X. Ribeyre, and V. Tikhonchuk. Modeling of the cross-beam energy transfer with realistic inertial-confinement-fusion beams in a large-scale hydrocode. *Physical Review E*, 91(1):013102, January 2015. ISSN 1539-3755, 1550-2376. doi: 10.1103/PhysRevE.91.013102. URL <https://link.aps.org/doi/10.1103/PhysRevE.91.013102>. 20
- [32] D. H. Edgell, R. K. Follett, I. V. Igumenshchev, J. F. Myatt, J. G. Shaw, and D. H. Froula. Mitigation of cross-beam energy transfer in symmetric implosions on OMEGA using wavelength detuning. *Physics of Plasmas*, 24(6):062706, June 2017. ISSN 1070-664X, 1089-7674. doi: 10.1063/1.4985315. URL <https://pubs.aip.org/aip/pop/article/108749>. 20, 66
- [33] R. K. Follett, J. G. Shaw, J. F. Myatt, V. N. Goncharov, D. H. Edgell, D. H. Froula, and J. P. Palastro. Ray-based modeling of cross-beam energy transfer at caustics.

- [Physical Review E](#), 98(4):043202, October 2018. ISSN 2470-0045, 2470-0053. doi: 10.1103/PhysRevE.98.043202. URL <https://link.aps.org/doi/10.1103/PhysRevE.98.043202>. 20, 40, 49, 50
- [34] R. K. Follett, A. Colaïtis, D. Turnbull, D. H. Froula, and J. P. Palastro. Validation of ray-based cross-beam energy transfer models. [Physics of Plasmas](#), 29(11):113902, November 2022. ISSN 1070-664X, 1089-7674. doi: 10.1063/5.0123462. URL <https://pubs.aip.org/pop/article/29/11/113902/2844248/Validation-of-ray-based-cross-beam-energy-transfer>. 20, 35, 36, 39, 40, 41, 48, 55, 56, 58, 59, 78
- [35] I. V. Igumenshchev, D. H. Edgell, V. N. Goncharov, J. A. Delettrez, A. V. Maximov, J. F. Myatt, W. Seka, A. Shvydky, S. Skupsky, and C. Stoeckl. Crossed-beam energy transfer in implosion experiments on OMEGA. [Physics of Plasmas](#), 17(12):122708, December 2010. ISSN 1070-664X, 1089-7674. doi: 10.1063/1.3532817. URL <https://pubs.aip.org/pop/article/17/12/122708/918785/Crossed-beam-energy-transfer-in-implosion>. 20
- [36] I. V. Igumenshchev, W. Seka, D. H. Edgell, D. T. Michel, D. H. Froula, V. N. Goncharov, R. S. Craxton, L. Divol, R. Epstein, R. Follett, J. H. Kelly, T. Z. Kosc, A. V. Maximov, R. L. McCrory, D. D. Meyerhofer, P. Michel, J. F. Myatt, T. C. Sangster, A. Shvydky, S. Skupsky, and C. Stoeckl. Crossed-beam energy transfer in direct-drive implosions. [Physics of Plasmas](#), 19(5):056314, May 2012. ISSN 1070-664X, 1089-7674. doi: 10.1063/1.4718594. URL <https://pubs.aip.org/pop/article/19/5/056314/596972/Crossed-beam-energy-transfer-in-direct-drive>. 20, 40, 73
- [37] Jason F. Myatt, John G. Shaw, Russell K. Follett, Dana H. Edgell, Dustin H. Froula, John P. Palastro, and Valeri N. Goncharov. LPSE: A 3-D wave-based model of cross-beam energy transfer in laser-irradiated plasmas. [Journal of Computational Physics](#), 399:108916, December 2019. ISSN 00219991. doi: 10.1016/j.jcp.2019.108916. URL <https://linkinghub.elsevier.com/retrieve/pii/S0021999119306217>. 20
- [38] R. K. Follett, J. G. Shaw, J. F. Myatt, H. Wen, D. H. Froula, and J. P. Palastro. Thresholds of absolute two-plasmon-decay and stimulated Raman scattering instabilities driven by multiple broadband lasers. [Physics of Plasmas](#), 28(3):032103, March 2021. ISSN 1070-664X, 1089-7674. doi: 10.1063/5.0037869. URL <https://pubs.aip.org/pop/article/28/3/032103/835482/Thresholds-of-absolute-two-plasmon-decay-and>. 21
- [39] L. J. Perkins, R. Betti, K. N. LaFortune, and W. H. Williams. Shock Ignition: A New Approach to High Gain Inertial Confinement Fusion on the National Ignition Facility. [Physical Review Letters](#), 103(4):045004, July 2009. ISSN 0031-9007, 1079-7114. doi: 10.1103/PhysRevLett.103.045004. URL <https://link.aps.org/doi/10.1103/PhysRevLett.103.045004>. 21

- [40] A. G. Seaton, L. Yin, R. K. Follett, B. J. Albright, and A. Le. Cross-beam energy transfer in direct-drive ICF. II. Theory and simulation of mitigation through increased laser bandwidth. *Physics of Plasmas*, 29(4):042707, April 2022. ISSN 1070-664X. doi: 10.1063/5.0078801. URL <https://doi.org/10.1063/5.0078801>. 21
- [41] A. G. Seaton, L. Yin, R. K. Follett, B. J. Albright, and A. Le. Cross-beam energy transfer in direct-drive ICF. I. Nonlinear and kinetic effects. *Physics of Plasmas*, 29(4):042706, April 2022. ISSN 1070-664X. doi: 10.1063/5.0078800. URL <https://doi.org/10.1063/5.0078800>. 21
- [42] J. P. Chittenden, B. D. Appelbe, F. Manke, K. McGlinchey, and N. P. L. Niasse. Signatures of asymmetry in neutron spectra and images predicted by three-dimensional radiation hydrodynamics simulations of indirect drive implosions. *Physics of Plasmas*, 23(5):052708, May 2016. ISSN 1070-664X. doi: 10.1063/1.4949523. URL <https://doi.org/10.1063/1.4949523>. 24
- [43] Hyeong-Bin Cheong and Hyun-Gyu Kang. Eigensolutions of the spherical Laplacian for the cubed-sphere and icosahedral-hexagonal grids. *Quarterly Journal of the Royal Meteorological Society*, 141(693):3383–3398, October 2015. ISSN 0035-9009, 1477-870X. doi: 10.1002/qj.2620. URL <https://rmets.onlinelibrary.wiley.com/doi/10.1002/qj.2620>. 26
- [44] Zinovy Malkin. A New Equal-area Isolatitudinal Grid on a Spherical Surface. *The Astronomical Journal*, 158(4):158, October 2019. ISSN 0004-6256, 1538-3881. doi: 10.3847/1538-3881/ab3a44. URL <https://iopscience.iop.org/article/10.3847/1538-3881/ab3a44>. 26
- [45] Thomas B. Kaiser. Laser ray tracing and power deposition on an unstructured three-dimensional grid. *Physical Review E*, 61(1):895–905, January 2000. doi: 10.1103/PhysRevE.61.895. URL <https://link.aps.org/doi/10.1103/PhysRevE.61.895>. Publisher: American Physical Society. 29, 30, 32
- [46] Thierry Dewandre, James R. Albritton, and E. A. Williams. Doppler shift of laser light reflected from expanding plasmas. *The Physics of Fluids*, 24(3):528–536, March 1981. ISSN 0031-9171. doi: 10.1063/1.863401. URL <https://pubs.aip.org/pfl/article/24/3/528/894917/Doppler-shift-of-laser-light-reflected-from>. 29
- [47] William H. Press, editor. *Numerical recipes: the art of scientific computing*. Cambridge University Press, Cambridge, 3. ed edition, 2007. ISBN 978-0-521-88068-8. 30
- [48] Jacob Williams. *bspline-fortran*, January 2024. URL <https://zenodo.org/records/8423936>. 30
- [49] Charles K. Birdsall and A. Bruce Langdon. *Plasma physics via computer simulation*. McGraw-Hill, New York, 1985. ISBN 978-0-07-005371-7. 31

- [50] T D Arber, K Bennett, C S Brady, A Lawrence-Douglas, M G Ramsay, N J Sircombe, P Gillies, R G Evans, H Schmitz, A R Bell, and C P Ridgers. Contemporary particle-in-cell approach to laser-plasma modelling. *Plasma Physics and Controlled Fusion*, 57(11):113001, November 2015. ISSN 0741-3335, 1361-6587. doi: 10.1088/0741-3335/57/11/113001. URL <https://iopscience.iop.org/article/10.1088/0741-3335/57/11/113001>. 31
- [51] Christophe Cornet and Dixon T.K. Kwok. A new algorithm for charge deposition for multiple-grid method for PIC simulations in r-z cylindrical coordinates. *Journal of Computational Physics*, 225(1):808–828, July 2007. ISSN 00219991. doi: 10.1016/j.jcp.2007.01.004. URL <https://linkinghub.elsevier.com/retrieve/pii/S0021999107000058>. 31
- [52] Brian M. Haines, D.E. Keller, J.A. Marozas, P.W. McKenty, K.S. Anderson, T.J.B. Collins, W.W. Dai, M.L. Hall, S. Jones, M.D. McKay Jr, R.M. Rauenzahn, and D.N. Woods. Coupling laser physics to radiation-hydrodynamics. *Computers & Fluids*, 201:104478, April 2020. ISSN 00457930. doi: 10.1016/j.compfluid.2020.104478. URL <https://linkinghub.elsevier.com/retrieve/pii/S0045793020300517>. 31, 32, 34
- [53] J. Denavit and D. W. Phillion. Laser ionization and heating of gas targets for long-scale-length instability experiments. *Physics of Plasmas*, 1(6):1971–1984, June 1994. ISSN 1070-664X, 1089-7674. doi: 10.1063/1.870653. URL <https://pubs.aip.org/pop/article/1/6/1971/260717/Laser-ionization-and-heating-of-gas-targets-for>. 34, 35
- [54] I. V. Igumenshchev, F. J. Marshall, J. A. Marozas, V. A. Smalyuk, R. Epstein, V. N. Goncharov, T. J. B. Collins, T. C. Sangster, and S. Skupsky. The effects of target mounts in direct-drive implosions on OMEGA. *Physics of Plasmas*, 16(8):082701, August 2009. ISSN 1070-664X, 1089-7674. doi: 10.1063/1.3195065. URL <https://pubs.aip.org/pop/article/16/8/082701/316526/The-effects-of-target-mounts-in-direct-drive>. 39
- [55] I. V. Igumenshchev, V. N. Goncharov, F. J. Marshall, J. P. Knauer, E. M. Campbell, C. J. Forrest, D. H. Froula, V. Yu. Glebov, R. L. McCrory, S. P. Regan, T. C. Sangster, S. Skupsky, and C. Stoeckl. Three-dimensional modeling of direct-drive cryogenic implosions on OMEGA. *Physics of Plasmas*, 23(5):052702, May 2016. ISSN 1070-664X, 1089-7674. doi: 10.1063/1.4948418. URL <https://pubs.aip.org/pop/article/23/5/052702/958965/Three-dimensional-modeling-of-direct-drive>.
- [56] M. Gatu Johnson, P. J. Adrian, K. S. Anderson, B. D. Appelbe, J. P. Chittenden, A. J. Crilly, D. Edgell, C. J. Forrest, J. A. Frenje, V. Yu. Glebov, B. M. Haines, I. Igumenshchev, D. Jacobs-Perkins, R. Janezic, N. V. Kabadi, J. P. Knauer, B. Lahmann, O. M. Mannion, F. J. Marshall, T. Michel, F. H. Séguin, R. Shah, C. Stoeckl, C. A. Walsh, and R. D. Petrasso. Impact of stalk on directly driven inertial confinement fusion implosions. *Physics of Plasmas*, 27(3):032704, March 2020. ISSN 1070-664X, 1089-7674.

- doi: 10.1063/1.5141607. URL <https://pubs.aip.org/pop/article/27/3/032704/1063027/Impact-of-stalk-on-directly-driven-inertial>. 39
- [57] William L. Kruer. The physics of laser plasma interactions. Frontiers in physics. CRC Press, Boulder, Colo. [u.a.] Westview, 2003. ISBN 978-0-8133-4083-8. 40
- [58] Jurij A. Kravcov and Jurij I. Orlov. Caustics, catastrophes and wave fields. Number 15 in Springer series on wave phenomena. Springer, Berlin Heidelberg New York, 2. ed edition, 1999. ISBN 978-3-540-64227-5. 40
- [59] Yury Alexandrovich Kratsov and Ning Yan Zhu. Theory of diffraction: heuristic approaches. Alpha Science International, Oxford, 2010. ISBN 978-1-84265-372-2. 40
- [60] N. A. Lopez and I. Y. Dodin. Metaplectic geometrical optics for ray-based modeling of caustics: Theory and algorithms. Physics of Plasmas, 29(5):052111, May 2022. ISSN 1070-664X, 1089-7674. doi: 10.1063/5.0082241. URL <https://pubs.aip.org/pop/article/29/5/052111/2847808/Metaplectic-geometrical-optics-for-ray-based>. 40
- [61] Shan-chieh Chang and Jian-Ming Jin. Computation of special functions. Wiley, New York, 1996. ISBN 978-0-471-11963-0. 41
- [62] A.A. Asatryan and Yu.A. Kravtsov. Fresnel zones of hyperbolic type from the physical point of view. Wave Motion, 10(1):45–57, January 1988. ISSN 01652125. doi: 10.1016/0165-2125(88)90005-4. URL <https://linkinghub.elsevier.com/retrieve/pii/0165212588900054>. 41
- [63] Yu.A. Kravtsov. IV Rays and Caustics as Physical Objects. In Progress in Optics, volume 26, pages 227–348. Elsevier, 1988. ISBN 978-0-444-87096-4. doi: 10.1016/S0079-6638(08)70177-X. URL <https://linkinghub.elsevier.com/retrieve/pii/S007966380870177X>. 41
- [64] R. K. Follett. LPSE data for ray-based CBET test cases, August 2022. URL <https://zenodo.org/record/6962934>. 41, 56
- [65] Jiachen Ding, Ping Yang, Michael I. Mishchenko, and Robert D. Nevels. Identify the limits of geometric optics ray tracing by numerically solving the vector Kirchhoff integral. Optics Express, 28(7):10670, March 2020. ISSN 1094-4087. doi: 10.1364/OE.389097. URL <https://opg.optica.org/abstract.cfm?URI=oe-28-7-10670>. 45
- [66] E. A. Williams, R. L. Berger, R. P. Drake, A. M. Rubenchik, B. S. Bauer, D. D. Meyerhofer, A. C. Gaeris, and T. W. Johnston. The frequency and damping of ion acoustic waves in hydrocarbon (CH) and two-ion-species plasmas. Physics of Plasmas, 2(1):129–138, January 1995. ISSN 1070-664X, 1089-7674. doi: 10.1063/1.871101. URL <https://pubs.aip.org/pop/article/2/1/129/261605/The-frequency-and-damping-of-ion-acoustic-waves-in>. 47

- [67] P. Michel, W. Rozmus, E. A. Williams, L. Divol, R. L. Berger, S. H. Glenzer, and D. A. Callahan. Saturation of multi-laser beams laser-plasma instabilities from stochastic ion heating. *Physics of Plasmas*, 20(5):056308, May 2013. ISSN 1070-664X, 1089-7674. doi: 10.1063/1.4802828. URL <https://pubs.aip.org/pop/article/20/5/056308/109013/Saturation-of-multi-laser-beams-laser-plasma>. 47
- [68] G. P. M. Poppe and C. M. J. Wijers. Algorithm 680: evaluation of the complex error function. *ACM Transactions on Mathematical Software*, 16(1):47, March 1990. ISSN 0098-3500, 1557-7295. doi: 10.1145/77626.77630. URL <https://dl.acm.org/doi/10.1145/77626.77630>. 47
- [69] Burton D. Fried and Samuel D. Conte. *The Plasma Dispersion Function: The Hilbert Transform of the Gaussian*. Academic Press, 1961. ISBN 978-1-4832-2929-4. 48
- [70] T. R. Boehly, V. A. Smalyuk, D. D. Meyerhofer, J. P. Knauer, D. K. Bradley, R. S. Craxton, M. J. Guardalben, S. Skupsky, and T. J. Kessler. Reduction of laser imprinting using polarization smoothing on a solid-state fusion laser. *Journal of Applied Physics*, 85(7):3444–3447, April 1999. ISSN 0021-8979, 1089-7550. doi: 10.1063/1.369702. URL <https://pubs.aip.org/jap/article/85/7/3444/491506/Reduction-of-laser-imprinting-using-polarization>. 48
- [71] D. H. Edgell, P. B. Radha, J. Katz, A. Shvydky, D. Turnbull, and D. H. Froula. Nonuniform Absorption and Scattered Light in Direct-Drive Implosions Driven by Polarization Smoothing. *Physical Review Letters*, 127(7):075001, August 2021. ISSN 0031-9007, 1079-7114. doi: 10.1103/PhysRevLett.127.075001. URL <https://link.aps.org/doi/10.1103/PhysRevLett.127.075001>. 48
- [72] A. Colaïtis, D. P. Turnbull, I. V. Igumenschev, D. Edgell, R. C. Shah, O. M. Mannion, C. Stoeckl, D. Jacob-Perkins, A. Shvydky, R. Janezic, A. Kalb, D. Cao, C. J. Forrest, J. Kwiatkowski, S. Regan, W. Theobald, V. N. Goncharov, and D. H. Froula. 3D Simulations Capture the Persistent Low-Mode Asymmetries Evident in Laser-Direct-Drive Implosions on OMEGA. *Physical Review Letters*, 129(9):095001, August 2022. ISSN 0031-9007, 1079-7114. doi: 10.1103/PhysRevLett.129.095001. URL <https://link.aps.org/doi/10.1103/PhysRevLett.129.095001>.
- [73] A Colaïtis, D Edgell, I Igumenshchev, D Turnbull, D J Strozzi, T Chapman, V Goncharov, and D H Froula. 3D simulations of inertial confinement fusion implosions part 1: inline modeling of polarized cross beam energy transfer and subsequent drive anomalies on OMEGA and NIF. *Plasma Physics and Controlled Fusion*, 65(1):014003, January 2023. ISSN 0741-3335, 1361-6587. doi: 10.1088/1361-6587/aca78e. URL <https://iopscience.iop.org/article/10.1088/1361-6587/aca78e>. 66, 67
- [74] A Colaïtis, I V Igumenshchev, D P Turnbull, R Shah, D Edgell, O M Mannion, C Stoeckl, D W Jacob-Perkins, A Shvydky, R Janezic, A Kalb, D Cao, C J Forrest, J Kwiatkowski, S P

- Regan, W Theobald, V N Goncharov, and D Froula. 3D simulations of inertial confinement fusion implosions part 2: systematic flow anomalies and impact of low modes on performances in OMEGA experiments. *Plasma Physics and Controlled Fusion*, 65(1): 014005, January 2023. ISSN 0741-3335, 1361-6587. doi: 10.1088/1361-6587/aca78d. URL <https://iopscience.iop.org/article/10.1088/1361-6587/aca78d>. 48
- [75] O. M. Mannion, I. V. Igumenshchev, K. S. Anderson, R. Betti, E. M. Campbell, D. Cao, C. J. Forrest, M. Gatu Johnson, V. Yu. Glebov, V. N. Goncharov, V. Gopalaswamy, S. T. Ivancic, D. W. Jacobs-Perkins, A. Kalb, J. P. Knauer, J. Kwiatkowski, A. Lees, F. J. Marshall, M. Michalko, Z. L. Mohamed, D. Patel, H. G. Rinderknecht, R. C. Shah, C. Stoeckl, W. Theobald, K. M. Woo, and S. P. Regan. Mitigation of mode-one asymmetry in laser-direct-drive inertial confinement fusion implosions. *Physics of Plasmas*, 28(4):042701, April 2021. ISSN 1070-664X, 1089-7674. doi: 10.1063/5.0041554. URL <https://pubs.aip.org/pop/article/28/4/042701/263531/Mitigation-of-mode-one-asymmetry-in-laser-direct>. 48, 75, 76
- [76] James McHardy. An introduction to the theory and use of SESAME equations of state. Technical Report LA-14503, 1487368, December 2018. URL <https://www.osti.gov/servlets/purl/1487368/>. 62, 80
- [77] A.J. Crilly, N.P.L. Niasse, A.R. Fraser, D.A. Chapman, K.W. McLean, S.J. Rose, and J.P. Chittenden. SpK: A fast atomic and microphysics code for the high-energy-density regime. *High Energy Density Physics*, 48:101053, September 2023. ISSN 15741818. doi: 10.1016/j.hedp.2023.101053. URL <https://linkinghub.elsevier.com/retrieve/pii/S1574181823000198>. 62
- [78] Lyman Spitzer and Richard Härm. Transport Phenomena in a Completely Ionized Gas. *Physical Review*, 89(5):977–981, March 1953. ISSN 0031-899X. doi: 10.1103/PhysRev.89.977. URL <https://link.aps.org/doi/10.1103/PhysRev.89.977>. 62
- [79] C. D. Zhou and R. Betti. Hydrodynamic relations for direct-drive fast-ignition and conventional inertial confinement fusion implosions. *Physics of Plasmas*, 14(7):072703, July 2007. ISSN 1070-664X, 1089-7674. doi: 10.1063/1.2746812. URL <https://pubs.aip.org/pop/article/14/7/072703/985533/Hydrodynamic-relations-for-direct-drive-fast>. 64
- [80] W. Trickey, V. N. Goncharov, R. Betti, E. M. Campbell, T. J. B. Collins, and R. K. Follett. The physics of gain relevant to inertial fusion energy target designs. *Physics of Plasmas*, 31(1):012702, January 2024. ISSN 1070-664X, 1089-7674. doi: 10.1063/5.0167405. URL <https://pubs.aip.org/pop/article/31/1/012702/2932657/The-physics-of-gain-relevant-to-inertial-fusion>. 64, 73
- [81] T. R. Boehly, R. S. Craxton, T. H. Hinterman, J. H. Kelly, T. J. Kessler, S. A. Kumpan, S. A. Letzring, R. L. McCrory, S. F. B. Morse, W. Seka, S. Skupsky, J. M. Soures, and C. P. Verdon. The upgrade to the OMEGA laser system. *Review of Scientific*

- Instruments, 66(1):508–510, January 1995. ISSN 0034-6748, 1089-7623. doi: 10.1063/1.1146333. URL <https://pubs.aip.org/rsi/article/66/1/508/455144/The-upgrade-to-the-OMEGA-laser-systemPlasma>. 67
- [82] A. Simon. LLE Review Quarterly Report (April-June 1989). Volume 39. Technical Report DOE/DP/40200-95, 1191446, June 1989. URL <http://www.osti.gov/servlets/purl/1191446/>. 67
- [83] R. H. H. Scott, D. Barlow, W. Trickey, A. Ruocco, K. Glize, L. Antonelli, M. Khan, and N. C. Woolsey. Shock-Augmented Ignition Approach to Laser Inertial Fusion. *Physical Review Letters*, 129(19):195001, November 2022. ISSN 0031-9007, 1079-7114. doi: 10.1103/PhysRevLett.129.195001. URL <https://link.aps.org/doi/10.1103/PhysRevLett.129.195001>. 71
- [84] A. Colaïtis, R. K. Follett, C. Dorner, A. G. Seaton, D. Viala, I. Igumenshchev, D. Turnbull, V. Goncharov, and D. H. Froula. Exploration of cross-beam energy transfer mitigation constraints for designing an ignition-scale direct-drive inertial confinement fusion driver. *Physics of Plasmas*, 30(8):082701, August 2023. ISSN 1070-664X, 1089-7674. doi: 10.1063/5.0150813. URL <https://pubs.aip.org/pop/article/30/8/082701/2906541/Exploration-of-cross-beam-energy-transfer>. 72, 73
- [85] K. S. Anderson, J. A. Marozas, T. J. B. Collins, C. J. Forrest, V. N. Goncharov, and D. Cao. Enhanced sensitivity to target offset when using cross-beam energy transfer mitigation techniques in direct-drive inertial confinement fusion implosions. *Physics of Plasmas*, 31(3):032704, March 2024. ISSN 1070-664X, 1089-7674. doi: 10.1063/5.0191277. URL <https://pubs.aip.org/pop/article/31/3/032704/3278248/Enhanced-sensitivity-to-target-offset-when-using>. 72
- [86] J. W. Bates, J. F. Myatt, J. G. Shaw, R. K. Follett, J. L. Weaver, R. H. Lehmberg, and S. P. Obenschain. Mitigation of cross-beam energy transfer in inertial-confinement-fusion plasmas with enhanced laser bandwidth. *Physical Review E*, 97(6):061202, June 2018. ISSN 2470-0045, 2470-0053. doi: 10.1103/PhysRevE.97.061202. URL <https://link.aps.org/doi/10.1103/PhysRevE.97.061202>. 72
- [87] J. W. Bates, R. K. Follett, J. G. Shaw, S. P. Obenschain, J. F. Myatt, J. L. Weaver, M. F. Wolford, D. M. Kehne, M. C. Myers, and T. J. Kessler. Suppressing parametric instabilities in direct-drive inertial-confinement-fusion plasmas using broadband laser light. *Physics of Plasmas*, 30(5):052703, May 2023. ISSN 1070-664X, 1089-7674. doi: 10.1063/5.0150865. URL <https://pubs.aip.org/pop/article/30/5/052703/2890436/Suppressing-parametric-instabilities-in-direct>.
- [88] R. K. Follett, A. Colaïtis, A. G. Seaton, H. Wen, D. Turnbull, D. H. Froula, and J. P. Palastro. Ray-based cross-beam energy transfer modeling for broadband lasers. *Physics of Plasmas*, 30(4):042102, April 2023. ISSN 1070-664X, 1089-7674. doi: 10.1063/5.0137420. URL <https://pubs.aip.org/pop/article/30/4/042102/2882936/Ray-based-cross-beam-energy-transfer-modeling-for>. 72

- [89] D. M. Kehne, M. Karasik, Y. Aglitsky, Z. Smyth, S. Terrell, J. L. Weaver, Y. Chan, R. H. Lehmberg, and S. P. Obenschain. Implementation of focal zooming on the Nike KrF laser. *Review of Scientific Instruments*, 84(1):013509, January 2013. ISSN 0034-6748, 1089-7623. doi: 10.1063/1.4789313. URL <https://pubs.aip.org/rsi/article/84/1/013509/354878/Implementation-of-focal-zooming-on-the-Nike-KrF>. 73
- [90] A. Lees, R. Betti, J. P. Knauer, V. Gopalaswamy, D. Patel, K. M. Woo, K. S. Anderson, E. M. Campbell, D. Cao, J. Carroll-Nellenback, R. Epstein, C. Forrest, V. N. Goncharov, D. R. Harding, S. X. Hu, I. V. Igumenshchev, R. T. Janezic, O. M. Mannion, P. B. Radha, S. P. Regan, A. Shvydky, R. C. Shah, W. T. Shmayda, C. Stoeckl, W. Theobald, and C. Thomas. Experimentally Inferred Fusion Yield Dependencies of OMEGA Inertial Confinement Fusion Implosions. *Physical Review Letters*, 127(10):105001, August 2021. ISSN 0031-9007, 1079-7114. doi: 10.1103/PhysRevLett.127.105001. URL <https://link.aps.org/doi/10.1103/PhysRevLett.127.105001>. 74
- [91] V. Gopalaswamy, R. Betti, J. P. Knauer, N. Luciani, D. Patel, K. M. Woo, A. Bose, I. V. Igumenshchev, E. M. Campbell, K. S. Anderson, K. A. Bauer, M. J. Bonino, D. Cao, A. R. Christopherson, G. W. Collins, T. J. B. Collins, J. R. Davies, J. A. Delettrez, D. H. Edgell, R. Epstein, C. J. Forrest, D. H. Froula, V. Y. Glebov, V. N. Goncharov, D. R. Harding, S. X. Hu, D. W. Jacobs-Perkins, R. T. Janezic, J. H. Kelly, O. M. Mannion, A. Maximov, F. J. Marshall, D. T. Michel, S. Miller, S. F. B. Morse, J. Palastro, J. Peebles, P. B. Radha, S. P. Regan, S. Sampat, T. C. Sangster, A. B. Sefkow, W. Seka, R. C. Shah, W. T. Shmyada, A. Shvydky, C. Stoeckl, A. A. Solodov, W. Theobald, J. D. Zuegel, M. Gatu Johnson, R. D. Petrasso, C. K. Li, and J. A. Frenje. Tripled yield in direct-drive laser fusion through statistical modelling. *Nature*, 565(7741):581–586, January 2019. ISSN 0028-0836, 1476-4687. doi: 10.1038/s41586-019-0877-0. URL <https://www.nature.com/articles/s41586-019-0877-0>. 74
- [92] V. Gopalaswamy, R. Betti, J. P. Knauer, A. Lees, D. Patel, A. R. Christopherson, I. V. Igumenshchev, D. Cao, K. S. Anderson, A. Shvydky, D. H. Edgell, O. M. Mannion, C. Thomas, W. Theobald, C. Stoeckl, S. P. Regan, V. N. Goncharov, R. Shah, and E. M. Campbell. Using statistical modeling to predict and understand fusion experiments. *Physics of Plasmas*, 28(12):122705, December 2021. ISSN 1070-664X, 1089-7674. doi: 10.1063/5.0056662. URL <https://pubs.aip.org/pop/article/28/12/122705/108236/Using-statistical-modeling-to-predict-and>. 74, 77, 95
- [93] R. Ejaz, V. Gopalaswamy, A. Lees, C. Kanan, D. Cao, and R. Betti. Deep learning-based predictive models for laser direct drive at the Omega Laser Facility. *Physics of Plasmas*, 31(5):052703, May 2024. ISSN 1070-664X, 1089-7674. doi: 10.1063/5.0195675. URL <https://pubs.aip.org/pop/article/31/5/052703/3293889/Deep-learning-based-predictive-models-for-laser>. 74
- [94] C. A. Thomas, D. Cao, W. Theobald, R. Betti, K. A. Anderson, K. A. Bauer, E. M. Campbell, A. R. Christopherson, T. J. B. Collins, R. S. Craxton, D. H. Edgell, R. Epstein,

- C. J. Forrest, V. Yu. Glebov, V. Gopalaswamy, I. V. Igumenshchev, S. T. Ivancic, D. W. Jacobs-Perkins, R. T. Janezic, T. Joshi, J. P. Knauer, J. Kwiatkowski, A. Lees, O. M. Manzion, F. J. Marshall, and LLE Team. Quantifying the Effects of Scale and Illumination Geometry in Laser Direct Drive. 2020:BO09.014, January 2020. URL <https://ui.adsabs.harvard.edu/abs/2020APS..DPPB09014T>. Conference Name: APS Division of Plasma Physics Meeting Abstracts ADS Bibcode: 2020APS..DPPB09014T. 74
- [95] S. X. Hu, G. Fiksel, V. N. Goncharov, S. Skupsky, D. D. Meyerhofer, and V. A. Smalyuk. Mitigating Laser Imprint in Direct-Drive Inertial Confinement Fusion Implosions with High- Z Dopants. *Physical Review Letters*, 108(19):195003, May 2012. ISSN 0031-9007, 1079-7114. doi: 10.1103/PhysRevLett.108.195003. URL <https://link.aps.org/doi/10.1103/PhysRevLett.108.195003>. 74
- [96] Max Karasik, J. L. Weaver, Y. Aglitskiy, J. Oh, and S. P. Obenschain. Suppression of Laser Nonuniformity Imprinting Using a Thin High- Z Coating. *Physical Review Letters*, 114(8):085001, February 2015. ISSN 0031-9007, 1079-7114. doi: 10.1103/PhysRevLett.114.085001. URL <https://link.aps.org/doi/10.1103/PhysRevLett.114.085001>.
- [97] S. X. Hu, W. Theobald, P. B. Radha, J. L. Peebles, S. P. Regan, A. Nikroo, M. J. Bonino, D. R. Harding, V. N. Goncharov, N. Petta, T. C. Sangster, and E. M. Campbell. Mitigating laser-imprint effects in direct-drive inertial confinement fusion implosions with an above-critical-density foam layer. *Physics of Plasmas*, 25(8):082710, August 2018. ISSN 1070-664X, 1089-7674. doi: 10.1063/1.5044609. URL <https://pubs.aip.org/pop/article/25/8/082710/1058211/Mitigating-laser-imprint-effects-in-direct-drive>. 74
- [98] T. R. Dittrich, B. A. Hammel, C. J. Keane, R. McEachern, R. E. Turner, S. W. Haan, and L. J. Suter. Diagnosis of Pusher-Fuel Mix in Indirectly Driven Nova Implosions. *Physical Review Letters*, 73(17):2324–2327, October 1994. ISSN 0031-9007. doi: 10.1103/PhysRevLett.73.2324. URL <https://link.aps.org/doi/10.1103/PhysRevLett.73.2324>. 74
- [99] S. C. Miller and V. N. Goncharov. Instability seeding mechanisms due to internal defects in inertial confinement fusion targets. *Physics of Plasmas*, 29(8):082701, August 2022. ISSN 1070-664X, 1089-7674. doi: 10.1063/5.0091949. URL <https://pubs.aip.org/pop/article/29/8/082701/2844945/Instability-seeding-mechanisms-due-to-internal>. 74
- [100] A. G. MacPhee, J. L. Peterson, D. T. Casey, D. S. Clark, S. W. Haan, O. S. Jones, O. L. Landen, J. L. Milovich, H. F. Robey, and V. A. Smalyuk. Stabilization of high-compression, indirect-drive inertial confinement fusion implosions using a 4-shock adiabat-shaped drive. *Physics of Plasmas*, 22(8):080702, August 2015. ISSN 1070-664X, 1089-7674. doi: 10.1063/1.4928909. URL <https://pubs.aip.org/pop/article/22/8/080702/109302/Stabilization-of-high-compression-indirect-drive>. 74

- [101] V.A. Smalyuk, H.F. Robey, D.T. Casey, D.S. Clark, T. Döppner, S.W. Haan, B.A. Hammel, A.G. MacPhee, D. Martinez, J.L. Milovich, J.L. Peterson, L. Pickworth, J.E. Pino, K. Raman, R. Tipton, C.R. Weber, K.L. Baker, B. Bachmann, L.F. Berzak Hopkins, E. Bond, J.A. Caggiano, D.A. Callahan, P.M. Celliers, C. Cerjan, S.N. Dixit, M.J. Edwards, S. Felker, J.E. Field, D.N. Fittinghoff, N. Gharibyan, G.P. Grim, A.V. Hamza, R. Hatarik, M. Hohenberger, W.W. Hsing, O.A. Hurricane, K.S. Jancaitis, O.S. Jones, S. Khan, J.J. Kroll, K.N. Lafortune, O.L. Landen, T. Ma, B.J. MacGowan, L. Masse, A.S. Moore, S.R. Nagel, A. Nikroo, A. Pak, P.K. Patel, B.A. Remington, D.B. Sayre, B.K. Spears, M. Stadermann, R. Tommasini, C.C. Widmayer, C.B. Yeamans, J. Crippen, M. Farrell, E. Giraldez, N. Rice, C.H. Wilde, P.L. Volegov, and M. Gatu Johnson. Mix and hydrodynamic instabilities on NIF. *Journal of Instrumentation*, 12(06):C06001–C06001, June 2017. ISSN 1748-0221. doi: 10.1088/1748-0221/12/06/C06001. URL <https://iopscience.iop.org/article/10.1088/1748-0221/12/06/C06001>. 74
- [102] Brian M. Haines, R. E. Olson, W. Sweet, S. A. Yi, A. B. Zylstra, P. A. Bradley, F. Elsner, H. Huang, R. Jimenez, J. L. Kline, C. Kong, G. A. Kyrala, R. J. Leeper, R. Paguio, S. Pajoom, R. R. Peterson, M. Ratledge, and N. Rice. Robustness to hydrodynamic instabilities in indirectly driven layered capsule implosions. *Physics of Plasmas*, 26(1):012707, January 2019. ISSN 1070-664X, 1089-7674. doi: 10.1063/1.5080262. URL <https://pubs.aip.org/pop/article/26/1/012707/367410/Robustness-to-hydrodynamic-instabilities-in>. 75
- [103] S.P. Regan, V.N. Goncharov, T.C. Sangster, E.M. Campbell, R. Betti, J.W. Bates, K. Bauer, T. Bernat, S. Bhandarkar, T.R. Boehly, M.J. Bonino, A. Bose, D. Cao, L. Carlson, R. Chapman, T. Chapman, G.W. Collins, T.J.B. Collins, R.S. Craxton, J.A. Delettrez, D.H. Edgell, R. Epstein, M. Farrell, C.J. Forrest, R.K. Follett, J.A. Frenje, D.H. Froula, M. Gatu Johnson, C.R. Gibson, L. Gonzalez, C. Goyon, V.Yu Glebov, V. Gopalaswamy, A. Greenwood, D.R. Harding, M. Hohenberger, S.X. Hu, H. Huang, J. Hund, I.V. Igumenshchev, D.W. Jacobs-Perkins, R.T. Janezic, M. Karasik, J.H. Kelly, T.J. Kessler, J.P. Knauer, T.Z. Kosc, R. Luo, S.J. Loucks, J.A. Marozas, F.J. Marshall, M. Mauldin, R.L. McCrory, P.W. Mckenty, D.T. Michel, P. Michel, J.D. Moody, J.F. Myatt, A. Nikroo, P.M. Nilson, S.P. Obenschain, J.P. Palastro, J. Peebles, R.D. Petrasso, N. Petta, P.B. Radha, J.E. Ralph, M.J. Rosenberg, S. Sampat, A.J. Schmitt, M.J. Schmitt, M. Schoff, W. Seka, R. Shah, J.R. Rygg, J.G. Shaw, R. Short, W.T. Shmayda, M.J. Shoup, A. Shvydky, A.A. Solodov, C. Sorce, M. Stadermann, C. Stoeckl, W. Sweet, C. Taylor, R. Taylor, W. Theobald, D.P. Turnbull, J. Ulreich, M.D. Wittman, K.M. Woo, K. Youngblood, and J.D. Zuegel. The National Direct-Drive Inertial Confinement Fusion Program. *Nuclear Fusion*, 59(3):032007, March 2019. ISSN 0029-5515, 1741-4326. doi: 10.1088/1741-4326/aae9b5. URL <https://iopscience.iop.org/article/10.1088/1741-4326/aae9b5>. 75
- [104] K. M. Woo, R. Betti, O. M. Mannion, C. J. Forrest, J. P. Knauer, V. N. Goncharov, P. B. Radha, D. Patel, V. Gopalaswamy, and V. Yu. Glebov. Inferring thermal ion temperature and residual kinetic energy from nuclear measurements in inertial confinement fusion

- implosions. *Physics of Plasmas*, 27(6):062702, June 2020. ISSN 1070-664X, 1089-7674. doi: 10.1063/1.5144460. URL <https://pubs.aip.org/pop/article/27/6/062702/1025468/Inferring-thermal-ion-temperature-and-residual>. 76
- [105] R. S. Craxton, K. S. Anderson, T. R. Boehly, V. N. Goncharov, D. R. Harding, J. P. Knauer, R. L. McCrory, P. W. McKenty, D. D. Meyerhofer, J. F. Myatt, A. J. Schmitt, J. D. Sethian, R. W. Short, S. Skupsky, W. Theobald, W. L. Kruer, K. Tanaka, R. Betti, T. J. B. Collins, J. A. Delettrez, S. X. Hu, J. A. Marozas, A. V. Maximov, D. T. Michel, P. B. Radha, S. P. Regan, T. C. Sangster, W. Seka, A. A. Solodov, J. M. Soures, C. Stoeckl, and J. D. Zuegel. Direct-drive inertial confinement fusion: A review. *Physics of Plasmas*, 22(11):110501, November 2015. ISSN 1070-664X, 1089-7674. doi: 10.1063/1.4934714. URL <https://pubs.aip.org/pop/article/22/11/110501/109006/Direct-drive-inertial-confinement-fusion-A-review>. 76
- [106] V N Goncharov, S P Regan, E M Campbell, T C Sangster, P B Radha, J F Myatt, D H Froula, R Betti, T R Boehly, J A Delettrez, D H Edgell, R Epstein, C J Forrest, V Yu Glebov, D R Harding, S X Hu, I V Igumenshchev, F J Marshall, R L McCrory, D T Michel, W Seka, A Shvydky, C Stoeckl, W Theobald, and M Gatu-Johnson. National direct-drive program on OMEGA and the National Ignition Facility. *Plasma Physics and Controlled Fusion*, 59(1):014008, January 2017. ISSN 0741-3335, 1361-6587. doi: 10.1088/0741-3335/59/1/014008. URL <https://iopscience.iop.org/article/10.1088/0741-3335/59/1/014008>. 76
- [107] G. Pérez-Callejo, C. Vlachos, C. A. Walsh, R. Florido, M. Bailly-Grandvaux, X. Vaisseau, F. Suzuki-Vidal, C. McGuffey, F. N. Beg, P. Bradford, V. Ospina-Bohórquez, D. Batani, D. Raffestin, A. Colaiòtis, V. Tikhonchuk, A. Casner, M. Koenig, B. Albertazzi, R. Fedosejevs, N. Woolsey, M. Ehret, A. Debayle, P. Loiseau, A. Calisti, S. Ferri, J. Honrubia, R. Kingham, R. C. Mancini, M. A. Gigosos, and J. J. Santos. Cylindrical implosion platform for the study of highly magnetized plasmas at Laser MegaJoule. *Physical Review E*, 106(3):035206, September 2022. ISSN 2470-0045, 2470-0053. doi: 10.1103/PhysRevE.106.035206. URL <https://link.aps.org/doi/10.1103/PhysRevE.106.035206>. 79
- [108] D.L. Tubbs, C.W. Barnes, J.B. Beck, N.M. Hoffman, J.A. Oertel, R.G. Watt, T. Boehly, D. Bradley, and J. Knauer. Direct-drive cylindrical implosion experiments: Simulations and data. *Laser and Particle Beams*, 17(3):437–449, July 1999. ISSN 0263-0346, 1469-803X. doi: 10.1017/S0263034699173117. URL https://www.cambridge.org/core/product/identifier/S0263034699173117/type/journal_article. 79
- [109] D. W. Peaceman and H. H. Rachford, Jr. The Numerical Solution of Parabolic and Elliptic Differential Equations. *Journal of the Society for Industrial and Applied Mathematics*, 3(1):28–41, March 1955. ISSN 0368-4245, 2168-3484. doi: 10.1137/0103003. URL <http://epubs.siam.org/doi/10.1137/0103003>. 80

- [110] A. Bose, R. Betti, D. Shvarts, and K. M. Woo. The physics of long- and intermediate-wavelength asymmetries of the hot spot: Compression hydrodynamics and energetics. *Physics of Plasmas*, 24(10):102704, October 2017. ISSN 1070-664X, 1089-7674. doi: 10.1063/1.4995250. URL <https://pubs.aip.org/pop/article/24/10/102704/795291/The-physics-of-long-and-intermediate-wavelength>. 93
- [111] A. Bose, R. Betti, D. Mangino, K. M. Woo, D. Patel, A. R. Christopherson, V. Gopalaswamy, O. M. Mannion, S. P. Regan, V. N. Goncharov, D. H. Edgell, C. J. Forrest, J. A. Frenje, M. Gatun Johnson, V. Yu Glebov, I. V. Igumenshchev, J. P. Knauer, F. J. Marshall, P. B. Radha, R. Shah, C. Stoeckl, W. Theobald, T. C. Sangster, D. Shvarts, and E. M. Campbell. Analysis of trends in experimental observables: Reconstruction of the implosion dynamics and implications for fusion yield extrapolation for direct-drive cryogenic targets on OMEGA. *Physics of Plasmas*, 25(6):062701, June 2018. ISSN 1070-664X, 1089-7674. doi: 10.1063/1.5026780. URL <https://pubs.aip.org/pop/article/25/6/062701/320064/Analysis-of-trends-in-experimental-observables>. 93
- [112] G. P. Schurtz, Ph. D. Nicolaï, and M. Busquet. A nonlocal electron conduction model for multidimensional radiation hydrodynamics codes. *Physics of Plasmas*, 7(10):4238–4249, October 2000. ISSN 1070-664X, 1089-7674. doi: 10.1063/1.1289512. URL <https://pubs.aip.org/pop/article/7/10/4238/264657/A-nonlocal-electron-conduction-model-for>. 97
- [113] Ph. D. Nicolaï, J.-L. A. Feugeas, and G. P. Schurtz. A practical nonlocal model for heat transport in magnetized laser plasmas. *Physics of Plasmas*, 13(3):032701, March 2006. ISSN 1070-664X, 1089-7674. doi: 10.1063/1.2179392. URL <https://pubs.aip.org/pop/article/13/3/032701/316589/A-practical-nonlocal-model-for-heat-transport-in>.
- [114] Duc Cao, Gregory Moses, and Jacques Delettrez. Improved non-local electron thermal transport model for two-dimensional radiation hydrodynamics simulations. *Physics of Plasmas*, 22(8):082308, August 2015. ISSN 1070-664X, 1089-7674. doi: 10.1063/1.4928445. URL <https://pubs.aip.org/pop/article/22/8/082308/109167/Improved-non-local-electron-thermal-transport>. 97
- [115] Anthony R Bell and Mark Sherlock. The *fast* VFP code for solution of the Vlasov-Fokker-Planck equation. *Plasma Physics and Controlled Fusion*, January 2024. ISSN 0741-3335, 1361-6587. doi: 10.1088/1361-6587/ad2278. URL <https://iopscience.iop.org/article/10.1088/1361-6587/ad2278>. 97
- [116] D. Patel, J. P. Knauer, D. Cao, R. Betti, R. Nora, A. Shvydky, V. Gopalaswamy, A. Lees, S. Sampat, W. R. Donaldson, S. P. Regan, C. Stoeckl, C. J. Forrest, V. Yu. Glebov, D. R. Harding, M. J. Bonino, R. T. Janezic, D. Wasilewski, C. Fella, C. Shuldberg, J. Murray, D. Guzman, and B. Serrato. Effects of Laser Bandwidth in Direct-Drive High-Performance DT-Layered Implosions on the OMEGA Laser.

- Physical Review Letters, 131(10):105101, September 2023. ISSN 0031-9007, 1079-7114.
doi: 10.1103/PhysRevLett.131.105101. URL <https://link.aps.org/doi/10.1103/PhysRevLett.131.105101>. 97
- [117] T. R. Dittrich, O. A. Hurricane, D. A. Callahan, E. L. Dewald, T. Döppner, D. E. Hinkel, L. F. Berzak Hopkins, S. Le Pape, T. Ma, J. L. Milovich, J. C. Moreno, P. K. Patel, H.-S. Park, B. A. Remington, J. D. Salmonson, and J. L. Kline. Design of a High-Foot High-Adiabat ICF Capsule for the National Ignition Facility. Physical Review Letters, 112(5):055002, February 2014. ISSN 0031-9007, 1079-7114. doi: 10.1103/PhysRevLett.112.055002. URL <https://link.aps.org/doi/10.1103/PhysRevLett.112.055002>. 97
- [118] H. F. Robey, V. A. Smalyuk, J. L. Milovich, T. Döppner, D. T. Casey, K. L. Baker, J. L. Peterson, B. Bachmann, L. F. Berzak Hopkins, E. Bond, J. A. Caggiano, D. A. Callahan, P. M. Celliers, C. Cerjan, D. S. Clark, S. N. Dixit, M. J. Edwards, N. Gharibyan, S. W. Haan, B. A. Hammel, A. V. Hamza, R. Hatarik, O. A. Hurricane, K. S. Jancaitis, O. S. Jones, G. D. Kerbel, J. J. Kroll, K. N. Lafortune, O. L. Landen, T. Ma, M. M. Marinak, B. J. MacGowan, A. G. MacPhee, A. Pak, M. Patel, P. K. Patel, L. J. Perkins, D. B. Sayre, S. M. Sepke, B. K. Spears, R. Tommasini, C. R. Weber, C. C. Widmayer, C. Yeamans, E. Giraldez, D. Hoover, A. Nikroo, M. Hohenberger, and M. Gatu Johnson. Performance of indirectly driven capsule implosions on the National Ignition Facility using adiabat-shaping. Physics of Plasmas, 23(5):056303, May 2016. ISSN 1070-664X, 1089-7674. doi: 10.1063/1.4944821. URL <https://pubs.aip.org/pop/article/23/5/056303/966084/Performance-of-indirectly-driven-capsule>. 97
- [119] S. X. Hu, R. Epstein, W. Theobald, H. Xu, H. Huang, V. N. Goncharov, S. P. Regan, P. W. McKenty, R. Betti, E. M. Campbell, and D. S. Montgomery. Direct-drive double-shell implosion: A platform for burning-plasma physics studies. Physical Review E, 100(6):063204, December 2019. ISSN 2470-0045, 2470-0053. doi: 10.1103/PhysRevE.100.063204. URL <https://link.aps.org/doi/10.1103/PhysRevE.100.063204>. 97
- [120] I. V. Igumenshchev, A. L. Velikovich, V. N. Goncharov, R. Betti, E. M. Campbell, J. P. Knauer, S. P. Regan, A. J. Schmitt, R. C. Shah, and A. Shvydky. Rarefaction Flows and Mitigation of Imprint in Direct-Drive Implosions. Physical Review Letters, 123(6):065001, August 2019. ISSN 0031-9007, 1079-7114. doi: 10.1103/PhysRevLett.123.065001. URL <https://link.aps.org/doi/10.1103/PhysRevLett.123.065001>. 97

Permissions